**KAM TORUS ORBIT PREDICTION FROM TWO
LINE ELEMENT SETS**

THESIS

Rasit ABAY, 1st Lieutenant, TURAF

AFIT-ENY-14-M-01

**DEPARTMENT OF THE AIR FORCE
AIR UNIVERSITY**

AIR FORCE INSTITUTE OF TECHNOLOGY

Wright-Patterson Air Force Base, Ohio

AFIT-ENY-14-M-01

KAM TORUS ORBIT PREDICTION FROM TWO LINE ELEMENT SETS

THESIS

Presented to the Faculty

Department of Aeronautics and Astronautics

Graduate School of Engineering and Management

Air Force Institute of Technology

Air University

Air Education and Training Command

in Partial Fulfillment of the Requirements for the

Degree of Master of Science in Space Systems

Rasit ABAY, BS

1$^{\text{st}}$ Lieutenant, TURAF

March 2014

AFIT-ENY-14-M-01

KAM TORUS ORBIT PREDICTION FROM TWO LINE ELEMENT SETS

Rasit ABAY, BS
1st Lieutenant, TURAF

Approved:

//signed//   Feb 28, 2014
_____   _____
William E. Wiesel, PhD (Chairman)   Date

//signed//   Mar 11, 2014
_____   _____
Alan L. Jennings, PhD (Member)   Date

//signed//   Mar 06, 2014
_____   _____
Kerry D. Hicks, PhD (Member)   Date

AFIT-ENY-14-M-01

Abstract

A new method for orbit prediction, which is as accurate as numerical methods and as fast as analytical methods, in terms of computational time, is desirable. This paper presents Kolmogorov Arnol'd Moser (KAM) torus orbit prediction using Simplified General Perturbations 4 (SGP4) and Two-Line Element (TLE) data. First, a periodic orbit and its Floquet solution are calculated. After that, perturbations, which are on the order of 10^{-5} and smaller, are added to the periodic orbit plus Floquet solution. Then, the low eccentricity KAM torus is least squares fitted to the SGP4 and TLE data. The performance of the theory is presented in various ways. The new method is approximately five times more accurate for the best fits and three times more accurate for mean fits comparing to SGP4 and TLE. History of TLEs and KAM torus theory can be used to make accurate orbit predictions, which is conceptually similar to extrapolation. In addition, the new method may rival numerical methods and it can be used for collision avoidance calculations, and formation flight applications. However, high eccentricity, polar and critical inclination, air drag, and resonance problems should be addressed.

Acknowledgements

Contents

List of Figures

List of Tables

KAM TORUS ORBIT PREDICTION FROM TWO LINE ELEMENT SETS

I. Introduction

Artificial satellites are indispensable parts of the daily lives of people. Both civilian and military world depend on satellites orbiting Earth at very high speeds. There are many applications of satellites such as communication, navigation, Earth observation, and weather. The position of a satellite should be known within a certain limit to establish communication between ground stations and the satellite. The accurate positions of satellites and debris are important for collision avoidance purposes. Orbit determination methods yield the position of a satellite at a given time in the future.

1.1 Motivation and Background

Bright moving objects in the sky have intrigued mankind since ancient history began. Ancient people worshiped heavenly bodies as Gods. They developed timekeeping systems to facilitate their daily lives. They used stars to navigate in deserts and seas. They made observations to figure out the motion of celestial bodies. It was Johannes Kepler who first developed the three laws of planetary motion in 1619. Kepler's empirical findings, based on Tycho Brahe's planetary observations, were explained by Isaac Newton in his book "Principia" in 1687. Isaac Newton used his three laws of motion to derive Kepler's laws of planetary motion. Kepler's equations serve as a complete solution to the two-body problem (2BP), which determines the mutual gravitational interaction of two bodies under the assumption that there is no third body affecting them. The solution to the 2BP assumes that there is no perturbing force affecting the two body motion. The formulation of the three-body problem (3BP) was provided by Joseph Louis Lagrange in 1772. The

1

3BP is a special case of the n-body problem (NBP). It is the problem of calculating mutual gravitational interaction of three bodies.

At the end of the 18th century, remarkable advances occured in perturbation theory due to the logarithms invented by John Napier in 1614 and the efforts in modeling the Earth's gravitational field. Perturbations can be defined as the divergence from the normal motion. The motion of a body under the influence of small accelerations diverges from the two body motion. There are three different methods to find perturbations to the two body motion: special perturbation techniques, general perturbation techniques, and semianalytical techniques. Special perturbation techniques rely on numerical integration techiques and require high computational power. Numerical integration methods provide orbit predictions with a level of accuracy in meters. General perturbation techniques make use of analytical solutions to the perturbation problem and do not require much computational power. However, predictions made by general perturbation techniques are not as accurate as that of numerical methods. Semianalytical techniques combine special and general perturbation techniques to compensate for their disadvantages [60].

Precise orbit prediction is of great importance in the space age. Accurate positions of operational satellites help us to communicate with them. Antennas are useless if they are not pointing to the right direction, unless they are omnidirectional. Nonoperational satellites and debris pose threats to operational satellites. Accurate orbit estimation is very important for collision avoidance because wrong maneuver decisions cannot only result in the loss of millions of dollars but also create thousands of pieces of debris. Moreover, accurate predictions for the reentry of returning space objects are very important for two reasons. First, space objects returning from space might pose threats to people. Second, space assets returning from space might contain hardware or software important to the national security. Therefore, U.S. Space Surveillance Network (SSN) detects, tracks, and catalogs debris, operational and nonoperational satellites every day. SSN has more than

23,000 objects orbiting Earth in its database. [54].

North American Aerospace Defense Command (NORAD) publishes Two-Line Element (TLE) sets of some satellites to promote situational awareness in space. Special General Perturbations 4 (SGP4) is the current method of NORAD to propagate orbits from raw observational data coming from radars. However, SGP4 is accurate in the vicinity of epoch time. SGP4 is based on general perturbation techniques. Therefore, it suffers from errors that emerge from omission of higher order terms in the equations of motions, and its predictions are accurate only in kilometers. SGP4 requires observational data to make corrections once every few days. However, it is very fast in terms of computation time. Special perturbation techniques are used if more accurate predictions are needed. For example, the success of a collision avoidance intrinsically depends on accuracy in the positions of objects in danger of collision. The downsides of numerical integration methods are truncation errors in the long run due to the limited word length of computers, high computational cost, and difficulty in determining whether the resultant orbit is the one that is desired. Moreover, the breakup of satellite 1961-Omicron in 1961 proved that heavily dependence on numerical methods that requires high computational power for the sake of accuracy is not reliable. In 1961, the breakup tripled the number of debris to be tracked. The Naval Ordinance Research Calculator (NORC), which was at the Naval Weapon's Laboratory (NWL) in Dahlgren, was insufficient to cope with the surveillance data flow and the orbital updates. Recently acquired IBM 7090, which was three times faster than NORC in terms of computational power, and incredible human effort processed the data in a few days. That catastrophic event has been second to none since then. However, lessons were well learned. It is crucial to have accurate orbit determination models that don't require as much computational power as special perturbation techniques [26]. Therefore, a new method for orbit prediction, which is as accurate as numerical methods and as fast as analytical methods, in terms of computational time, would be very desirable.

1.2 Problem Statement

This work will answer the question of whether best low eccentricity Kolmogorov Arnold Moser (KAM) tori fitted to the orbits, using TLE histories of satellites, produce more accurate predictions for low eccentricity orbits than SGP4 does. Moreover, this effort presents an approximate accuracy analysis for the low KAM torus orbit prediction because both SGP4 and TLE suffer from intrinsic inaccuracies. The actual accuracy that can be achieved by this theory can be analyzed using raw observational data.

A previous study by Frey showed that it is possible to extract KAM torus basis frequencies from SGP4 and TLE sets. Frey concluded that low eccentricities of Hubble Space Telescope (HST) and Thor Rocket Body caused difficulties in the construction process of KAM torus, and the difficulties in the TLE curve fitting for the two Delta Rocket Bodies are due to air drag. Frey used a modified Laskar frequency algorithm, developed by Wiesel, to determine KAM torus basis frequencies [28]. Laskar fequency analysis is used to determine the stability of orbits in dynamical systems where the energy is conserved.

Because the modified Laskar frequency algorithm cannot model low eccentricity orbits to the desired degree of accuracy, Wiesel developed a new theory for low eccentricity Earth satellite motion to construct KAM torus. This work will make use of this new theory to build KAM torus for low eccentricity orbits. This KAM torus construction method includes geopotential, order and degree 20, and air drag perturbations[69].

1.3 Approach

This effort uses three different main programs to prove KAM torus orbit prediction from TLE sets provides more accurate predictions in the long run than SGP4 and TLE sets. The first main program is a public domain SGP4 program written in C++ by Vallado [61]. It outputs predicted positions and velocities for an orbit period and some orbital elements by making use of TLE sets of satellites. TLE sets of satellites with low eccentricities are

4

obtained from www.space-track.org once every 3 to 4 days for a period of 2 months. NO-RAD imports corrections to SGP4 predictions with observational data coming from radars once every 3 to 4 days. The second main program, developed by Wiesel, builds a low eccentricity KAM torus including zonal, sectoral, and tesseral geopotential perturbations, and air drag perturbations. The third main program is a least squares fitting program that fits a low eccentricity KAM torus to SGP4 and TLE data by iteratively correcting modal variables, which are KAM torus coordinates and their linearizations, and basis frequencies of the KAM torus, and subsequently outputs residual mean square values. The methodology is based on the concept, which is very similar to that of the least squares method, that it is possible to obtain more accurate results with more data, and SGP4 is more accurate when nearer to the epoch time. The author has developed some scripts to analyze all low eccentricity satellites, which have eccentricities smaller than 10^{-2}, and inclinations not close to critical and polar inclination. There are 7,938 satellites and pieces of debris correspond with the above description, which can be publicly obtained from www.space-track.org. However, the author has pseudo-randomly chosen 1500 of these 7,398 near-Earth objects as his test cases. This effort serves as a prelude to converting the TLE sets catalog from SGP4 to low eccentricity KAM torus theory.

1.4 Results

This effort proves that the low eccentricity KAM theory is a better substitute for SGP4. The new theory is five times more accurate for the best fits, and three times better for mean fits. Most of the low eccentricity orbits of the near-Earth objects can be modeled by the low eccentricity KAM torus method. However, resonance, higher eccentricity, polar and critical inclinations, and air drag issues should be addressed. The results are certainly promising. Specifically, the new method can be used for collision avoidance calculations, and formation flight applications. The new method provides with a set of numerical algorithms that

may rival the numerical methods in accuracy and the analytic methods in computational speed. This work also presents a rigorous performance analysis of the theory, which will be hopefully used as a reference for future studies.

1.5 Overview

This document is organized in five chapters. Chapter II will present previous studies conducted by Wiesel and his masters and PhD students on KAM torus orbit determination. It will also give an overview of the history of analytical orbit modeling in the United States space surveillance system, satellite dynamics formulated in Hamiltonian mechanics, KAM theory, the geopotential and air drag as perturbing forces, and least squares fitting. Chapter III will discuss the methodology and the data to be analyzed. It will also outline predicting positions and velocities from TLE and SGP4, building low eccentricity KAM tori, and fitting the low eccentricity KAM tori to the orbits obtained from SGP4 and TLE. Chapter IV will present the results and limitations of KAM torus orbit prediction method. It will also compare the accuracy of the new method to that of SGP4 and TLE. A general summary of the work, conclusions, and recommendations for future studies will be presented in Chapter V.

II. Background

This chapter provides background information on current orbit determination methods, near-Earth satellite motion, and KAM theory. First, a brief history of analytical orbit modeling in the United States Space Surveillance System is presented. Then, the importance of the space situational awareness is presented. Next, Hamiltonian mechanics, transformation theory, orbit perturbations, and KAM theory are described. Then, the application of KAM theory to celestial mechanics is presented. After that, the previous studies of Wiesel and his masters and PhD students on the applications of KAM theory to Earth satellites are provided in chronological order. Finally, a summary of this chapter will be given.

2.1 A Brief History of Analytical Orbit Modeling

After the launch of Sputnik in 1957, United States started to track space objects. Today, SSN database has more than 23,000 space objects orbiting earth [54]. Earth orbiting objects are cataloged by analytical orbit models. The analytical methods have been mostly developed by the Air Force Space Command and the Naval Space Command. The development and improvement of orbital models and algorithms span from 1957 to today [26].

The necessity of knowing orbital positions of space objects emerged due to military concerns in 1957. The Air Force used it not to confuse a missile with an object orbiting Earth, and the Navy used it to warn the fleets against space reconnaissance. The potential benefits from artificial satellites led to great interest in the accurate positions of the satellites for the civilian world. Therefore, the catalog for Earth orbiting objects was created, and it is still in use today [26].

The first formal catalog was created at the National Space Surveillance Control Center (NSSCC). The control center was located in Bedford, Massachusetts. The observational data were provided by 150 different sites. There were 4 different types of observations,

which were categorized by their source and content. Table 1 shows details of different observational data types used from the year 1957 to 1963 [26].

Table 1. Observational Data Types [26]

Observation Type	Content	Source
Type 1	2 angles and slant range	Radars
Type 2	2 angles	Baker-Nunn cameras, telescopes, binoculars, visual sightings
Type 3	Azimuth	Direction finders
Type 4	Time of closest approach (Doppler)	Radars, radio receivers (for transmitting satellites)

Observations were processed by an IBM-709 computer to update orbital elements in the catalog, which were some type of mean orbital elements. Then, updated orbital data were processed by another program to yield three different products, which were used to make observations for the next time by ground sites. The first product, called bulletin, was the precursor of the TLE sets. The most important components of a bulletin were longitude, time of ascending pass, and revolution number of a satellite. These were generated approximately a week in advance. The second product was used to calculate all satellite passes, which could be seen from an observing site. The third product was very similar to the second product. However, the third one was used by the U.S. Navy and U.S. Army observation fences, which were composed of a number of radars. Therefore, the third product was used to yield the intersection point of orbital plane of a satellite and vertical plane spanned by radar beam instead of some look angles and ranges [26].

In 1961, U.S. Navy constructed the Naval Space Surveillance System (NAVSPASUR), which detected and cataloged Earth orbiting objects mostly without human intervention. The processing unit for NAVSPASUR was located at Dahlgren, Virginia. The system was a continuous wave multi-static interferometer, which observed LEO satellites 4 to 6 times a day. There were 3 transmitters and 6 receivers, which spanned from San Diego, California

to Savannah, Georgia as 9 individual sites located in the Southern States. The system was called "Fence". The command of the Fence, which was responsible for 40% of all observations made by the Air Force, was passed to U.S. Air Force in 2004. The U.S. Air Force shut down the system in October 2013. A new fence is planned to be operational in 2017 in the Marshall Islands [19].

Special perturbation techniques were thought to be used in the Fence until it was discovered that it took the NORC at the NWL several hours to update one orbit. In 1961, the catalog was transferred to an IBM-7090 computer, which reduced the time required to update one orbit to approximately 1 minute. That was very promising for the implementation of highly numerical methods, which yield more accurate predictions. However, the breakup of 1961-Omicron tripled the number of objects to be tracked. The number of detectable objects exceeded the capability of the NORC. The IBM-7090 and incredible human effort processed the data in a few days. Although special perturbation techniques provide with more accurate predictions, the beakup of satellite 1961-Omicron proved that accurate analytical models are needed in case computers fail to process the data [26].

In 1959, Dirk Brouwer and Yoshide Kozai provided two different solutions to the same problem, which was Earth satellite motion under the influence of the zonal harmonics J2, J3, J4, and J5 [9, 38]. Modern orbit prediction methods used in the U.S. Space Surveillance System include fundementals of the solutions provided by Brouwer and Kozai. In 1961, Brouwer and Gen-Ichiro Hori added atmospheric drag effect to the 1959 Brouwer solution [10]. However, the atmospheric model was computationally heavy for the computers of the time due to the series expansions in the scale height. In 1960, a group of people under the project SPACETRACK developed an atmospheric density modeling, which solved the series expansion problem for artificial satellites. Max Lane developed an analytic orbit model based on the atmospheric density modeling of the SPACETRACK in 1965 [40]. Lane and Cranford improved the analytic orbit model by implementing analytic density

9

model instead of empirical one in 1969 [42]. In 1963, Lyddane contributed to the analytic orbit modeling by solving small divisors of the eccentricity and sine of the inclination by defining the perturbation theory in terms of Poincaré variables instead of Delaunay variables [49].

Conversion from theory to practice for analytical orbit models took place in Dahlgren, Virginia, and Colorado Springs, Colorado. NAVSPASUR implemented the 1959 Brouwer solution with Lyddane's contribution, which was known as PPT (Position and Partials as a function of Time), on an IBM-7090 computer in 1964. PPT adopted semi-empirical drag model developed by Richard H. Smith because the atmospheric model of Brouwer and Hori was computationally heavy for the computers of the time, and it was too early for the Lane's analytic orbit model. The change in the eccentricity could be solved using Equation 1 and Equation 2.

$$\dot{e}_o = e_o(1 - e_o^2)\frac{\dot{a}_o}{a_o} \tag{1}$$

$$\dot{a}_o = -\frac{4}{3}\frac{a_o}{n_o}(\frac{\dot{a}_o}{2}) \tag{2}$$

Numerically, mean motion term in PPT is similar to Kozai's mean motion, which has the zonal secular perturbation rate of mean anomaly drived by Brouwer.

NSSCC was moved to Colorado Springs, and named as Space Detection and Tracking System (SPADATS). SPADATS is the other location for the implementation of the analytic orbital theory, which was called SGP (Simplified General Perturbations), developed by Brouwer and Kozai. Arsenault, Chaffee, and Kuhlman avoided small divisors of the eccentricity and sine of the inclination in SGP by defining the solution in non-singular terms and keeping only the most important ones in the model. They included long and short-period terms without the eccentricity effect from the Brouwer solution and the con-

vention that relates mean motion to semi-major axis from the Kozai solution [33]. The air drag effect used in SGP was very similar to Smith's semi-empirical model. In 1969, Lane and Cranford developed an analytic atmospheric model for artificial satellites [42]. However, computers of the time were inadequate to cope with calculations required for the new model. Therefore, the most important terms of the atmospheric model were implemented to the analytical orbit model, which is now called SGP4. Today, some flavor of SGP4 is used by NORAD [26].

Solar and Lunar gravitation, and resonance in the tesseral harmonics of Earth became important when the first satellite with a period of 12 hours was launched in 1965. Bruce Bowman developed a model which includes third body effects, and resonance in the tesseral harmonics of Earth in 1967 [7]. In 1977, Dick Hujsak developed another model which includes everything from Bowman's work. Moreover, his first-order model could be applied to geosynchronous satellites [32]. Hujsak's model was combined with the SGP4 model, which is still in use today. In 1997, third body effects, and resonance in the tesseral harmonics of Earth were adopted from SGP4 by the Naval Space Command. The new method, which is still in use today, is called PPT3 [26].

2.2   Space Situational Awareness

In less than six years from the launch of Sputnik 1 to 1963, 616 man-made objects accumulated in low Earth orbit (LEO). Those man-made objects were 76 payloads, 35 rocket bodies, and 227 mission related debris. The U.S. Ablestar upper stage explosion created 184 pieces of objects which were half of all the objects cataloged by SSN in 1963, and 60% of all debris from this explosion is still orbiting Earth [54]. Today, 23,000 objects are cataloged by SSN and the majority of these objects are not operational satellites but debris and nonoperational satellites, which is approximately 95% of total number of objects being cataloged [59].

11
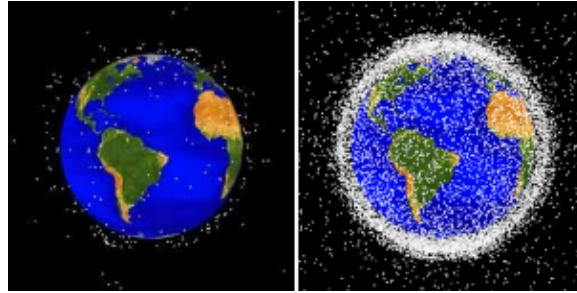
Figure 1. Cataloged objects by SSN in 1963 (left) and in 2013 (right) [54]

The rate of growth in the number of debri objects in less than six years was noticed by Ernest Peterkin, Head of the Systems Section of the Operational Research Branch at the U.S. Naval Research Laboratory. He was one of the first to calculate the number of objects per unit volume in LEO in February 1963. He derived population growth functions for the objects in LEO using estimates for launch rates, lifetimes of satellites, and satellite collisions. Peterkin's conclusions showed that there would be 16,500 objects in LEO at the beginning of 2013. His predictions are very close to the number of objects cataloged by SSN on 1 January 2013. Peterkin concluded that space surveillance systems would have difficulty coping with the rapid growth in the number of objects orbiting Earth in the future. He stated that it is important to improve detection and data processing methods used in space surveillance systems to manage the increase in the number of objects orbiting Earth [54]. This effort is trying to find an accurate and a fast orbit prediction method which can help space surveillance systems to cope with the proliferation of objects orbiting Earth. Low eccentricity KAM theory yields more accurate orbit predictions than SGP4. In addition, this work shows that it is possible to extract valuable data, which are used by the low eccentricity KAM torus orbit prediction method to make corrections to low eccentricity KAM tori, from inaccurate TLEs in the long run.

The Joint Space Operations Center (JSpOC), located at Vandenberg, is responsible for detecting, tracking, and cataloging all man-made objects orbiting Earth. JSpOC uses SSN which has 30 space surveillance radars and optical telescopes all over the world. The radar
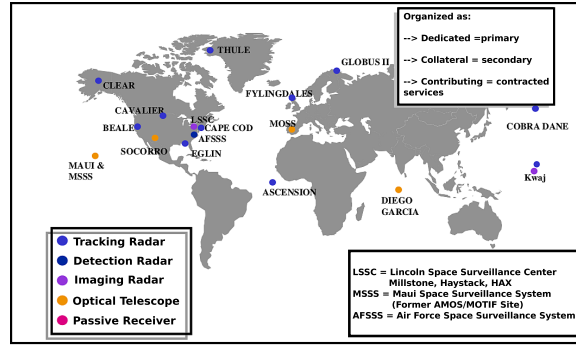
Figure 2. Worldwide network of space surveillance sensors of SSN [55]

sensors are dedicated to make observations for near-Earth objects, which are below 6000 kilometers altitude. The electro-optic sensors are dedicated to make observations for deep-space objects, which are above 6000 kilometers altitude. Azimuth, elevation, range, and range rate are typical observation types obtained from a radar site. Azimuth and elevation or right ascension and declination are observations provided by an optical sensor. Observations made by SSN include time tags [37]. Figure 2 shows locations of worldwide network of 30 space surveillance sensors. Observational data obtained by these sensors are fitted to the trajectories of orbiting objects, and the satellite catalog is continuously updated. SSN makes 380,000 to 420,000 observations every day. SSN implements a predictive surveillance method because all objects orbiting Earth cannot be covered by existing sensors, which requires efficient analytic orbit models. These observations are important for operational satellites because collision analyses are made using orbit predictions in the satellite catalog [59].

This effort is beneficial for satellite communities which use NORAD TLE for propagating orbits of the objects that pose threat to their space assets because low eccentricity KAM theory can yield position and velocity data to create TLEs before NORAD publishes them. NORAD publishes a new element set when the difference of positions predicted by the current and the new element sets exceed 5 km with a 90% confidence interval. LEO satellites require more frequent updates due to the atmospheric drag. Maneuverable satel-

13

lites also need more frequent updates because orbital maneuvers cannot be modeled by SGP4 [37]. This work uses Vallado's public domain SGP4 with differential corrections to determine the accuracy of the orbit predictions yielded by low eccentricity KAM theory because JSpOC version of SGP4 has no technical details and codes available to public.

2.3 Orbit Prediction using SGP4 and TLE

TLEs are some type of mean elements which are averaged, and smoothly changing over time or angle. Some period of time, mean anomaly, true anomaly, and eccentric anomaly can be used to average the elements [60]. TLEs are used by NORAD, and the majority of the satellite community. NORAD TLE is the default input for most of the commercialized satellite ground antenna control system and orbit analysis programs [46]. TLE is generated from observational data flow from SSN using one of five orbit prediction methods of NORAD. The first one is SGP which was developed by Hilton and Kuhlman [31], and simplified by the work of Kozai in terms of gravitational and air drag effects [38]. SGP is used for satellites with a period less than 225 minutes. The second one is SGP4 which was developed by Cranford in 1970 [41], and simplified by adopting analytic atmospheric model of Lane and Cranford instead of empirical atmospheric model in 1969 [42]. Table 2 shows parameters required to initialize SGP4. All of the parameters but mean motion are mean orbital elements defined by Brouwer [9]. Brouwer's mean elements include only the effects of the zonal harmonics which are J2, J3, J4, and J5. SGP4 includes orbital mean elements and their linearizations defined in series expansions. Many assumptions are made for SGP4. For example, Earth's gravitational potential includes only a few zonal terms, the atmospheric model is a static model with an assumption of exponential decay, and the third-body mass and resonance effects are partially added to the model [62]. Mean motion in the Table 2 includes only short-period oscillations similar to Kozai's mean motion [38]. Long-periodic oscillations are masked by air drag, which gradually increases mean motion

14
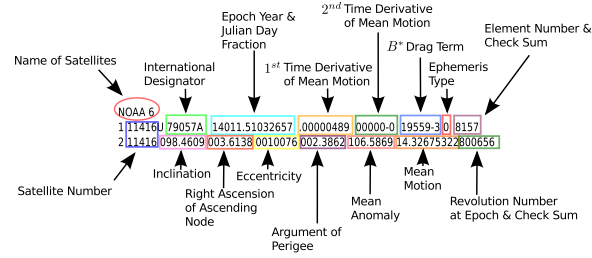
Figure 3. TLE Example for NOAA-6 Weather Satellite

over time, for LEO satellites [28].

Table 2. Parameters to Initialize SGP4 Propagation

Symbols	Description
t_o	Epoch time
n_o	Mean motion at epoch
e_o	Eccentricity at epoch
i_o	Inclination at epoch
ω_o	Argument of perigee at epoch
Ω_o	Right ascension of the ascending node at epoch
M_o	Mean anomaly at epoch
B^*	Atmospheric drag coefficient

The third one is SDP4 which is developed for orbits with a period more than 225 minutes by Hujsak in 1979 [32]. SDP4 includes third-body, sectoral, and tesseral effects, whereas SGP4 doesn't. The fourth one is SGP8 which is applicable to near-Earth satellites. SGP8 depends on the model of Lane and Cranford for gravitational and air drag effects [42]. The integration of differential equations are treated in a different way for SGP8 than SGP4. The fifth one is SDP8 which is a deep-space model. SGP8/SDP8 were introduced to decrease the effects of the deficiencies of SGP4/SDP4 associated with reentry and orbital decay [62]. A TLE should be used with one of these models because periodic variations are removed in a way that these five models can compensate for them. Figure 3 shows an example of a NORAD TLE with descriptions of each elements.

Orbit prediction methods are divided into three different catagories: special perturba-

tion techniques, general perturbation techniques and semianalytical techniques. Special perturbation techniques use numerical methods to make predictions. However, numerical methods are prone to errors due to limited word length of computers. Moreover, long time steps for integrations result in round-off errors. Special perturbation techniques cannot be generalized to other orbits because the predictions are special to the orbit that is integrated. Special perturbation techniques provide predictions accurate in meters. However, they require high computational power. All perturbations are calculated for every point in time in special perturbation techniques. General perturbation techniques use closed form solutions to equations of motions of orbits. The complexity of equations of motions requires omission of higher order terms in the equations. The accuracy of the predictions degrades rapidly due to these omissions. In addition, orbit predictions made by general perturbation techniques are not as accurate as those provided by special perturbation techniques. However, general perturbation techniques provide orbit predictions without calculating every intermediate points to find the desired point in the future and take an average of all perturbations over time as one parameter which can be integrated into the equations. Therefore, they are very fast in terms of computation time. SGP4 orbit determination method is such a general perturbation technique. Semianalytical techniques combine advantages of analytical methods and numerical methods.

Equation 3 shows the relationship between the SGP4 model and the state vector of a satellite.

$$y(t) = f_{SGP4}(x_o, B^*, t), \tag{3}$$

where f_{SGP4} is the SGP4 model, $y(t)$ is the velocity and position vectors at time t, x_o is the mean orbital elements, which are shown in the Table 2 excluding t_o and B^*, at the epoch time. The epoch time is represented as t_o [46]. Equation 4 shows how the ballistic coefficient, B, and the atmospheric reference reference density ρ_o are related to NORAD

16

SGP4 air drag term B^* [52].

$$B^* = \frac{1}{2} B \rho_o \tag{4}$$

Equation 5 can also be used to produce the NORAD TLE given osculating elements and a good approximation for the NORAD TLE. Equation 5 shows the relationship between osculating elements and the NORAD mean elements. B^* is missing in the Equation 5 because SGP4 can't model the air drag term. Therefore, B^* needs to be calculated separately [46]. B^* is important for the accuracy of the NORAD TLE. The omission of B^* value of 10^{-4} could worsen the accuracy of SGP4 twice as much within approximately 3 days [45].

$$y_i = f_{SGP4_i}(x_1, ..., x_6), \tag{5}$$

where i=(1,$\cdots$,6), and y_i are osculating elements, x_i are the NORAD mean elements. Equation 5 can be expanded around x_i^a, which are good approximations for the NORAD mean elements, using Taylor series expansion. Equation 6 and Equation 7 show the linear system of equations after taylor series expansion [45].

$$\Delta y_i = M \Delta x_i, \tag{6}$$

$$M = \begin{bmatrix} \frac{\partial f_{SGP4_1}}{\partial x_1^a} & \frac{\partial f_{SGP4_1}}{\partial x_2^a} & \cdots & \frac{\partial f_{SGP4_1}}{\partial x_6^a} \\ \vdots & \vdots & \ddots & \vdots \\ \frac{\partial f_{SGP4_6}}{\partial x_1^a} & \frac{\partial f_{SGP4_6}}{\partial x_2^a} & \cdots & \frac{\partial f_{SGP4_6}}{\partial x_6^a} \end{bmatrix}, \tag{7}$$

where $\Delta y_i = y_i - y_i^a$, and $\Delta x_i = x_i - x_i^a$. Partial derivatives in matrix M are hard to solve due to the coupled nature of the SGP4 model. Newton's quotient can be used to find the partial derivatives [25]. Equation 8 shows one of the partial derivatives in the difference quotient

notation [45].

$$\frac{\partial f_{SGP4_1}}{\partial x_1^a} = \frac{f_{SGP4}(x_1^a + \Delta x_1^a, x_2^a, \cdots, x_6^a) - f_{SGP4}(x_1^a, x_2^a, \cdots, x_6^a)}{\Delta x_1^a},$$ (8)

where Δx_i^a can be some small increment of percentage of x_i^a. The NORAD mean elements can be approximated using a process called differential corrections. The iterative process is stopped when the difference between the given osculating elements and derived ones, which are $(y_i - y_i^a)$, are small enough for convergence. Equation 8 shows the iterative process to approximate the NORAD mean elements [45].

$$x_i^{a+1} = x_i^a + \sum_{j=1}^{6} M_{ij}^{-1}(y_i - y_i^a),$$ (9)

where i=(1,$\cdots$,6).

There are inevitable deficiencies in the SGP4 theory. Because SGP4 is an analytic orbit model, it ignores higher order terms in the equations of motion. Moreover, sectoral and tesseral gravity field perturbations are not included in the model. The SGP4 model includes only the effects of the zonal harmonics which are J2, J3, J4,and J5. Therefore, the SGP4 model yields position errors of 2 km at epoch time [52]. The velocity predictions made by the NORAD TLE and the SGP4 are less accurate than the position predictions because the rates of change in the orbital parameters, which are not accurate due to inevitable deficiencies in the SGP4 theory, are used to calculate velocities [28].

The accuracy of the Vallado's SGP4 with differential corrections for near-Earth objects are on the order of magnitude of 100 km. The prediction accuracy worsens with decreasing altitude, and increasing eccentricity and solar flux. Table 3 and Table 4 show the SGP4 orbit prediction accuracy of the near-Earth objects in terms of the root mean square values with respect to two different solar flux values [24].

Table 3. The Orbit Prediction Accuracy of the Near-Earth Objects ($F_{10} = 100$)[24]

Altitude(km)	Test Cases	1day(km)	3days(km)	7days(km)	15days(km)
h<400	57	4	10	60	300
400≤h<600	168	3	10	50	100
600≤h<1200	267	3	10	20	50
1200≤h<7000	90	2	10	10	20

Table 4. The Orbit Prediction Accuracy of the Near-Earth Objects ($F_{10} = 200$)[24]

Altitude(km)	Test Cases	1day(km)	3days(km)	7days(km)	15days(km)
h<400	57	10	40	300	1000
400≤h<600	168	7	30	200	400
600≤h<1200	267	6	15	70	100
1200≤h<7000	90	2	10	10	20

2.4 Reference Frames

Reference frames are important for classical and analytic mechanics. All equations of motions are written in some frame of reference. The first step in solving a dynamical problem is defining the reference frame. There are two different types of reference frames, which are inertial and rotating frames. There is no solution for any dynamical problem in classical mechanics unless an inertial frame is defined. This effort formulate satellite
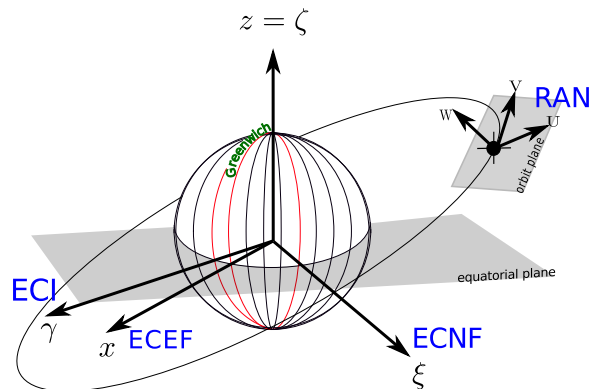
Figure 4. Reference Frames

Table 5. Reference Frames

Acronym	Reference Frame	Type	Origin	1st **axis**	2nd **axis**	3rd **axis**
RAN	Radial, Along-Track, and Normal	Rotating frame	Space object CoM	Toward radial direction (U)	Normal to orbital frame (W)	Along velocity direction (V)
ECI	Earth-Centered-Inertial frame	Inertial frame	Earth CoM	Toward vernal equinox (γ)	Completes right-handed frame (ε)	Earth's axis of rotation (ζ)
ECEF	Earth-Centered-Earth-Fixed frame	Rotating frame	Earth CoM	Toward prime meridian in equatorial plane (x)	Completes right-handed frame (y)	Earth's axis of rotation (z)
ECNF	Earth-Centered-Node-Fixed frame	Rotating frame	Earth CoM	Toward ascending node in equatorial plane (ξ)	Completes right-handed frame (η)	Earth's axis of rotation (ζ)

motion using 4 different reference frames, which are defined in Table 5 and Figure 4.

Reference frames in Table 5 are helpful in different ways for this effort. RAN reference frame is used to make residuals between SGP4 and low eccentricity KAM theory predictions meaningful because it is hard to analyze the residuals in ECI frame. ECNF reference frame is important because orbits are not periodic in ECI frame although they are in ECNF frame. Periodic orbits are not periodic in ECI frame because orbital plane regresses due to the zonal potential. Moreover, the Keplerian frequency is defined in a frame which is tied to the node of the orbit. Thus, it can simply be generalized to ECI and ECEF frame because the zonal potential is symmetric about the earth's polar axis. Greenwich referenced ECEF frame simplifies calculations because the gravitational field potential is constant in ECEF

frame.

2.5   Analytical Dynamics

Equations of motions are formulated using momentum and force in Newtonian mechanics. Objects and forces applied on them are considered separately. For Newtonian mechanics, constraint forces, which are forces that do no work, may be needed to solve dynamical problems. However, analytical dynamics considers a dynamical system as a whole not separately. For analytical dynamics, equation of motions are formulated using kinetic energy and work, which are both scalar quantities. Therefore, constraint forces are not needed to solve dynamical problems. Dynamical systems in analytical dynamics are defined in generalized coordinates, which are finite, continuous, and differentiable with respect to time. In addition, generalized coordinates aren't restricted to be physical quantities. Number of generalized coordinates for a system equals to the number of degrees of freedom that the system has [51]. Many complex dynamical systems can be solved without much effort using analytical dynamics. Figure 5 shows the evolution of transition from Newtonian to Lagrangian mechanics.

Principle of Virtual Work

↓

D' Alembert Principle

↓

Hamilton's Law

↓

Hamilton's Principle (Hamilton's Extended Principle)

↓

Lagrange's Equations
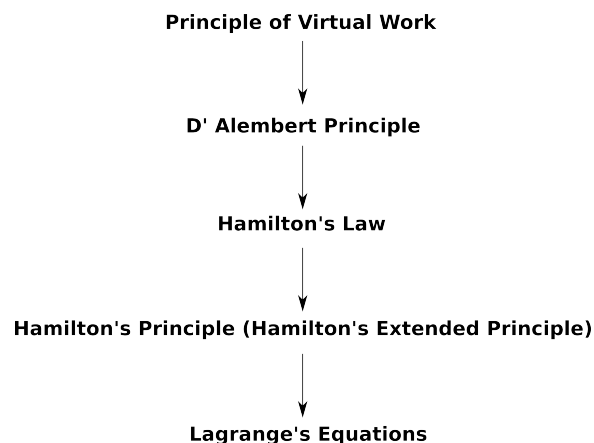
Figure 5. Evolution of the Transition from Newtonian to Lagrangian Mechanics

Principle of virtual work is based on static equilibrium of a system. It is the first variational principle in mechanics [51]. Constraint forces are perpendicular to virtual displace-

ments. However, formulation of equations of motions relies on forces. Equation 10 and Equation 11 show the virtual work of the entire system equals to zero.

$$\overline{\delta W} = \sum_{i=1}^{N} F_i \cdot \delta r_i + \sum_{i=1}^{N} F_i' \cdot \delta r_i = 0, \tag{10}$$

$$\sum_{i=1}^{N} F_i' \cdot \delta r_i = 0, \tag{11}$$

where F_i are external forces, and F_i' are constraint forces applied on the system. δr_i are virtual displacements.

D' Alembert's principle is an extension of principle of virtual work to dynamics. D' Alembert's principle treats dynamical problems as if they were statical. Equation 12 shows the most general formulation of dynamics [51].

$$\sum_{i=1}^{N} (F_i - \dot{p}_i) \cdot \delta r_i = 0, \tag{12}$$

where $\dot{p}_i$ is rate of change of the momentum, which is also called inertia force.

Hamilton's law is important because it depends on kinetic and potential energy instead of force and momentum. Both principal of virtual work and D' Alembert's principle are similar to Newtonian mechanics in formulating equations of motion because they all depend on force and momentum. The first step in transition from D' Alembert's principle to Hamilton's law is integrating D' Alembert's principal equation over a finite period of time, and expressing momentum in terms of kinetic energy. The derivation of Hamilton's law introduces Lagrangian, which is the difference between kinetic and potential energy. Equation 13 represents Hamilton's law of varying action. Hamilton's law of varying action is valid for non-linear, non-conservative, non-stationary dynamic systems. Variations of the generalized coordinates δq_j aren't necessarily zero because the system state q_j isn't always known at time t_1 and t_2, which shows the system is non-stationary. Variation of any

constant value equals to zero [39].

$$\int_{t_1}^{t_2} \delta L dt + \int_{t_1}^{t_2} \overline{\delta W} - \sum_{j=1}^{N} \left(\frac{\partial T}{\partial \dot{q}_j} \delta q_j \right) \Big|_{t_1}^{t_2} = 0, \tag{13}$$

$$L = T - V, \tag{14}$$

where L is Lagrangian, T is kinetic energy, and V is potential energy.

Hamilton's principle is an extension of Hamilton's law. For Hamilton's principle, the generalized coordinates δq_j are assumed to be known at end points t_1 and t_2. Hamilton's principle is applicable when there are no non-conservative forces, whereas extended Hamilton's principle is applicable when there are non-conservative forces in the system. Equation 15 shows Hamilton's principle, and Equation 16 shows extended Hamilton's principle [39]. Hamilton's principle is a variational principle which reduces a dynamical problem to a scalar integral independent of coordinates, which describes Lagrangian. Equations of motion are obtained by figuring out the conditions which make the scalar integral stationary. Figure 6 represents true path and varied path, which the true path coincide with two end points t_1 and t_2. The varied path is formed when the virtual displacements is applied, which by definition, has no change in δr_i [51].

$$\int_{t_1}^{t_2} \delta L dt = 0 \tag{15}$$

$$\int_{t_1}^{t_2} \delta L dt + \int_{t_1}^{t_2} \overline{\delta W} dt = 0 \tag{16}$$

Lagrange equations are n number of coupled second-order differential equations, which has n number of generalized coordinates. Lagrange equations are derived from Hamilton's
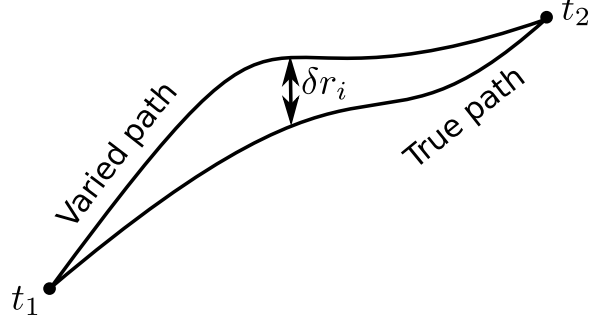
Figure 6. True Path and Varied Path

law of varying action as [39]:

$$\int_{t_1}^{t_2} \delta L(q_i, \dot{q}_i, t)dt + \int_{t_1}^{t_2} \overline{\delta W} - \sum_{j=1}^{N} \left(\frac{\partial T}{\partial \dot{q}_j} \delta q_j \right) \bigg|_{t_1}^{t_2} = 0 \tag{17}$$

After calculating the variation of the Lagrangian,

$$\sum_{i=1}^{N} \int_{t_1}^{t_2} \left(\frac{\partial L}{\partial \dot{q}_i} \delta \dot{q}_i + \frac{\partial L}{\partial q_i} \delta q_i \right) dt + \int_{t_1}^{t_2} \overline{\delta W} - \sum_{j=1}^{N} \left(\frac{\partial T}{\partial \dot{q}_j} \delta q_j \right) \bigg|_{t_1}^{t_2} = 0 \tag{18}$$

After integrating Lagrangian terms by parts, and cancelling the trailing term, which shows the system could be non-stationary,

$$\sum_{i=1}^{N} \int_{t_1}^{t_2} \left[\frac{d}{dt} \left(\frac{\partial L}{\partial \dot{q}_i} \right) - \frac{\partial L}{\partial q_i} - Q_i \right] \delta q_i dt = 0, \tag{19}$$

where Q_i is generalized force. The integrand can be equated to zero because the system can be considered stationary. Equation 21 shows Lagrange's equations when there is no non-conservative force in the system because virtual work equals to zero.

$$\frac{d}{dt} \left(\frac{\partial L}{\partial \dot{q}_i} \right) - \frac{\partial L}{\partial q_i} - Q_i = 0 \tag{20}$$

24

$$\frac{d}{dt}\left(\frac{\partial L}{\partial \dot{q}_i}\right) - \frac{\partial L}{\partial q_i} = 0 \qquad (21)$$

2.6 Hamilton's Equations

The Hamiltonian formulation is an alternative to the Lagrangian formulation [16]. They both have the same physics. The Lagrangian formulation has n number of second-order differential equations, whereas the Hamiltonian formulation has 2n number of first-order differential equations. The Lagrange's equations describe mechanics in terms of generalized coordinates and velocities, whereas the Hamilton's equations rely on the generalized coordinates, q_i, and momenta, p_i [29]. Equation 22 shows the equation for the generalized momenta. The generalized momenta can be described as linear functions of the generalized velocities. Conversely, the generalized velocities can be shown to be linear functions of the generalized momenta [51]. The Legendre transform of the Lagrangian yields the Hamiltonian. Equation 23 shows the Hamiltonian.

$$p_i = \frac{\partial L(q_i, \dot{q}_i, t)}{\partial \dot{q}_i}, \qquad (22)$$

$$H(p, q, t) = \sum_i \dot{q}_i p_i - L(q, \dot{q}, t), \qquad (23)$$

where $H(p, q, t)$ is Hamiltonian, which can fully describe the motion [51].

The Hamilton's formalism are more powerful than Lagrange formalism. The apparent advantage of the Hamilton's equations over Lagrange equations is that time derivatives of the variables are on the left side of the equations, which may help to figure out first integrals of motion. Moreover, the Hamilton's equations are favorable in representing the solution in geometrically because 2n-dimensional representation is advantageous in representing not only one path but totality of paths, which are all possible solutions. In Hamiltonian

phase space, the velocity of every point can be determined uniquely, whereas the motion can start in any direction, and paths may intersect in the Lagrangian configuration space, which makes totality of paths confusing [51]. The canonical equations of Hamiltonian can be derived from the Hamiltonian as [29]:

$$dH = \sum_i \frac{\partial H}{\partial q_i} dq_i + \sum_i \frac{\partial H}{\partial p_i} dp_i + \frac{\partial H}{\partial t} dt \qquad (24)$$

After substituting Equation 23 into Equation 24,

$$dH = \sum_i \dot{q}_i dp_i - \sum_i \frac{\partial L}{\partial q_i} dq_i - \frac{\partial L}{\partial t} dt \qquad (25)$$

and from Equation 22 it follows as,

$$dH = \sum_i \dot{q}_i dp_i - \sum_i \dot{p}_i dq_i - \frac{\partial L}{\partial t} dt \qquad (26)$$

After equating each term in Equation 26 to each term in Equation 24,

$$\dot{q}_i = \frac{\partial H}{\partial p_i}, \quad \dot{p}_i = -\frac{\partial H}{\partial q_i} \qquad (27)$$

Equations 27 are the canonical equations of Hamilton, which are 2n number of first-order differential equations.

2.7 Canonical Transformations

Hamiltonian formalism doesn't introduce an efficient calculation tool by itself. The freedom in choosing the physical quantities as coordinates and momenta is beneficial for solving difficult dynamical problems. Changing coordinates helps to reveal much about any dynamical system. In Hamiltonian mechanics, the Hamiltonian is constant if it doesn't ex-

plicitly depend on time, and the momenta are constant if the associated coordinates, which are called ignorable or cyclic coordinates, are missing in the Hamiltonian. However, it is necessary to start from the beginning when the change of coordinates is required. More-over, for Hamiltonian formalism, the coordinates can be changed to anything as long as they describe the system, but the momenta are dictated by the Lagrangian, see Equation 22. One method for changing coordinates without starting from the beginning by conserving the structure of Hamiltonian dynamics is canonical transformation [64].

Assume Equation 28 represents new canonical coordinates, and Equation 29 represents new momenta:

$$Q_i = Q_i(q_i, p_i, t) \tag{28}$$

$$P_i = P_i(q_i, p_i, t) \tag{29}$$

Also assume a new Hamiltonian $K = K(Q_i, P_i, t)$, and Hamilton's equations as:

$$\dot{Q}_i = \frac{\partial K}{\partial P_i}, \quad \dot{P}_i = -\frac{\partial K}{\partial Q_i} \tag{30}$$

The old variables q_i and p_i, and the new variables Q_i and P_i are supposed to describe the same dynamical system. The Hamilton's principle can be used to show that the variation of both integrals equal to zero as:

$$\delta \int (\sum_{i=1}^{N} p_i \dot{q}_i - H) dt = 0, \tag{31}$$

$$\delta \int (\sum_{i=1}^{N} P_i \dot{Q}_i - H) dt = 0, \tag{32}$$

where L can be deduced from Legendre transform as $L = (\sum_{i=1}^{N} p_i \dot{q}_i - H)$. Although the variations of both integrals equal to zero, the integrands aren't equal. The total time deriva-

tive of an arbitrary function F separates two integrands from each other as:

$$\delta \int [\sum p_i \dot{q}_i - H(p_i, q_i, t) - \sum P_i \dot{Q}_i$$
$$+ K(Q_i, P_i, t) - \frac{dF}{dt}]dt = 0$$

(33)

The variation vanishes at end times as:

$$\delta \int_{t_1}^{t_2} \frac{dF}{dt} dt = \delta(F(t_2) - F(t_1)) = 0,$$

(34)

where F is the generating function, which is a function of independent 2n variables. Table 6 shows the four possible forms of the generating function F. The generating function F needs to be known in order to apply the transformation. F can be obtained from the relationship between old and new coordinates, and Table 6, see Wiesel [64].

Table 6. Canonical Transform Relations

$F_1(q,Q,t)$	$F_2(q,P,t)$	$F_3(p,Q,t)$	$F_4(p,P,t)$
$p_i = \frac{\partial F_1}{\partial q_i}$	$p_i = \frac{\partial F_2}{\partial q_i}$	$q_i = -\frac{\partial F_3}{\partial p_i}$	$q_i = -\frac{\partial F_4}{\partial p_i}$
$P_i = -\frac{\partial F_1}{\partial Q_i}$	$Q_i = \frac{\partial F_2}{\partial P_i}$	$P_i = -\frac{\partial F_3}{\partial Q_i}$	$Q_i = \frac{\partial F_4}{\partial P_i}$

The new Hamiltonian K and the old Hamiltonian H are related by Equation 35 as:

$$K(Q,P,t) = H(q,p,t) + \frac{\partial F_1}{\partial t}$$

(35)

2.8   Hamilton-Jacobi Theory

The easier solution to a dynamical system can be accomplished when the more coordinates are missing in the Hamiltonian. Moreover, any momenta missing from the new Hamiltonian dictates that its conjugate coordinate is constant. If the new momenta, K,

equals to zero, all the new coordinates and momenta are constant [64]. Equation 36 shows that the new Hamiltonian equals to zero, which is called the Hamilton-Jacobi equation, and Equation 37 shows that the new coordinates and momenta are constant [29].

$$H(q_i, p_i, t) + \frac{\partial F}{\partial t} = 0 \tag{36}$$

$$\dot{Q}_i = \frac{\partial K}{\partial P_i} = 0$$
$$\dot{P}_i = -\frac{\partial K}{\partial Q_i} = 0 \tag{37}$$

It is favorable to use a generating function which is a function of the old coordinates, q_i, and the new momenta, P_i. The generating function, F_2, from Table 6 is such a function. Therefore, Equation 36 becomes [29]:

$$H\left(q_i, \frac{\partial F_2}{\partial q_i}, t\right) + \frac{\partial F_2}{\partial t} = 0 \tag{38}$$

Equation 38 is known to be Hamilton's principal function. The solution to this equation is denoted by S as [29]:

$$S = S(q_1 \cdots q_n, \alpha_1 \cdots \alpha_n, t), \tag{39}$$

where α_i are n number of constants of the integration because S is the solution to the first-order differential equation. Therefore, one of the variables of the solution has to be an arbitrary constant added to the solution S. Using the analogy of the physical description of the generating function, the constants of the integration, α_i, can be chosen as the new momenta, P_i [29]:

$$P_i = \alpha_i \tag{40}$$

29

After applying transformation for the F_2 generating function from Table 6 [29]:

$$p_i = \frac{\partial S(q_i, \alpha_i, t)}{\partial q_i} \qquad (41)$$

Continuing with the second half of the transformation [29]:

$$Q_i = \beta_i = \frac{\partial S(q_i, \alpha_i, t)}{\partial \alpha_i} \qquad (42)$$

Both α_i and β_i can be obtained by evaluating partial derivatives with the known initial conditions. The Hamilton-Jacobi equation can be solved as [29]:

$$q = q(\alpha_i, \beta_i, t) \qquad (43)$$

The Hamilton's principal function helps to transform the old variables to new constant coordinates and momenta. A solution to the dynamical system is obtained when solving the Hamilton-Jacobi equation. The relationship between the Hamilton's principal function and the Hamilton's principle can be shown by examining total time derivative of the Hamilton's principle function, S [29]:

$$\frac{dS}{dt} = \sum_i \frac{\partial S}{\partial q_i} \dot{q}_i + \frac{\partial S}{\partial t} \qquad (44)$$

After inserting Equation 36 and Equation 41, Equation 44 becomes:

$$\frac{dS}{dt} = \sum_i p_i \dot{q}_i - H = L \qquad (45)$$

Therefore, a constant differs the Hamiltonian principle function from Hamilton's principle as:

$$S = \int L \, dt + constant \qquad (46)$$

For Hamilton's principle, the solution to a dynamical system is obtained by solving the

30

definite integral of Lagrangian, L. Equation 46 represents the same integral in indefinite form which can be used to solve a dynamical system.

Hamilton's principle function can be separated in two parts when the Hamiltonian doesn't explicitly depend on time as [29]

$$S(q_i, \alpha_i, t) = W(q_i, \alpha_i) - \alpha_1 t, \tag{47}$$

where $W(q_i, \alpha_i)$ is the first part of the solution, which depends on the old coordinates and the new momenta, and appears only when the Hamiltonian is constant. $W(q_i, \alpha_i)$ is called Hamilton's characteristic function. Equation 47 is the solution to the Hamilton-Jacobi equation [29]:

$$\frac{\partial S}{\partial t} + H(q_i, \frac{\partial S}{\partial q_i}) = 0 \tag{48}$$

After substituting Equation 47, the Equation 48 becomes [29]:

$$H(q_i, \frac{\partial W}{\partial q_i}) = \alpha_1, \tag{49}$$

where one of the constants of integration, α_1, equals to the constant value of the Hamiltonian, H. The new Hamiltonian, K, equals to α_1 because H doesn't depend on time [29]:

$$K = \alpha_1 \tag{50}$$

After calculating Hamilton's equations for the new Hamiltonian, K [29]:

$$\dot{P}_i = -\frac{\partial K}{\partial Q_i} = 0, \quad P_i = \alpha_i$$
$$\dot{Q}_i = \quad \frac{\partial H}{\partial \alpha_i} = 1 \quad i = 1 \tag{51}$$
$$= 0 \quad i \neq 1$$

After denoting the generating function by $W(q_i, P_i)$, the solution becomes [29]:

$$
\begin{aligned}
Q_1 &= t + \beta_1 \equiv \frac{\partial W}{\partial \alpha_1} \\
Q_i &= \quad \beta_i \equiv \frac{\partial W}{\partial \alpha_i} \quad i \neq 1
\end{aligned}
\tag{52}
$$

where Q_1 is not a constant of the motion, and time , t, is a coordinate and the Hamiltonian is its conjugate momenta [29].

2.9 Action-Angle Variables

The periodic motion is of great importance in physics. The frequencies of the motion is mostly more desirable than the other properties of the orbit. A variation of the Hamilton-Jacobi process is used to obtain the frequency of the periodic motion. The action variables, J, are chosen instead of the new momenta of the Hamilton-Jacobi equations. J_i are independent functions of the α_i of the Section 2.8. Figure 7 shows an example of the two types of periodic motion. For oscillation, the system repeats its track for every point because q and p return to its original values after one period. For rotation, the position coordinate q is an unbounded angle of rotation, which grows indefinitely with a period of q_o, whereas q is bounded for oscillation [29].

J_i can be defined as [29]:

$$
J_i = \oint p_i dq_i
\tag{53}
$$

After applying the canonical transformation, Equation 53 becomes [29]:

$$
J_i = \oint \frac{\partial W(q_i, \alpha_i)}{\partial q_i} dq_i,
\tag{54}
$$

where the solution to the Equation 54 is J_i as independent functions of α_i. Substituting J_i
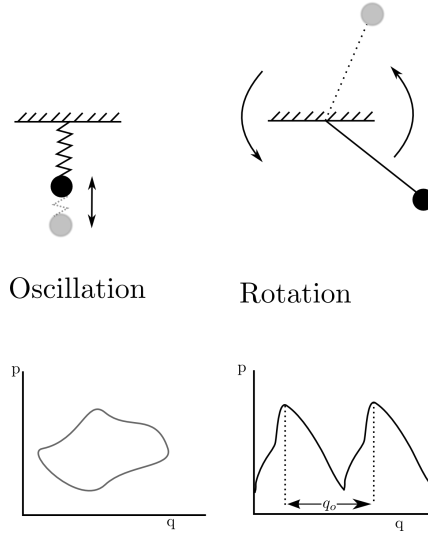
Figure 7. The Orbit of Phase Space for Periodic Motion [29]

for α_i yields the characteristic function W as [29]:

$$W = W(q_1 \cdots q_n; J_1 \cdots J_n) \tag{55}$$

Also, the angle variables, ω_i, are the conjugate coordinates to the J_i [29]:

$$
\begin{aligned}
p_i &= \frac{\partial W}{\partial q_i} \\
\omega_i &= \frac{\partial W}{\partial J_i}
\end{aligned}
\tag{56}
$$

The Hamiltonian is a function of only J_i because w_i are cyclic [29]:

$$H = H(J_1 \cdots J_n) = \alpha_1 \tag{57}$$

The Hamilton equations of motions for the new variables become [29]:

$$
\begin{aligned}
\dot{J_i} &= -\frac{\partial H}{\partial \omega_i} = 0 \\
\dot{\omega_i} &= \frac{\partial H}{\partial J_i} = v_i
\end{aligned}
\tag{58}
$$

33

where v_i are constant functions of J_i. The solution becomes [29]:

$$J_i = constant$$
$$\omega_i = v_i t + \beta_i$$

(59)

where the solution doesn't introduce any advantage over the α_i coordinates from the Section 2.8. The advantage of this process is that the Action-Angle variables transformation yields the frequencies, v_i, of the periodic motion without finding a complete solution. If a system is periodic, the energy of the system can be defined in terms of J_i by Equation 53. Next, the frequencies, v_i, of the system can be obtained by Equation 58. The ω_i are conveniently called angle variables due to Equation 59 [29].

The fact that the frequency v_i are related to q_i can be proved by investigating the change in one of the angle variables, ω_i, when one of the coordinates, q_i, completes its one cycle of oscillation or rotation. The Equation 60 shows that the change in the angle variable is caused by an incremental increase in one of the coordinates, q_j [29]:

$$\Delta \omega_i = \oint \delta \omega_i,$$

(60)

where $\delta \omega_i$ is the infinitesimal change due to the incremental increase in one of the coordinates, q_j [29]:

$$\delta \omega_i = \frac{\partial \omega_i}{\partial q_j} dq_j$$

(61)

Also, by Equation 56 and Equation 61, $\Delta \omega_i$ can be written as [29]:

$$\Delta \omega_i = \oint \frac{\partial \omega_i}{\partial q_j} dq_j = \oint \frac{\partial^2 W}{\partial q_j \partial J_i} dq_j$$

(62)

The J_i in the denominator can be taken out of the integral because J_i are independent func-

34

tions of only α_i [29]:

$$\Delta \omega_i = \frac{\partial}{\partial J_i} \oint \frac{\partial W}{\partial q_j} dq_j = \frac{\partial}{\partial J_i} \oint p_j dq_j \tag{63}$$

By Equation 53, $\Delta \omega_i$ becomes [29]:

$$\Delta \omega_i = \frac{\partial J_j}{\partial J_i} = 1 \qquad i = j$$
$$= \delta_{ij} \qquad i \neq j \tag{64}$$

If τ_i is the period of the motion related to q_i, Equation 65 becomes [29]:

$$\Delta \omega_i = 1 = \nu_i \tau_i$$
$$\nu_i = \frac{1}{\tau_i} \tag{65}$$

2.10   General Canonical Transformations

It is not an easy task to create a generating function for every canonical transformations. A different approach to canonical transformations can be initiated as [64]:

$$x^T = \{q_i, \ p_i\} \tag{66}$$

Next, the Hamilton's equations of motion becomes [64]:

$$\dot{q}_i = \frac{\partial H}{\partial p_i}$$
$$\dot{p}_i = -\frac{\partial H}{\partial q_i} \tag{67}$$

Equation 67 can be defined in terms of phase space state vector by Equation 66 [64]:

$$\dot{x} = Z\frac{\partial H}{\partial x}$$

$$Z = \left\{ \begin{array}{cc} 0 & I \\ -I & 0 \end{array} \right\} \tag{68}$$

where Z satisfies the properties [64]:

$$-Z = Z^T = Z^{-1} \tag{69}$$

Nothing new has been introduced except representing the Hamilton's equations in terms of the phase space state vector. The transformation of the phase space from the old variables, x, to the new variables, y, can be accomplished as [64]:

$$x = f(y) \tag{70}$$

Then, the new Hamiltonian, K, becomes [64]:

$$K(y) = H(f(y)), \tag{71}$$

where the old Hamiltonian, H, doesn't explicitly depend on time. The transformation, f, is valid as long as it is a canonical transformation. Therefore, the conditions which make f a canonical transformation should be examined. The new coordinates and momenta should comply with the Hamilton's equations as [64]:

$$\dot{y} = Z\frac{\partial K}{\partial y} \tag{72}$$

Converting Equation 72 to Equation 68 may reveal these conditions. Equation 73 shows

the time derivative of the transformation, and Equation 74 represents the gradient of the new Hamiltonian [64]:

$$\dot{x} = \frac{\partial f}{\partial y}\dot{y} \tag{73}$$

$$\frac{\partial K}{\partial y} = \frac{\partial}{\partial y}H(f(y)) = \left(\frac{\partial f}{\partial y}\right)^T \frac{\partial H}{\partial x} \tag{74}$$

Combining these equations with Equation 72 yields [64]:

$$\dot{y} = (\frac{\partial f}{\partial y})^{-1}\dot{x} = Z(\frac{\partial f}{\partial y})^T \frac{\partial H}{\partial x} \tag{75}$$

Then, Equation 75 yields $\dot{x}$ as [64]:

$$\dot{x} = (\frac{\partial f}{\partial y})Z(\frac{\partial f}{\partial y})^T \frac{\partial H}{\partial x} \tag{76}$$

Comparing Equation 68 to Equation 76 immediately yields [64]:

$$(\frac{\partial f}{\partial y})Z(\frac{\partial f}{\partial y})^T = Z, \tag{77}$$

where the first-order partial derivative is called the Jacobian matrix J. The J matrix is symplectic when it satisfies [64]:

$$JZJ^T = Z \tag{78}$$

Therefore, the transformation, f, is a canonical transformation if its Jacobian matrix is symplectic.

2.11 Orbit Perturbations for Near-Earth Satellites

Orbit perturbations are the deviations from the two-body orbit motion. Two-body motion assumes that secondary body orbits around a point of mass or spherically symmetric

sphere [15]. However, Earth is neither a point of mass nor spherically symmetric. The equatorial bulge, continental blocks, ocean basis, and mountain ranges result in gravitational field deviations from the two-body point of mass. Another important perturbation for near-Earth satellites is air drag. Air drag effect is bigger when a satellite has smaller mass with bigger cross section. Air drag acceleration is a non-conservative force, which determines the orbit lifetime of a satellite in Low Earth Orbit (LEO) [64]. Table 7 represents three categories for Earth orbits. LEO satellites are primarily affected by air drag and non-sphericity of Earth, and both MEO and GEO satellites are mainly perturbed by solar-radiation pressure and third-body effects [60]. This work includes air drag, and sectoral and tesseral harmonics perturbation accelerations. The effects of zonal harmonics perturbation are included in the periodic orbit, see Section 3.2.

Table 7. The Three Categories of Earth Orbits [60]

Orbit	Altitude (km)
Low Earth Orbit (LEO)	h < 800
Medium Earth Orbit (MEO)	800 ≤ h < 30,000
Geostationary Orbit (GEO)	h = 35,780

The gravitational field equation, which is also called Poisson's equation, is the fundamental partial differential equations for gravitational fields [64]:

$$\nabla^2 V = 4\pi G\rho, \tag{79}$$

where G is the gravitational constant, ρ is mass distribution, ∇^2 is Laplacian operator, and V is gravitational potential function. Equation 79 defines the gravitational potential of a sphere. The gravitational potential can be calculated by Equation 79 when mass distribution, ρ, is provided. However, the gravitational potential outside the sphere is needed. Equation 80 represents the infinite series of the gravitational potential function outside a
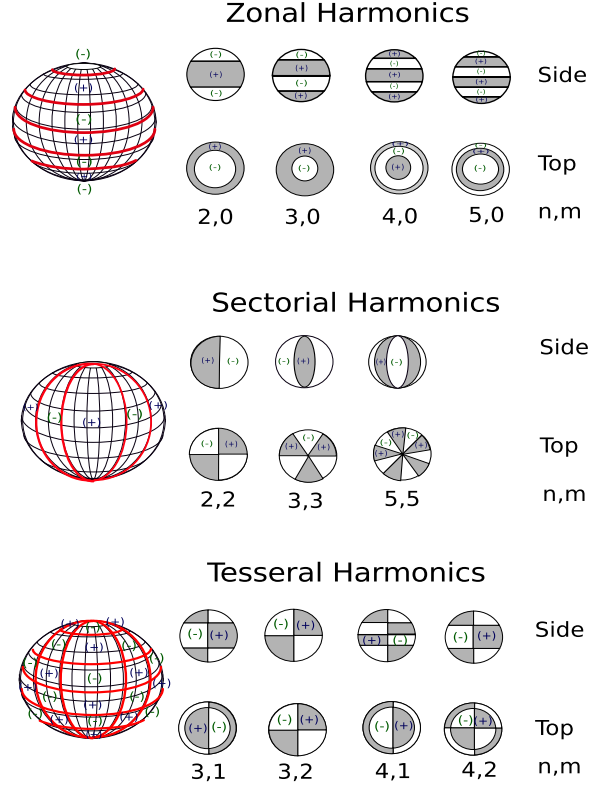
Figure 8. The Visual Depictions of Spherical Harmonics [60]

sphere, which has a radius of $R_{\oplus}$ [64].

$$V(r,\theta,\phi) = -\frac{\mu}{r} \sum_{n=0}^{\infty} \sum_{m=0}^{n} (\frac{r}{R_{\oplus}})^{-n} P_n^m(cos\theta)$$
$$\times (C_{nm}cosm\phi + S_{nm}sinm\phi) \tag{80}$$

where μ is the gravitational parameter, n and m are the order and degree of the expansion, respectively, $R_{\oplus}$ is the radius of Earth, P_n^m are the associated Legendre functions, the θ is the geocentric latitude, ϕ is the longitude, and C_{nm} and S_{nm} are gravitational constants, which can be obtained from the gravitation models. Both C_{nm} and S_{nm} define the shape of the gravitational field [64]. All spherical harmonics in the gravitational potential field of Earth, which are zonal, tesseral, and sectoral harmonics, can be represented by Equation 80 [60]. Figure 8 shows the visual depictions of three types of spherical harmonics.

Newtonian point of mass potential can be obtained from Equation 80 when $m,n = 0$.

The first term is free of longitude and latitude terms because $cos\ m\phi = 0$, $sin\ m\phi = 0$, $C_{00} = 1$, and the associate Legendre function $P_0^0 = 1$.

$$V = -\frac{\mu}{r}, \tag{81}$$

where V is the Newtonian point of mass potential.

The geopotential expansion yields zonal harmonics when n is the order and $m = 0$ is the degree. The smallest zonal harmonic, which has $n = 1$ order and $m = 0$ degree, is considered to be zero because it shifts the center of mass of Earth parallel to North-South axis. Any frame which doesn't have its origin at the center of mass is not practical. Therefore, the first zonal harmonic equals to zero, $J_1 = 0$, when the origin is defined at the center of Earth. The second zonal harmonic specifies the oblateness of Earth at the equator. For the Earth's potential expansion, the J_2 is second to the Newtonian point mass potential in strength. The Newtonian potential is 10^3 times bigger than the the $J2$. The contribution of J_2 term to the gravitational potential can be represented as [64]:

$$V_{20} = \frac{\mu R_\oplus^2 J_2}{2r^3}(3cos^2\theta - 1), \tag{82}$$

where $J_2 = -C_{20} = 0.001082$. For the second zonal harmonic, J_2, mass concentration is bigger at the equator than the poles. The higher order zonal harmonics add more terms to the potential, which model the irregularities of the mass distribution along the longitudes. See Figure 8 for the visual depiction of zonal harmonics [64].

The sectoral harmonics are the terms with equal orders and degrees in the potential expansion, $n = m$. They are functions of only longitude, and they change signs across the longitudes. The first sectoral harmonic, $n = m = 1$, changes the location of center of mass away from the origin of a reference frame to another one in the equatorial plane. Therefore, $S_{11} = C_{11} = 0$ because it is always desirable to have center of mass at the origin

of a reference frame. The second sectoral harmonic, $n = m = 2$, contributes to the potential as [64]:

$$V_{22} \propto C_{22} cos\, 2\phi + S_{22} sin\, 2\phi, \tag{83}$$

where ϕ is the longitude. The second sectoral harmonics, C_{22} and S_{22}, are on the order of 10^{-6}. J_2 is 10^3 times bigger than C_{22} and S_{22}. The mass concentrations of Earth at Eurasia and the Americas are bigger than Pacific and Atlantic ocean basis due to the second sectoral harmonics. See Figure 8 for the visual depiction of sectoral harmonics [64].

The tesseral harmonics are the case when $n \neq m \neq 0$ in the geopotential expansion. They create a sphere with rectangular square-tiled boards on it. The number of bands in latitude is $n - m + 1$ because of $P_n^m(cos\, \theta)$ dependence. The terms , $C_{nm} cos\, m\phi$ and $S_{nm} sin\, m\phi$, disappear for $2m$ meridians. Therefore, there are $2m$ bands in longitude. See Figure 8 for the visual depiction of tesseral harmonics [64, 60].

The gravity models, such as EGM96, include the coefficients, C_{nm} and S_{nm}. The gravity models are built from terrestrial or satellite measurements. The satellite measurements are orbit dependent. Therefore, the accuracy of a gravity model depends on the number of satellites with different orbits. This effort uses the EGM96 gravity model. The EGM96 is developed by the University of Texas at Austin, the Defence Mapping Agency, Ohio State University, and the Goddard Spaceflight Center. The EGM96 includes 30 different satellite measurements and terrestrial gravity measurements. It is a complete model with degree and order 360 [60]. However, this work uses only order and degree 20 because it provides high accuracy with low computational power requirement. Figure 9 represents the variations in the geopotential.

The air drag is the other perturbation included by this work. The air molecules behave individually, which is called the free molecular flow regime, at the altitude of satellites. The air molecules impact the motion of the satellites. Equation 84 represents the drag law

41
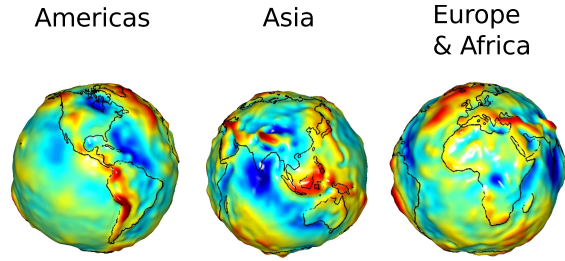
Figure 9. GRACE Gravity Model [53]
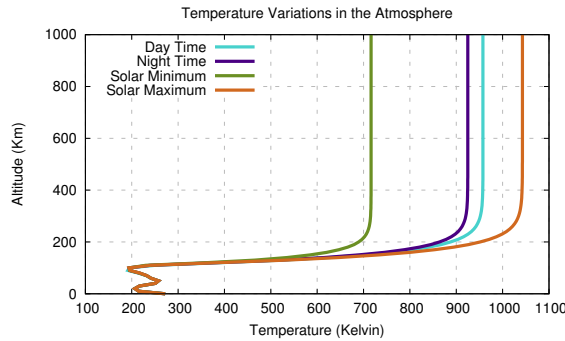
Figure 10. Temperature Variations in the Atmosphere

[64]:

$$a_d = -\frac{1}{2}\frac{C_D A}{m}\rho V \mathbf{V}, \tag{84}$$

where C_d is the drag coefficient, which is 2.2 for flat plane models, and between 2.0 and 2.1 for spheres for the most part, ρ is the atmospheric density, A is the cross-sectional area of the satellite, V is the velocity of the satellite relative to the air molecules, and m is the mass of the satellite. The drag coefficient, C_d, specifies the vulnerability of a satellite to the air drag, and it is dimensionless. The atmospheric density at the altitude of a satellite is represented by ρ, which is difficult to calculate due to the interaction between Earth's upper atmosphere and Sun. The cross-sectional area, A, is also difficult to calculate because the attitude of the satellite must be known. Moreover, it is almost impossible to determine the attitude of a tumbling satellite [60].

Solar flux and geomagnetic storms heat up the thermosphere. Therefore, the upper at-

mosphere expands, which increases the number of air molecules. During Solar maximum the emission of Extreme Ultraviolet radiation (EUV) increases because Solar flare and Coronal Mass Ejection (CME) events increase during Solar maximum. Charged particles coming from the night side of the Earth's atmosphere during geomagnetic storm interact with air molecules, and increase their energy, which expands the upper atmosphere. Geomagnetic storms cause delayed expansion in the atmosphere because storms first hit the day side of the Earth's atmosphere. Both Solar flux and geomagnetic storms increase the atmospheric density in the upper atmosphere. Figure 10, which is plotted using Mass Spectrometer - Incoherent Scatter (MSIS-E-90) model data, shows the temperature change in the atmosphere due to the diurnal variations and the Solar cycle, and Figure 11, which is plotted using SGP4 and TLE prediction data, represents the impact of air drag on the Delta 1 rocket body over 138 days, which has an altitude of 482 km.
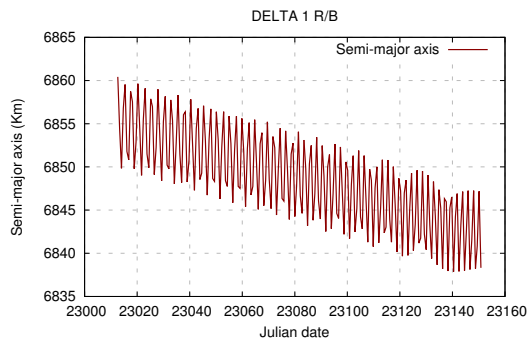
Figure 11. Air Drag Effect on the Delta 1 Rocket Body

Although the atmospheric density is unpredictable, it is very important for the accuracy of the orbit predictions. Many atmospheric models, which are either static or time-varying, has been developed. Every model is either based on physical models, which are built by combining conservation laws and atmospheric-constituent models or developed from in-situ measurements and satellite-tracking data. Every atmospheric model is different in terms of speed, accuracy, and applicability. Therefore, there is no model which provides

43

best results for all applications. This effort uses the 1962 Standard Atmosphere. The routine for the atmosphere model requires the altitude of each layer, molecular weight, and molecular temperature. Moreover, the temperature within each layer changes linearly, see Regan and Anandarskarian [27]. It is an ideal, static atmospheric model at a latitude of $45°$ during moderate Solar activity [60].

2.12 Numerical Integration Methods

There are many numerical integration methods which have been developed to solve ordinary differential equations. Most of these methods have been successfully applied in celestial mechanics. However, there is no numerical integration method which yields the best solution to every problem pertaining to the motion of satellites. The most important numerical integration methods for orbit computations are Runge-Kutta methods, multistep methods, and extrapolation methods. Runge-Kutta methods are easy and applicable to wide range of different problems. Multistep methods are very efficient, but they need to store previous data points. Extrapolation methods are highly accurate [56].

This effort uses 4th-order Hamming predictor-corrector method, which is basically a multistep numerical integrator. It requires four values of the state vector. However, only the initial conditions are know at the beginning. The other three values can be obtained by a process called Picard iteration. Equation 85 shows the Picard iterative process:

$$y_{n+1}(x) = y_n + \int_{x_o}^{x} f(t, y_n(t)) dt$$
$$y_n(x) = y_n$$

(85)

If the Picard iteration converges, the four values of the state vector are extrapolated to give the next value for the state vector, which is the predictor part. Next, the extrapolated state is corrected using better values of the equations of motion, which is the corrector part. Although predictor-corrector methods require complex algorithms, they are favorable

because of their stability.

2.13   KAM theory

The French mathematician and physicist Henri Poincaré found out that 3BP is unsolvable because of small divisors problem. He suggested that N-Body Problem is mathematically unsolvable. Birkhoff and Smale proved Poincaré's earlier findings, and they suggested that some nonlinear systems aren't solvable. The primary question was: When does a system behave chaotically? The KAM theory, which was announced by A.N. Kolmogorov in 1954, and proved by J. Moser and V.I. Arnol'd in the early 1960's, is the solution to this question from the Hamiltonian aspect. The KAM theory explains what happens when an integrable Hamiltonian is perturbed. It is developed to overcome the difficulties in perturbation theory about small divisors [50]. The KAM theory states that an integrable, which means n constants of the motion are known, Hamiltonian has a phase space motion which lies on a n-dimensional torus in $2n$-dimensional phase space, where n is the number of independent coordinates [47, 6]. The quasi-periodic motion can be represented by action and angle variables, see Section 2.9. The quasi-periodic orbits describe integrable motion on the invariant torus. If any trajectory is on an invariant torus in phase space, it will stay on the torus [5]. The quasi-periodic motions have n number of frequencies, which is dictated by the Hamilton-Jacobi theory [65].

The fundamental equation for the KAM theory can be shown as :

$$H(\mathbf{I}, \theta) = H_o(\mathbf{I}) + \varepsilon H_1(\mathbf{I}, \theta), \tag{86}$$

where H is the perturbed Hamiltonian, H_1 is the perturbing Hamiltonian, H_o is the integrable Hamiltonian, ε is a small real number, $\varepsilon << 1$, and $\mathbf{I}$ *and* θ are action-angle variables. H_o *and* H_1 must be real analytic functions, which are infinitely differentiable

45
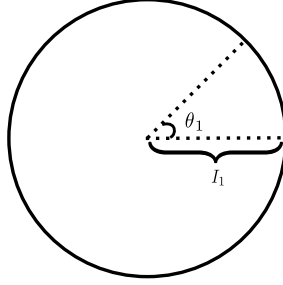
Figure 12. A Visual Depiction of 1-Torus [50]

functions. The action variable I is constant and θ is a linear function of time because H_o is only a function of $\mathbf{I}$, see Equation 27. Figure 12 represents 1-torus, and Figure 13 shows 2-torus where the action variables, $\mathbf{I}$, are constant and the angle variables, θ, are functions of time.

If the solutions for the perturbed Hamiltonian Equation 86 lie on n-dimensional tori, there are new action-angle variables as [57]:

$$H(\mathbf{I}, \theta) = H'(\mathbf{I}') \tag{87}$$

Equation 87 represents the generating function, S, for the Hamilton-Jacobi transformation, see Section 2.8 [57]:

$$\mathbf{I} = \frac{\partial S(\mathbf{I}')}{\partial \theta}$$
$$\theta' = \frac{\partial S(\mathbf{I}')}{\partial \mathbf{I}'} \tag{88}$$

New Hamiltonian is a function of only $\mathbf{I}'$ because the θ variables are cyclic, and the Hamilton-Jacobi equation becomes [57]:

$$H(\frac{\partial S}{\partial \theta}, \theta) = H'(\mathbf{I}') \tag{89}$$

46
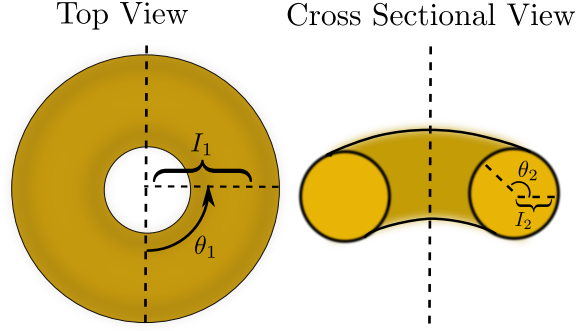
Figure 13. A Visual Depiction of 2-Torus

Power series expansion in ε can yield a solution to the generating function, S, as [57]:

$$S = S_o + \varepsilon S_1 + \varepsilon^2 S_2 + \cdots \tag{90}$$

Substituting Equation 89 in Equation 88 assuming $S_o = \mathbf{I}' \cdot \boldsymbol{\theta}$ because Equation 87 yields $\mathbf{I} = \mathbf{I}'$ and $\boldsymbol{\theta} = \boldsymbol{\theta}'$ after the assumption [57]:

$$\begin{aligned}
H_o(\mathbf{I}' + \varepsilon \frac{\partial S_1}{\partial \boldsymbol{\theta}} + \varepsilon^2 \frac{\partial S_2}{\partial \boldsymbol{\theta}} + \cdots) \\
+ \varepsilon H_1(\mathbf{I}' + \varepsilon \frac{\partial S_1}{\partial \boldsymbol{\theta}} + \cdots, \boldsymbol{\theta}) = H'(\mathbf{I}')
\end{aligned} \tag{91}$$

The expansion of Equation 91 for small ε keeping only the first-order terms yields [57]:

$$H_o(\mathbf{I}') + \varepsilon \frac{\partial H_o}{\partial \mathbf{I}'} \cdot \frac{\partial S_1}{\partial \boldsymbol{\theta}} + \varepsilon H_1(\mathbf{I}', \boldsymbol{\theta}) = H'(\mathbf{I}') \tag{92}$$

Then, $H_1(\mathbf{I}', \boldsymbol{\theta})$ and $S_1(\mathbf{I}', \boldsymbol{\theta})$ can be represented as Fourier series [57]:

$$\begin{aligned}
H_1 = \sum_{\mathbf{m}} H_{1,\mathbf{m}}(\mathbf{I}') exp(i\mathbf{m} \cdot \boldsymbol{\theta}) \\
S_1 = \sum_{\mathbf{m}} S_{1,\mathbf{m}}(\mathbf{I}') exp(i\mathbf{m} \cdot \boldsymbol{\theta})
\end{aligned} \tag{93}$$

where $\mathbf{m}$ is a vector with n rows consisting of integers. Substituting Equation 93 in Equa-
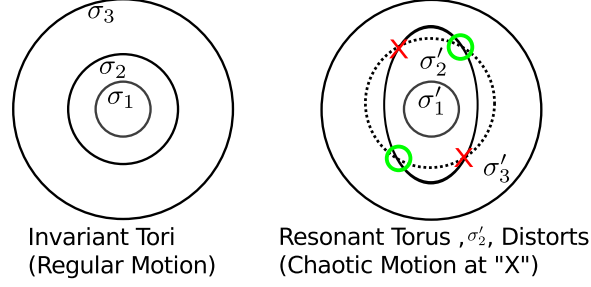
Figure 14. Elliptic Islands and Hyperbolic Fixed Points

tion 92 yields [57]:

$$S_1 = i \sum_{\mathbf{m}} \frac{H_{1,\mathbf{m}}(\mathbf{I}')}{\mathbf{m} \cdot \nu_o(\mathbf{I}')} exp(i\mathbf{m} \cdot \boldsymbol{\theta}) \tag{94}$$

where ν_o is the unperturbed n-dimensional frequency vector by Equation 59. The infinite sum must converge to provide a solution. Moreover, the same condition must be satisfied for S_2, S_3, $\cdots$ if ε is expanded to higher orders. Although a method of successive approximations to S has been shown here, the proof of KAM theory depends on complex successive approximations which converge much faster.

The convergence of the sum depends on the denominator, $\mathbf{m} \cdot \nu_o(\mathbf{I}')$. This problem is called the small divisors problem. The action variables, $\mathbf{I}$, specify the resonant tori, which behave chaotically when $\varepsilon > 0$, for the unperturbed system when $\mathbf{m} \cdot \nu_o(\mathbf{I}') = 0$. On the other hand, the nonresonant tori must satisfy the Equation 94 [57]:

$$|\mathbf{m} \cdot \nu| > K(\nu)|\mathbf{m}|^{-(n+1)}, \tag{95}$$

where $\mathbf{m}$ are vectors consisting of integers, the absolute value of $\mathbf{m}$, $|\mathbf{m}|$, is the sum of all $\mathbf{m}$ vectors up to number n, and $K(\nu) > 0$ is an arbitrary number independent of $\mathbf{m}$. Moreover, $\mathbf{m}$ can't be the zero vector for nonresonant tori [57]. Therefore, it is highly likely that a perturbed, nearly integrable, and periodic system is described by an invariant tori in phase space [1].

Another way to describe the resonant tori, which helps to visualize it, is by winding

number, σ. Figure 13 can help to visualize of the ratio of two frequencies, v_1 *and* v_2. Assume v_1 is the frequency seen from top view, and v_2 is the frequency seen from cross sectional view. If the winding number, $\sigma = v_1/v_2$, is a rational number, the tori associated with this winding number are called resonant tori. The tori with irrational winding number, σ, are called nonresonant tori. For nonresonant tori, "almost all" orbits are preserved because "the KAM theory restore a measure of continuity to chaos" [50]. Figure 14, which consists of two surface of section plots, represents what happens if a resonant torus breaks up when a perturbation is introduced to the system. According to the Birkhoff's theorem, alternating elliptic and hyperbolic fixed points are formed when the resonant torus breaks down. The two stable elliptic islands, which is represented by O, and the two unstable hyperbolic points, which is represented by X, are shown in Figure 14.

2.14 KAM Theory Applications

After KAM theory was published, astronomers applied it to astronomical models because the motions in the solar system are comparatively bounded. However, application of KAM theory to astronomical models didn't yield promising results because of the limitation on the size of the perturbation parameter, ε, which is the ratio of masses. In 1963, Arnold endeavored to establish the existence of KAM tori for NBP, which he was partially successful. The primary question was whether there were the initial position and velocities of the bodies that keep the distance of the bodies from each other bounded for all the time in the NBP [2]. A combination of KAM theory and computer-assisted techniques named interval arithmetic, which is a computational technique that controls the errors introduced by numerical computations in a special way, was successfully used to prove the existence of KAM tori for the Restricted, Planar, Circular 3-Body Problem (RPC3BP) by Celletti and others. In 1997, Celletti and Chierchia proved the existence of quasi-periodic tori with a frequency close to the average frequency of Ceres for the Sun-Jupiter-Ceres problem [12].

Locatelli and Giorgilli proved the existence of KAM tori describing the secular motions of Jupiter and Saturn for the obserbed values of the parameters [48]. Celletti and Chierchia investigated a truncated RPC3BP model for Sun, Jupiter, and Asteroid 12 Victoria. The invariant tori bounding the motion of Victoria was built successfully for the astronomic value of the Jupiter-Sun mass ratio [13]. For further information, see a brief history of KAM tori for NBP [14].

The numerical applications of KAM theory originated from Binney and Spergel's paper which spectra obtained from Fourier series of the coordinates of numerically integrated orbits under the influence of galactic potentials can be expressed as sums of integer multiple of fundamental frequencies. Binney and others realized that orbits of N-dimensional galaxies defined in phase space can be represented as N-tori [4, 6]. McGill and Binney developed a method to build tori for Hamiltonians including general gravitational potentials. This method is based on the idea of distorting the analytic tori of a toy Hamiltonian into the desired tori using generating functions [18, 6]. Binney and Kumar generalized the method for obtaining the frequencies and angular variables related to the tori least-squares fitted to any Hamiltonian [3, 6]. Kaasalainen and Binney further refined the torus-fitting process of the method in order to include the case of non-rotating bar, which admits two major orbit families instead of one [36, 6]. Kaasalainen and Binney introduced point transformations into the method in order to solve the problem of a toy potential being too different from its target potential [35, 6]. Then, Kaasalainen showed that the method can be applied to globally chaotic regions as well [34, 6].

The only work related to this effort in terms of the application of KAM theory for objects orbiting Earth has been done by Wiesel and his masters and PhD students. Their efforts are represented in a chronological order. Wiesel showed that Earth satellite orbits under the full geopotential effect are likely to be KAM tori in a reference frame rotating with Earth. First, he determined the frequencies of the orbit using a Laskar frequency

algorithm. Next, he obtained Fourier series coefficients from numerically integrated trajectories. Then, He fitted numerically integrated orbit to the multiple Fourier series, which defines the torus, using least squares fitting technique. The spectral analysis of almost all orbits, excluding chaotic ones, yielded three basis frequencies. Moreover, Wiesel concluded that other dynamical effects can be added as perturbations because of the single point construction of the Hamilton-Jacobi separation of variables solution [65]. His next paper related to the application of KAM torus theory to Earth satellites is the one that compares two different KAM torus construction algorithms, which are the least squares fitting of a KAM torus to a numerically integrated orbit and the extraction of the Fourier coefficients of the KAM torus from numerically integrated Fourier transform. An efficient KAM torus construction method, which yields the torus that passes through the given initial conditions, is important for applications, such as formation flight of satellites, stationkeeping satellite constellations, and compressing ephemeris data for navigational satellites [66]. Derbis tried to apply the KAM theory to precise satellite data from the GPS satellites. She applied a Fast Fourier Transform (FFT) to obtain and identify discrete frequencies from orbit data. However, some orbits showed inconsistencies related to their basis frequencies. She concluded that the inconsistencies in the third frequency, ω_3, which is the apsidal regression rate, caused by the resonance in orbits of the GPS satellites [22]. Little tried to build KAM tori from orbit data of the Gravity Recovery Climate Experiment (GRACE) and Jason-1 satellites. He applied a modified Laskar Fourier transform algorithm to obtain the basis frequencies of the orbits. Although the residuals of the KAM torus for Jason-1 satellite were as low as 1 km over a 30 day period, the KAM torus construction process failed for GRACE satellite. Little concluded that air drag and errors related to Fourier coefficients resulted in the poor results for GRACE satellite. Craft investigated the applicability of the KAM theory for the satellite formation flight in the full geopotential with an order and degree of 20. The KAM torus method yielded promising results for the satellite

51

formation flight applications. Orbits of satellite clusters provided with drift rates in the nanometer to micrometer range over 60 day integration interval when they were separated by 10 to 100 meters [20]. Bordner tried to apply the KAM theory to the GPS satellite orbits. His research questions were whether the KAM theory can increase the accuracy of GPS satellites and whether it can reduce the burden on GPS operations. However, the methods for constructing KAM tori failed to yield desired accuracy for operational GPS orbits. He suggested that improved methods are needed to deal with complexities related to the maneuvering operational satellites [6]. Wiesel's third paper related to the KAM theory compared the KAM tori built from 2BP, SGP4 model, and numerically integrated orbit with a degree and order of 20. He showed that a KAM torus is similar to a full analytic perturbation theory in many ways. However, for a KAM torus, frequencies aren't approximations of the perturbation series expansions, and the torus is built numerically. Moreover, the comparison of numerical integration and the KAM torus, which yielded residuals smaller than 4 m over 10 years, showed that trajectories in the full geopotential are KAM tori [68]. Yates investigated the motion near a reference torus in order to compensate for errors in the reference KAM torus due to dissipative forces, such as air drag, lunar/solar mass effects. He suggested that routine phase angle updates and stochastic offsets to the reference torus can improve the accuracy of the KAM torus perturbed by dissipative forces. He showed that most stochastic effects can be modeled to predict the motion near a reference torus. Moreover, the low eccentricity of International Space Station (ISS) is proved to be a big hurdle in estimating the torus coordinate offsets [70]. Hagen studied the effects of air drag and lunar mass perturbations on a reference KAM torus. He showed that the KAM theory is also applicable when air drag and lunar mass perturbations are included in the system. However, it is proved that an accurate Jacobian, which performs the linear transformation, is of great importance, and Jacobian is only valid when the reference torus coordinates are tightly aligned with the perturbed torus coordinates [30]. This effort includes air drag

as perturbations to the reference KAM torus. Frey studied feasibility of constructing the KAM torus using TLE and SGP4. Frey's work, in a sense, proved that the KAM torus can be constructed from observational data. Two of his test cases, which are the two Delta rocket bodies, failed due to air drag and inaccuracies of the TLE data. The other two test cases, which are the Hubble Space Telescope (HST) and the Thor rocket body, showed that it is possible to extract accurate KAM torus basis frequencies although they suffered from their small eccentricities. Frey concluded that small eccentricities can't be modeled with a modified Laskar frequency algorithm developed by Wiesel [28]. This effort uses a different method which builds the reference KAM torus for orbits with low eccentricities using periodic orbits and Floquet theory.

This effort is based on Wiesel's recent paper, "A Theory of Low Eccentricity Earth Satellite Motion", and it builds on the results of previous efforts related to the application of KAM theory to Earth orbiting satellites. Wiesel considered the Earth satellite motion in terms of periodic orbits and Floquet theory. Periodic orbits in the zonal potential are known to be nearly circular, excluding the ones with critical inclination [58]. The main advantage of applying this method is that perturbations are in the order of 10^{-5} instead of 10^{-3} because periodic orbits includes the effects of the Earth's oblateness. The perturbations caused by sectoral and tesseral potential terms, air drag, and third body mass effects can be added to the periodic orbit. The current method is a hybrid of numerical and analytic methods. It has numerical sets of algorithms that may match numerical integration in their accuracy. Moreover, Once the theory files are constructed, which takes approximately 1 minute per orbit, it has the the usual advantages of general perturbations because it provides the results at the time of interest without having to perform a long propagation [69].

2.15 Summary

Space surveillance systems are under great stress due to the number of objects orbiting the Earth. Current launch rates and operational lifetimes of current satellites show that space surveillance systems need to cope with more objects soon. The increase in the spatial density of debris leads to an increase in the probability of collision. Figure 15 represents the growth of the cataloged satellite population during the past 15 years. Therefore, a new method which is as accurate as numerical methods and as fast as analytical methods is needed. The KAM theory for Earth orbiting objects yield promising results specifically for space debris because they are non-maneuverable,and lightly perturbed. Once a KAM torus is built for a non-maneuverable object, its motion will be bounded by the torus until a dissipative force affects its motion. Formation flight of satellites is another potential application of the KAM tori. Craft showed that tight formations yield secular drift rates between satellites from 4 nanometers to 1 micrometer per second [20]. Moreover, The KAM tori can reduce the operational burdens of GPS because the ephemerides provided by the orbital tori will have a much longer useful life [6]. Indeed, the KAM tori has numerous potential applications because they provide accurate predictions with long lasting validity for the time of interest as fast as an analytic method can provide. However, computationally expensive long integrations for building a torus, and perturbations that shift a reference torus to the nearby torus have been the main problems for the theory. Hopefully, this effort mostly overcomes these issues and the KAM torus orbit determination will serve as a prelude to converting the TLE catalog.
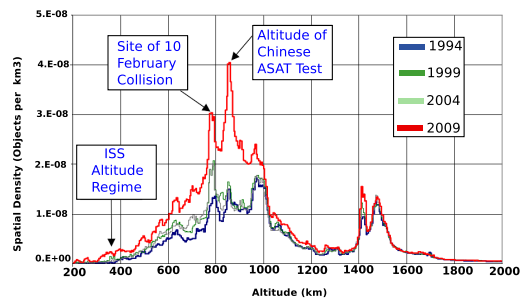
Figure 15. The Growth of the Cataloged Satellite Population over 15 Years [55]

III. Methodology

This chapter describes the data, the method, and the analytic process used to perform this study. This effort is intended for small eccentric orbits, which were one of the main issues for the KAM torus construction process for the previous efforts. Although this effort has been built on the previous works, it introduces a completely new method for constructing the KAM torus, which was developed and coded by Wiesel. In addition, the new theory is a complete orbit determination method which retrieves the TLE data for two months from `www.space-track.com` servers, propagates each TLE for one orbit, build the KAM torus theory file using some of the SGP4 mean elements, and fits the low eccentricity KAM torus to the SGP4 and TLE predictions using least squares without human intervention. Although converting whole TLE catalog to the new method is a trivial task, it requires at least 30 days of computation time. Therefore, the author pseudo-randomly chose 1500 objects from the NORAD satellite catalog for analysis. This chapter can simply be divided into four distinct parts. The first part, Section 3.1, discusses the data gathering, SGP4 propagation, and contains a quick overview of the whole process. The second part includes all sections from Section 3.2 to Section 3.6, which can be conveniently named as the KAM theory building part. The third part, starting in Section 3.7, introduces the evolutionary steps to the desired KAM torus by differential correcting the initial conditions and the frequencies of the newly built torus using SGP4 and TLE data. The fourth part is a summary.

3.1 Data Gathering and Overview of the Method

This effort uses the TLE obtained from the website `www.space-track.org`. This site allows users to download the TLE of most satellites. The previous work by Wiesel and others showed that there are some properties of satellites which cause difficulties in KAM tori construction process. The author also made an initial test in order to define an optimal ec-

56

centricity threshold level because this effort is intended for low eccentric orbits. Although the author defined an eccentricity of 10^{-3} and small as optimal eccentricity for the program to converge, he will further analyze the highest limit for the eccentricity to converge by modifying the code. It is also known that there are no nearly circular periodic orbits in the close vicinity of the critical inclination, which is 63.435°, or the complementary angle of 116.565° [58]. Although there exist periodic orbits for polar orbits, the close vicinity of polar orbits is avoided because of numerically unstable Legendre polynomial recursions for the gravitational potential calculations. The correction is left for future studies. An altitude of 300 km and more is chosen as a criterion because air drag shrinks the size of the torus down in phase space. It is also known that orbital maneuvers destroy the KAM torus, but they are not listed as a criterion because maneuvers are unpredictable. Table 8 shows known issues in the previous works and the selection criteria of test objects for avoiding these issues.

Table 8. Test Case Selection Criteria

Issues	Test Case Selection Criteria
Air Drag	Objects which have altitude of 300 kilometers and more
Resonance	Objects with periods that are not nearly an integer multiple of Earth's rotational period
Critical inclination and Polar Orbits	Objects which have inclinations that aren't in the close vicinity of the critical and polar inclinations. ($0° \leq i \leq 60°$ and $67° \leq i \leq 87°$ and $93° \leq i \leq 113°$ and $119° \leq i < 180°$)

There are 7,938 space objects which match the criteria in Table 8. The author wrote a C++ script which retrieves 7,938 TLEs for a period of 2 months ,which is between Jan 1, 2013 and March 1, 2013, from `www.space-track.org` server. This script also prepares essential input files that are required by low eccentricity KAM torus construction program,
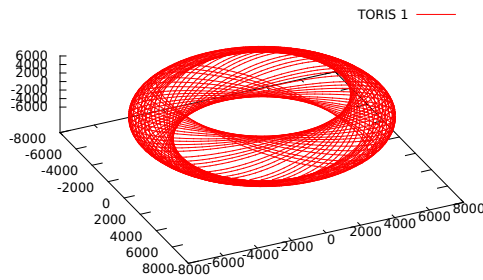
Figure 16. The Orbit of Toris 1 Satellite over 2 Months

which can be conveniently named as theory building program. The solar activity is relatively low between the selected dates. The dates for solar minimum can be selected, but the author intended to analyse the recently launched satellites as well. Then, 1500 TLEs are pseudo-randomly selected, and propagated for an orbit for a period of 2 months by Vallado's revised SGP4 code [21]. Figure 16 shows the orbit of TORIS 1 satellite over two months, which is simply a torus shape. TLEs are propagated for an orbit period because it is known that the position errors are smallest some point within the data interval and grows with respect to time going outwards into the future, or back into the past [67]. It is also desirable that JSpOC releases the TLE with an epoch time within data interval. JSpOC fits the orbits for 3 to 4 days for LEO satellites and a couple of weeks for higher altitude satellites. Therefore, there is a progression of orbits, and that progression includes more information than each individual orbit has. The idea behind propagating each TLE for a 2 months orbit is to obtain more accuracy through combining smaller chunks of less accurate propagation data. Because SGP4 and TLE prediction data are considered observational data, data from the calculation of dynamics are needed, which will be combined to form an estimate. The low eccentricity KAM torus provides the dynamical data. The low eccentricity KAM torus construction starts with the calculation of the periodic orbit, which is basically a boundary value problem. Once the periodic orbit is built, it is transformed to Fourier series [23]. The solution for the periodic orbit in the zonal potential problem

58

yields two basis frequencies, which are the Keplerian frequency and the nodal regression rate. The other missing frequency, which is the advance of the argument of perigee rate, can be obtained from the Floquet solution of the periodic orbit. The Floquet solution also yields two time linear terms due to adjacent periodic orbits. The solution includes only the zonal potential so far. However, perturbations, which are air drag, and sectoral and tesseral harmonics perturbations, are added to the Floquet solution. Therefore, the problem becomes forced linear system problem. The order of perturbations suddenly drops from 10^{-3} to 10^{-6}, which satisfies the main dictate of KAM theorem of small perturbations better. In addition, the momenta are inertial velocity components defined in a rotating frame of reference because of the set up of the dynamics. Therefore, simply substituting velocity components with momenta is a valid approach, see Section 3.2. Indeed, defining the forcing function as a function of Q_1 and Q_2 in a reference frame that rotates with Earth where sectoral and tesseral perturbations are stationary leads to the usual set up of the fundamental equation for the KAM theorem, see Equation 86. After the low eccentricity KAM torus is built, it is fitted to the observational data acquired from SGP4 and TLE prediction. Non-linear least square algorithm is used to form an estimate. The modal variables and the frequencies of the periodic orbit are updated for each iteration, see Section 3.7. Although, the author represents the process piece by piece, each main program is connected to another by GNU/Linux bash files, which are batch files for MS-DOS environment. Therefore, it is a simple matter to switch different parameters, such as air drag, and sectoral and tesseral perturbations, on and off. Moreover, human intervention is not required during the process due to the bash files which orchestrate the whole orbit determination procedure. This method is a numerically constructed perturbation theory which uses periodic orbits under the influence of only the zonal potential as the starting point [69].

3.2 Satellite Dynamics

This effort uses different reference frames, such as rotating and inertial frames of reference. The inertial reference frame is the ECI frame, and the rotating frames have rotation rates, $\omega = \dot{\Omega}$ where the frame of reference is tied to the regression of the ascending node, or $\omega = \omega_\oplus$ where it is tied to Greenwich. In such a rotating frame of reference the inertial velocity vector becomes [69]:

$$v = \dot{r} = \left\{ \begin{array}{c} \dot{x} - \omega y \\ \dot{y} + \omega x \\ \dot{z} \end{array} \right\}, \tag{96}$$

where ω appears in the components of the inertial velocity because of transport theorem. Then the satellite's kinetic energy becomes [69]:

$$T = \frac{1}{2} \left((\dot{x} - \omega y)^2 + (\dot{y} + \omega x)^2 + (\dot{z})^2 \right) \tag{97}$$

The generalized momenta can be found from the canonical Hamilton equations, $p_i = \partial T / \partial \dot{q}_i$, as [69]:

$$p_x = \dot{x} - \omega y$$
$$p_y = \dot{y} + \omega x \tag{98}$$
$$p_z = \dot{z}$$

where the generalized momenta are the inertial velocity components. Then, the Hamiltonian can be calculated from $H = \sum_i p_i \dot{q} - T + V$ as [69]:

$$
\begin{aligned}
H = {} & \frac{1}{2}(p_x^2 + p_y^2 + p_z^2) + \omega(y p_x - x p_y) \\
& - \frac{\mu}{r} \sum_{n=0}^{\infty} \sum_{m=0}^{\infty} \left(\frac{r}{R_\oplus}\right)^{-n} P_n^m(\sin \delta) \\
& \times (C_{nm} \cos m\lambda + S_{nm} \sin m\lambda)
\end{aligned}
\tag{99}
$$

where μ is the Earth's gravitational parameter, $R_\oplus$ is the radius of Earth at the equator, and C_{nm}, S_{nm} are the geopotential coefficients. This effort uses NASA EGM-96 gravity model with an order and degree of 20. The relationship between rectangular coordinates and the radius, r, the latitude, δ, the longitude, λ, can be shown as [69]:

$$
\begin{aligned}
r &= \sqrt{x^2 + y^2 + z^2} \\
\sin \delta &= \frac{z}{\sqrt{x^2 + y^2}} \\
\tan \lambda &= \frac{y}{x}
\end{aligned}
\tag{100}
$$

where the rectangular coordinates are in a reference frame tied to the Greenwich, which is the Greenwich referenced ECR frame, see Section 2.4. The expansion of the geopotential in the zonal harmonics, which is $m = 0$, is used for constructing the periodic orbit. The sectoral and tesseral harmonics are added as perturbations to the periodic orbit. The Hamilton's equations can be represented as [69]:

$$
\dot{X} = Z \frac{\partial H}{\partial X},
\tag{101}
$$

where X is the physical state vector, $X^T = \{x, y, z, p_x, p_y, p_z\}$, and Z is a $2n \times 2n$ matrix, where n is the number of coordinates, that conveniently arranges the Hamilton's equations

in vector form as [69]:

$$\dot{X} = \left\{ \begin{array}{c} \dot{x} \\ \dot{y} \\ \dot{z} \\ \dot{p}_x \\ \dot{p}_y \\ \dot{p}_z \end{array} \right\} = \left\{ \begin{array}{cc} 0 & I \\ -I & 0 \end{array} \right\} \cdot \left\{ \begin{array}{c} \frac{\partial H}{\partial q_i} \\ \frac{\partial H}{\partial p_i} \end{array} \right\} = \left\{ \begin{array}{c} \frac{\partial H}{\partial p_x} \\ \frac{\partial H}{\partial p_y} \\ \frac{\partial H}{\partial p_z} \\ -\frac{\partial H}{\partial x} \\ -\frac{\partial H}{\partial y} \\ -\frac{\partial H}{\partial z} \end{array} \right\} \quad (102)$$

The linearization of the Hamilton's equations is needed because this effort is an estimation problem. The equations of variation can be represented as [69]:

$$\dot{x} = Z \frac{\partial^2 H}{\partial X^2} = Ax, \quad (103)$$

where x is represented as small changes to the physical state vector X.

Air drag perturbations are also added to the the combination periodic orbit and the Floquet solution. The momenta are inertial velocity components. Therefore, air drag acceleration can be represented as [69]:

$$\begin{aligned} a_{drag} &= -\frac{1}{2} \frac{C_d A \rho_o}{m} \frac{\rho}{\rho_o} \sqrt{p_x^2 + p_y^2 + p_z^2} \mathbf{p} \\ &= -B^* \frac{\rho}{\rho_o} \sqrt{p_x^2 + p_y^2 + p_z^2} \mathbf{p} \end{aligned} \quad (104)$$

where B^* is another measure for the susceptibility of a satellite to air drag , m is the satellite mass, and ρ is the atmospheric density at perigee. [60]. For further information, see Equation 84.

Symmetric About Polar Axis

J2
J3
J4
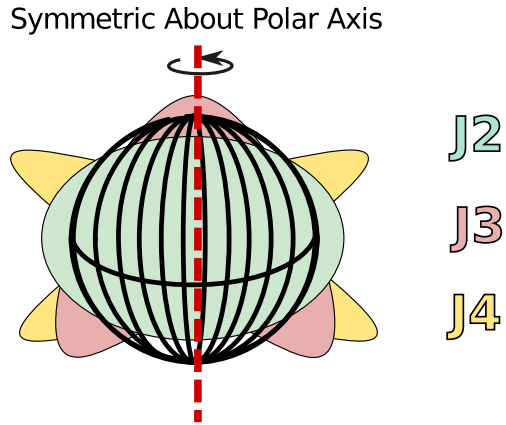
Figure 17. The Earth's Zonal Gravity Potential

3.3 Periodic Orbits

The periodic orbit and Floquet theory are used as starting point for calculating the perturbations because the previous KAM torus construction methods failed for low eccentricity orbits and the periodic orbit resides at the core of the torus. The modified Laskar algorithm, developed by Wiesel, is one of the KAM torus construction methods. It yields three basis frequencies for orbits by Fourier series spectral analysis. The low eccentricities are hard to be detected for methods like Laskar frequency analysis method, which requires high eccentricities that cause more dramatic change in the frequency spectrum of the orbit. Although this fact is a disadvantage for the previous KAM torus construction methods, it is favorable for this effort because the structure lies at the core of the torus is a periodic orbit.

In 1960's, the periodic orbits were studied extensively because they are more realistic than 2BP, which describes every orbit periodic. The Newtonian point mass plus the zonal harmonics terms lead to the periodic orbit because the zonal potential about polar axis is symmetric. Figure 17 represents the symmetry of the Earth's zonal potential about polar axis. Nearly circular orbits are periodic orbits in the Earth's zonal gravity potential for every inclination, except in the close vicinity of the critical inclination [58]. The periodic orbits are closely related to the frozen orbits, which have nearly stationary eccentricity
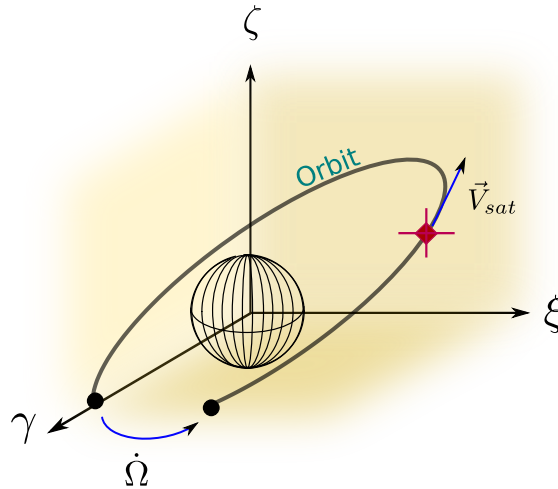
Figure 18. The Regression of Orbit Plane in the Zonal Gravity Potential

and argument of perigee. The repeated ground tracks are of great importance for mission planning. The periodic orbits defined in a reference frame tied to the rotating Earth have repeated ground tracks. Therefore, the periodic orbits have been studied as frozen orbits as well [44, 43]. It has been shown that nearly circular orbits are unstable at the critical inclination, and the periodic orbits in the vicinity of the critical inclination have high eccentricities [17]. The numerical proof of the existence of periodic orbits with high eccentricities has been done by Broucke [8]. Moreover, Wiesel has developed a new relative motion solution for satellites using the low eccentricity periodic orbits, but their potential use for orbit determination hasn't been explored until he uses the low eccentricity periodic orbits to construct the low eccentricity KAM torus [69].

In the zonal problem, there are periodic orbits. However, there are a few difficulties in building the periodic orbit. It is known that there are two non-zero frequencies, which are the Keplerian frequency and the regression of the node. These frequencies aren't known. The periodic orbit precesses at a certain rate which can only be determined when it finishes its motion for one period, and the orbits aren't periodic in inertial space. Therefore, defining the periodic orbit in a reference frame that rotates with the node is required. Fig-

64

ure 18 represents the regression of orbit plane under the influence of zonal potential. The periodicity condition needs to be set up in such a way that the nodal regression rate of the orbit plane is not needed. Therefore, the initial conditions are defined with position vector, $\mathbf{r} = \{x_o, 0, 0\}$, and momentum vector, $\mathbf{p} = \{\dot{x}_o, v_o \cos i_o, v_o \sin i_o\}$. The orbital period, τ, and inclination, i, define the orbit, while the unknowns are $\Xi^T = \{x_o, \dot{x}_o, v_o\}$. Because Earth doesn't have North/South symmetry, $\dot{x}_o$ is required as a component of the momentum vector, $\mathbf{p}$. The orbit becomes periodic if the 3 conditions after one revolution, τ, are set up as [69]:

$$G = \left\{ \begin{array}{c} z(\tau) \\ \mathbf{r}(\tau) \cdot \mathbf{p}(\tau) - x_o \dot{x}_o \\ \mathbf{r}(\tau) \cdot \mathbf{r}(\tau) - x_o^2 \end{array} \right\} = 0, \tag{105}$$

where the conditions dictate the satellite to cross the equatorial plane, $z(\tau) = 0$, to have the same radial velocity as at the beginning, $\mathbf{r}(\tau) \cdot \mathbf{p}(\tau) - x_o \dot{x}_o = 0$, and to be at the same distance from Earth as at the beginning. The actual orbit precession isn't known, but can be calculates as [69]:

$$\dot{\Omega} = \frac{1}{\tau} \cos^{-1} \frac{\mathbf{r}(\tau) \cdot \mathbf{r}(0)}{|\mathbf{r}(\tau)| \, |\mathbf{r}(0)|} = \frac{1}{\tau} \cos^{-1} \frac{x(\tau)}{x(0)} \tag{106}$$

A linearization of Equation 105 using Taylor's series expansion is required to obtain the periodic orbit [69]:

$$\mathbf{G} = \mathbf{G}(\Xi) + \frac{\partial \mathbf{G}}{\partial \Xi} \delta \Xi = 0 \tag{107}$$

The expansion using the state transition matrix $\Phi(\tau, 0)$, which is calculated from parallel numerical integration with the trajectory, yields the derivative matrix of $\mathbf{G}$ [69]:

$$\begin{aligned} \frac{\partial \mathbf{G}}{\partial \Xi} &= \frac{\partial \mathbf{G}}{\partial \mathbf{X}(\tau)} \frac{\partial \mathbf{X}(\tau)}{\partial \Xi} + \frac{\partial \mathbf{G}}{\partial \mathbf{X}(0)} \frac{\partial \mathbf{X}(0)}{\partial \Xi} \\ &= \left(\frac{\partial \mathbf{G}}{\partial \mathbf{X}(\tau)} \Phi(\tau, 0) + \frac{\partial \mathbf{G}}{\partial \mathbf{X}(0)} \right) \frac{\partial \mathbf{X}(0)}{\partial \Xi} \end{aligned} \tag{108}$$

where $\Phi(\tau,0)$ can be calculated from $\partial \mathbf{X}(\tau)/\partial \mathbf{X}(0)$. The partial derivatives in the Equation 107 can be computed as [69]:

$$\frac{\partial \mathbf{G}}{\partial \mathbf{X}(\tau)} = \left\{ \begin{array}{cccccc} 0 & 0 & 1 & 0 & 0 & 0 \\ \dot{x} & \dot{y} & \dot{z} & x & y & z \\ 2x & 2y & 2z & 0 & 0 & 0 \end{array} \right\}$$

$$\frac{\partial \mathbf{G}}{\partial \mathbf{X}(0)} = \left\{ \begin{array}{cccccc} 0 & 0 & 0 & 0 & 0 & 0 \\ -\dot{x}_o & 0 & 0 & -x_o & 0 & 0 \\ -2x_o & 0 & 0 & 0 & 0 & 0 \end{array} \right\} \tag{109}$$

$$\frac{\partial \mathbf{X}(0)}{\partial \Xi} = \left\{ \begin{array}{cccccc} 1 & 0 & 0 & 0 & 0 & 0 \\ 0 & 0 & 0 & 1 & 0 & 0 \\ 0 & 0 & 0 & 0 & \cos i_o & \sin i_o \end{array} \right\}^{T}$$

Then, the initial condition parameter vector, Ξ, can be corrected by the correction, $\delta \Xi$, which can be calculated by Equation 107 [69].

After the periodic orbit is built, it is represented as a Fourier series by harmonic analysis [23]. Figure 19 shows the representation of the periodic orbit by two angle variables. In Figure 19, Q_1 is "mean argument of latitude analogue", and Q_2 is regression of the right ascension of ascending node. Q_1 and Q_2 are the physical coordinates of the KAM torus [69] :

$$Q_1 = M + \Omega, \tag{110}$$

$$Q_2 = \Omega - \theta_g, \tag{111}$$

where M is mean anomaly, Ω is right ascension of ascending node, and θ_g is angle between the vernal equinox and the prime meridian. The periodic orbit is a function of only Q_1 in a frame of reference, which is the ECNF frame, see Section 2.4, that rotates with the ascend-
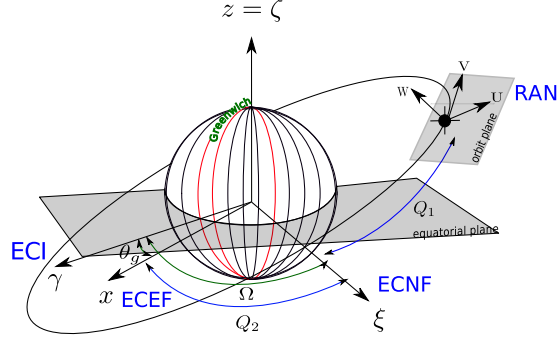
Figure 19. The Representation of the Periodic Orbit by Angle Variables

ing node. The nodal orbital frequency, ω_1, and the inertial nodal regression rate, ω_2, can be obtained from the Fourier series. These Fourier series store only the coordinates, ξ, η, and ζ, because the momenta can be obtained by the kinematic relations in Equation 98. Moreover, it is a simple matter to generalize from ECEF frame to ECI or ECEF frames because the zonal potential is symmetric about polar axis. The inertial nodal regression rate, ω_2, needs to be updated to define the regression rate with respect to the Greenwich. Equation 112 represents that the periodic orbit defined in ECNF frame, where the periodic orbit, $\mathbf{X}$, is a function of only Q_1, can be transformed to ECI or ECEF frame with a double rotation matrix about the z axis by the nodal angle Q_2 [69]:

$$\mathbf{X}_{ECEF}(Q_1, Q_2) = \left\{ \begin{array}{cc} R_z(-Q_2) & 0 \\ 0 & R_z(-Q_2) \end{array} \right\} \mathbf{X}_{ECNF}(Q_1) \qquad (112)$$

Equation 112 can also be used when the desired reference frame is ECI instead of ECEF with small modifications. Both Q_2 in the equation are substituted by the usual initial frame node, Ω, and ω_2 is reduced by the Earth's rotation to transform the periodic orbit, $\mathbf{X}$, from ECNF frame to ECI frame. Although the two frequencies have been obtained from the periodic orbit, the third frequency is required for the solution.

67

3.4 Floquet Solution

Periodic orbits plus the Floquet solution provides a method that numerically solves dynamical problems which don't have closed form solution. The linearization of the periodic orbit describes the behaviour of the system near the periodic orbit. Linearizing about the periodic orbit results in a linearization problem [64]:

$$\dot{x} = A(t)x, \tag{113}$$

where x is the first order displacements from the state X. Equation 113 is a time periodic linear differential equations. The solution to time periodic linear differential equations yields stability information of periodic orbits. The solution to the Equation 113 can be obtained as [64]:

$$\Phi(t,t_o) = E(t)exp(J(t-t_o))E^{-1}(t_o), \tag{114}$$

where E is a periodic matrix, J is a matrix of system frequencies in the Jordan normal form. The system frequencies are also called Poincaré exponents.

The Floquet solution can be obtained by calculating the Jordan normal form, J, and the periodic matrix, E, over one period. Over one period, Equation 114 becomes [64]:

$$\Phi(t,0) = E(t)exp(Jt)E^{-1}(0), \tag{115}$$

where $E(t) = E(0)$ because E is periodic. Figure 20 represents the visual depiction of E periodic matrix. Geometrically, defining $E(t) = E(0)$ puts a sets of coordinates on the periodic orbit, and they follow the trajectory by rotating around themselves. At the end these sets of coordinates smoothly join themselves. Φ is the state transition matrix over a period. Indeed, because the system is periodic, we have Φ for all time. The Φ matrix is called monodromy matrix. The eigenvalues and eigenvectors of the Φ matrix can be found
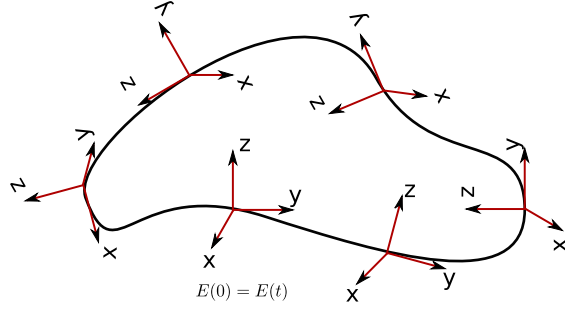
Figure 20. E Periodic Matrix

by rearranging Equation 114 [64]:

$$E(0)^{-1}\Phi(t,0)E(0) = e^{Jt}, \tag{116}$$

where the exponential of the Jordan form J, is the eigenvalue matrix of Φ. E periodic matrix yields the eigenvalues of the Φ matrix. If λ_i are eigenvalues of the monodromy matrix, Equation 116 becomes [64]:

$$\lambda_i = e^{\omega_i t}$$
$$\omega_i = \frac{1}{t} \ln \lambda_i \tag{117}$$

where ω_i are the system frequencies, which are also called Poincaré exponents. The interpretation of the Poincaré exponents is similar to the eigenvalues of a constant coefficient system. For Hamiltonian systems without dissipation, the frequencies must be a pair of positive / negative real numbers or a pair of a pair of imaginary numbers. As an exception, when $\lambda_i = 0$, there is a repeated value of $\omega_i = 0$. Repeated roots in linear systems lead to off-diagonal time terms. These pair of zeros are called a degenerate mode. For this effort, the Hamiltonian has two integrals of the motion, which are the Hamiltonian itself , and the z component of the angular momentum. Because each of these pair of zeros correspond to one integral of motion, this effort has two degenerate modes. Each degenerate mode involves a static displacement and a linear drift is associate momentum is not zero. These

69

static displacements can occur either along the orbit or around the polar axis. These two degenerate modes correspond to two frequencies. The third frequency is the free eccentricity of the orbit, which is a pair of imaginary frequencies by the eigenvalue calculation, because the imaginary part of ω_i is the oscillatory frequency of the mode i. For this effort, the oscillatory frequency is $\pm\omega_3$ with algebraic sign that depends on the inclination. As a result, the calculation of eigenvalues yields the complete linear stability information of the periodic orbit [64, 69].

The calculation of eigenvector yields $E(t)$ over one period, which can be used to transform from physical variables to model variables. The eigenvalue problem for equation is highly singular, and a special treatment is required. The differentiation of the state transition matrix becomes [63]:

$$\dot{\Phi}(t,t_o) = \dot{E}(t)e^{J(t-t_o)}E^{-1}(t_o) + E(t)Je^{J(t-t_o)}E^{-1}(t_o) \tag{118}$$

By substituting into Equation 119 :

$$\dot{\Phi}(t,t_o) = A(t)\Phi(t,t_o) \tag{119}$$

A differential equation for F(t) becomes:

$$\dot{E}(t)e^{J(t-t_o)}E^{-1}(t_o) + E(t)Je^{J(t-t_o)}E^{-1}(t_o) = A(t)E(t)exp(J(t-t_o))E^{-1}(t_o)$$
$$\dot{E}(t) + E(t)J = A(t)E(t) \tag{120}$$
$$\dot{E} = AE - EJ$$

Since $E(0)$ is obtained from the periodic orbit, solving Equation 120 from $t = 0$ to t yields F(t) over one period. $E(t)$ periodic matrix is reduced to Fourier series [23]. For this effort, the periodic matrix is a function of Q_1, $E(Q_1)$.

The transformation from physical coordinates to modal variables is possible because

$F(t)$ periodic matrix is calculated. Assuming y is the modal variable [63]:

$$y = E^{-1}(t)x \tag{121}$$

By substituting into Equation 122 :

$$x(t) = \phi(t,t_o)x(t_o) \tag{122}$$

The Floquet solution represented in modal variables becomes :

Table 9. Analogous of Modal Variables

Modal Variables	Analogous of Modal Variables
y_1	a displacement along the argument of latitude direction, Q_1.
y_2	a change in the momentum which is analogous to the Delaunay momentum, L.
y_3	an offset in the nodal variable, Q_2.
y_4	a change in the z component of orbital angular momentum.
y_5	$e\cos\omega$
y_6	$e\sin\omega$

$$x(t) = E(t)e^{J(t-t_o)}E^{-1}(t_o)x(t_o)$$

$$E^{-1}(t)x(t) = e^{J(t-t_o)}E^{-1}(t_o)x(t_o) \tag{123}$$

$$y(t) = e^{J(t-t_o)}y(t_o)$$

Equation 123 is a solution to the linear system to the form [69]:

$$\dot{y} = Jy \tag{124}$$

71

The Floquet solution can be added to the periodic orbit solution as :

$$\mathbf{X}_{ECR} = R_z(-Q_2)\{\mathbf{X}_{PO}(Q_1) + E(Q_1)exp(J(t-t_o))y(t_o)\}, \tag{125}$$

where double z rotation is represented as R_z, the nodal frame periodic orbit series are shown as $(X)_{PO}$. The modal variables , y_1 and y_2, are local versions of the global angles , Q_1 and Q_2, and they are scaled to suit this purpose. The Jordan form matrix becomes :

$$exp(J(t-t_o)) = \begin{Bmatrix} 1 & t-t_o & 0 & 0 & 0 & 0 \\ 0 & 1 & 0 & 0 & 0 & 0 \\ 0 & 0 & 1 & t-t_o & 0 & 0 \\ 0 & 0 & 0 & 1 & 0 & 0 \\ 0 & 0 & 0 & 0 & \cos Q_3 & \sin Q_3 \\ 0 & 0 & 0 & 0 & -\sin Q_3 & \cos Q_3 \end{Bmatrix} \tag{126}$$

The modal variables are analogous to 6 orbital elements that can be used to represent nearby motion. Table 9 represents an analogy between modal variables and miscellaneous orbital elements. The global variables, Q_1 and Q_2, should be freely traded with the modal variables, y_1 and y_3, because this will keep them from growing unboundedly [69].

3.5   First-Order Perturbations

The periodic orbit and its Floquet solution has been obtained from Equation 125. This solution has the Newtonian term and all of the zonal gravity harmonics. The perturbations start approximately on the order of 10^{-5} instead of 10^{-3}, which is advantageous because errors originated from the calculation of perturbations are less influential. However, the method for calculating first-order perturbations can be extended to higher order perturbations. This effort includes only sectoral and tesseral harmonics and air drag. However, the

72

exact same method applies to lunar and solar mass perturbations by including at least one extra angle in the Fourier series which describes the motion of the Moon or the Sun with respect to Earth in a frame that rotates with it. The perturbing force, $\dot{\mathbf{X}}_{pert}$, can be added to Equation 113 as [69]:

$$\dot{x} = Ax + \dot{\mathbf{X}}_{pert} \tag{127}$$

The perturbing acceleration can be expanded about the periodic orbit because this is a forced linear system [69]:

$$
\begin{aligned}
\dot{\mathbf{X}}_{pert} &\approx \dot{\mathbf{X}}_{pert}\big|_{\mathbf{X}_{PO}} + \frac{\partial \mathbf{X}_{pert}}{\partial \mathbf{X}}\bigg|_{\mathbf{X}_{PO}} x + \dots \\
&= \dot{\mathbf{X}}_{pert}\big|_{\mathbf{X}_{PO}} + \frac{\partial \mathbf{X}_{pert}}{\partial \mathbf{X}}\bigg|_{\mathbf{X}_{PO}} Ey + \dots
\end{aligned} \tag{128}
$$

The first-order perturbations can be added to the Floquet solution by Equation 124 as [69]:

$$
\dot{y} = \left\{
\begin{array}{cccccc}
1 & 0 & 0 & 0 & 0 & 0 \\
0 & 1 & 0 & 0 & 0 & 0 \\
0 & 0 & 1 & 0 & 0 & 0 \\
0 & 0 & 0 & 1 & 0 & 0 \\
0 & 0 & 0 & 0 & 0 & \omega_3 \\
0 & 0 & 0 & 0 & -\omega_3 & 0
\end{array}
\right\} y + E^{-1}\dot{\mathbf{X}}_{pert}, \tag{129}
$$

where for sectoral and tesseral perturbations, the trailing term, $E^{-1}\dot{\mathbf{X}}_{pert}$, is a function of the global variables, Q_1 and Q_2. The forcing term can be transformed to a double Fourier series in these angles. This applies to air drag as well. However, the air drag forcing term is a function of only one global variable, Q_1.

For the first-order perturbations, a perturbing acceleration transformed to the modal variables is decoupled. Two different terms, which are the constant and periodic Fourier series terms, are examined for the perturbing acceleration as the response to the oscilla-

73

tory and the two degenerate modes. Each factor is evaluated separately. A constant solu-
tion is obtained from the constant terms in the Fourier series for the oscillatory mode by
Equation129 as [69]:

$$\begin{pmatrix} \dot{y}_5 \\ \dot{y}_6 \end{pmatrix} = \begin{pmatrix} 0 \\ 0 \end{pmatrix} = \left\{ \begin{matrix} 0 & \omega_3 \\ -\omega_3 & 0 \end{matrix} \right\} \begin{pmatrix} y_5 \\ y_6 \end{pmatrix} + \begin{pmatrix} c_5 \\ c_6 \end{pmatrix} \qquad (130)$$

Then, the solution to the Equation 130 becomes [69]:

$$\begin{pmatrix} y_5 \\ y_6 \end{pmatrix} = \begin{pmatrix} c_6/\omega_3 \\ -c_5/\omega_3 \end{pmatrix} \qquad (131)$$

These terms can't be ignored because ω_3 is a small number for the most part. The modal
variables, y_1 and y_2, don't become infinite near the periodic orbit, which has zero eccen-
tricity for this effort, because they are analogous to the quantities, *ecos* ω and *esin* ω, in
the 2BP. The constant terms in the Fourier series for one of the degenerate modes doesn't
yield a constant solution [69]:

$$\begin{pmatrix} \dot{y}_1 \\ \dot{y}_2 \end{pmatrix} = \left\{ \begin{matrix} 0 & 1 \\ 0 & 0 \end{matrix} \right\} \begin{pmatrix} y_1 \\ y_2 \end{pmatrix} + \begin{pmatrix} c_1 \\ c_2 \end{pmatrix} \qquad (132)$$

Then, the solution becomes:

$$\begin{pmatrix} y_1 \\ y_2 \end{pmatrix} = \begin{pmatrix} (c_1 - y_2(t_o))(t - t_o) + \frac{1}{2}c_2(t^2 - t_o^2) \\ c_2 t - y_2(t_o) \end{pmatrix}, \qquad (133)$$

where the solution for $\dot{y}_2 = c_2$ is written at the start time because the other secular terms,
which appear due to the periodic perturbations in y_2, can be absorbed. The solution for y_1
has been obtained by substituting y_2 into y_1. Equation 133 represents that y_1 and y_2 could

74

have quadratic terms, and y_2 and y_4 could have a linear rate of change. When there is no dissipative force in the system, c_2 should be zero, and a quadratic term isn't expected for in-track and nodal perturbation. For air drag perturbation, quadratic behavior is expected. y_1 and y_2 can be observed by their associated global variables because the modal variables aren't scaled. The exact same approach is taken for periodic Fourier terms.

The periodic terms in the Fourier series for a degenerate mode yields the forced linear system as[69]:

$$
\begin{pmatrix} \dot{y}_1 \\ \dot{y}_2 \end{pmatrix} = \left\{ \begin{matrix} 0 & 1 \\ 0 & 0 \end{matrix} \right\} \begin{pmatrix} y_1 \\ y_2 \end{pmatrix}
$$
$$
+ \begin{pmatrix} c_1 \, cos(n_1 Q_1 + n_2 Q_2) + s_1 \, sin(n_1 Q_1 + n_2 Q_2) \\ c_2 \, cos(n_1 Q_1 + n_2 Q_2) + s_2 \, sin(n_1 Q_1 + n_2 Q_2) \end{pmatrix}
\tag{134}
$$

where the setup is for sectoral and tesseral harmonics, but if a perturbation requires it, an additional angle can be introduced. In the equation, n_1 and n_2 are integers, and $w_p = n_1 \omega_1 + n_2 \omega_2$. The solution for y_2 can be calculated [69]:

$$
y_2(t) = \left(\frac{c_2}{\omega_p} \, sin(n_1 Q_1 + n_2 Q_2) - \frac{s_2}{\omega_p} \, cos(n_1 Q_1 + n_2 Q_2) \right) \Big|_{t_o}^{t}
\tag{135}
$$

Then, substituting into the y_1 yields :

$$
y_1(t) = \left\{ \left(\frac{c_1}{\omega_p} - \frac{s_2}{\omega_p^2} \right) \, sin(n_1 Q_1 + n_2 Q_2) - \left(\frac{s_1}{\omega_p} - \frac{c_2}{\omega^2} \right) \, cos(n_1 Q_1 + n_2 Q_2) \right\} \Big|_{t_o}^{t}
$$
$$
- \left(\frac{c_2}{\omega_p} \, sin(n_1 Q_1 + n_2 Q_2) - \frac{s_2}{\omega_p} \, cos(n_1 Q_1 + n_2 Q_2) \right) \Big|_{t_o}^{t}
\tag{136}
$$

where the constant terms in the y_2 solution lead to time dependent terms in the solution for y_1. However, the secular terms introduced by the constant terms in the y_2 solution has already been absorbed into the solution provided by Equation 133.

The remaining forced linear system is due to the periodic terms in the oscillatory mode. Equation 137 represents the forced linear system [69]:

$$
\begin{pmatrix} \dot{y}_5 \\ \dot{y}_6 \end{pmatrix} = \left\{ \begin{matrix} 0 & \omega_3 \\ -\omega_3 & 0 \end{matrix} \right\} \begin{pmatrix} y_5 \\ y_6 \end{pmatrix}
$$
$$
+ \begin{pmatrix} c_5\,cos(n_1Q_1+n_2Q_2)+s_5\,sin(n_1Q_1+n_2Q_2) \\ c_6\,cos(n_1Q_1+n_2Q_2)+s_6\,sin(n_1Q_1+n_2Q_2) \end{pmatrix}
\tag{137}
$$

Let both a forced solution and the perturbation term has the same form:

$$
\begin{pmatrix} y_5 \\ y_6 \end{pmatrix} = \begin{pmatrix} \alpha_5\,cos(n_1Q_1+n_2Q_2)+\beta_5\,sin(n_1Q_1+n_2Q_2) \\ \alpha_6\,cos(n_1Q_1+n_2Q_2)+\beta_6\,sin(n_1Q_1+n_2Q_2) \end{pmatrix}
\tag{138}
$$

After inserting assumed solution and simplifying it, the solution becomes a set of linear equations for the forcing coefficients as:

$$
\alpha_5 = \frac{c_6\omega_3+s_5\omega_p}{\omega_3^2-\omega_p^2}, \quad \beta_5 = \frac{s_6\omega_3-c_5\omega_p}{\omega_3^2-\omega_p^2}
$$
$$
\alpha_6 = \frac{-c_5\omega_3+s_6\omega_p}{\omega_3^2-\omega_p^2}, \quad \beta_6 = \frac{-s_5\omega_3-c_6\omega_p}{\omega_3^2-\omega_p^2}
\tag{139}
$$

Once the perturbing Fourier series is obtained, it is converted to the perturbation solution, and stored. This method can be applied to any other perturbations with simple modifications, and the code written for this method requires only the new data file and truncation level associated with the perturbation. It should be noted that Equation 139 includes the expected small divisors problem, which will lead to problems near the resonance.

Equation 125 can be modified to include the first-order perturbations as[69]:

$$
\mathbf{X}_{ECR} = R_z(-Q_2)\left\{ \mathbf{X}_{PO}(Q_1)+E(Q_1)\left[exp(J(t-t_o))y_{free}(t_o)+y_{forced} \right] \right\},
\tag{140}
$$

where the modal variables from the Floquet solution is represented by y_{free}, and the perturbed solution is denoted by y_{forced}. The perturbed solution, y_{forced}, can be a function of different angles, depending on the perturbation.

3.6 Second-Order Eccentricity Perturbations

The modal variables, y_1 and y_3, are necessary for fitting orbit and for small perturbations. The global angles Q_1 and Q_2 absorb the large changes. Moreover, secular terms may be absorbed in their frequencies, ω_1 and ω_2. However, the expansion of the torus along, y_5 and y_6, which describe the eccentricity and argument of perigee states, is necessary because not all orbits have small enough eccentricities. The equation for the expansion of the two model variables, y_5 and y_6, when setting the other model variables approximately zero in physical variables becomes [69]:

$$
\begin{aligned}
\dot{x}_i &= Z_{i\alpha} \frac{\partial^2 H}{\partial X_\alpha \partial X_\beta}\bigg|_{X_{PO}} x_\beta + \frac{1}{2} Z_{i\alpha} \frac{\partial^3 H}{\partial X_\alpha \partial X_\beta \partial X_\gamma}\bigg|_{X_{PO}} x_\beta x_\gamma + ... \\
&= A_{i\alpha}(Q_1) x_\alpha + \frac{1}{2} B_{i\alpha\beta}(Q_1) x_\alpha x_\beta
\end{aligned}
\tag{141}
$$

where Z is the symplectic matrix, $i = (1...6)$ for this specific case, the linear, time varying differential equations are the equations of variation. Representing the equation in the modal variables, Equation 141 becomes:

$$
\begin{aligned}
\dot{y}_i &= J_{i\alpha} y_\alpha + \frac{1}{2} E_{i\alpha}^{-1} B_{\alpha\beta\gamma} E_{\beta\delta} E_{\gamma\varepsilon} y_\delta y_\varepsilon + ... \\
&= J_{i\alpha} y_\alpha + \frac{1}{2} B'_{i\alpha\beta} y_\alpha y_\beta + ...
\end{aligned}
\tag{142}
$$

where B'_{ijk}, the periodic orbit, and the E matrix are periodic functions of Q_1. The quadratic matrix, B'_{ijk} with y_5 and y_6 portion in the final two indices yields a periodic six by two by two tensor [69].

Assuming all model variables are zero except the eccentricity mode, the linear matrix

becomes:

$$J = \left\{ \begin{array}{cc} 0 & \omega_3 \\ -\omega_3 & 0 \end{array} \right\} \tag{143}$$

Then, the linear solution can easily be obtained as:

$$y(t) = \Phi(t,t_o)y(t_o) = \left\{ \begin{array}{cc} \cos\omega_3(t-t_o) & \sin\omega_3(t-t_o) \\ -\sin\omega_3(t-t_o) & \cos\omega_3(t-t_o) \end{array} \right\} y(t_o) \tag{144}$$

If the quadratic terms in the Equation 142 is small enough, the first order solution, $y(t) = \Phi(t,t_o)y(t_o)$, can be used for the equation as:

$$\begin{aligned} \dot{y}_i &= J_{i\alpha}y_\alpha + \frac{1}{2}B'_{i\alpha\beta}\Phi_{\alpha\gamma}\Phi_{\beta\delta}y_\gamma(0)y_\delta(t_o) \\ &= J_{i\alpha}y_\alpha + \frac{1}{2}B"_{i\alpha\beta}y_\alpha(t_o)y_\beta(t_o) \end{aligned} \tag{145}$$

where $B"$ is a function of both Q_1 and $Q_3 = \omega_3(t-t_o)$. The solution to Equation 145 is assumed to be generalized as [69]:

$$y_i(t) = \Phi^{(1)}_{t_o}y_\alpha(t_o) + \frac{1}{2}\Phi^{(2)}_{i\alpha\beta}y_\alpha(t_o)y_\beta(t_o) + ... , \tag{146}$$

where $\Phi^{(1)}(t_o,t_o) = I$,as it is in the classical linear system theory, and $\Phi^{(2)}(t_o,t_o) = 0$ because the initial conditions, $y_i(t_o)$, need to be preserved. Therefore, the time derivative of Equation 146 can easily be calculated because $y_i(t_o)$ are constant. Inserting the time derivative in the form of the modal differential Equation 145 yields [69]:

$$\begin{aligned} \dot{y}_i &= \dot{\Phi}^{(1)}_{t_o}y_\alpha(t_o) + \frac{1}{2}\dot{\Phi}^{(2)}_{i\alpha\beta}y_\alpha(t_o)y_\beta(t_o) + ... \\ &= J_{i\beta}\Phi^{(1)}_{\beta\alpha}y_\alpha(t_o) + \frac{1}{2}J_{i\gamma}\Phi^{(2)}_{\gamma\alpha\beta}y_\alpha(t_o)y_\beta(t_o) \\ &\quad + \frac{1}{2}B"_{i\alpha\beta}y_\alpha(t_o)y_\beta(t_o) \end{aligned} \tag{147}$$

78

where the arbitrary indices are for a uniformity requirement in the initial conditions. The first order state transition matrix differential equation can be obtained as [69]:

$$\dot{\Phi}_{ij}^{(1)} = J_{i\beta}\Phi_{\beta j}^{(1)} \tag{148}$$

Then, the new result in the second order becomes:

$$\dot{\Phi}_{ijk}^{(2)} = J_{i\gamma}\Phi_{\gamma jk}^{(2)} + B"_{ijk}, \tag{149}$$

where it is already known that $\Phi_{ijk}^{(2)}(t_o,t_o) = 0$. The solution for Equation 149 has been provided for the constant terms in the Fourier series of $B"$ by Equation 131 and by Equation 139 for the periodic terms. If indices j and k are constant, the solution to the system will be same as the first order case. Therefore, $\Phi^{(2)}$ will be a periodic function of the global variables, Q_1 and Q_3. The extension to higher order of the eccentricity/argument of perigee is believed to better characterize the short periodic oscillations.

3.7   Least Squares Fit to SGP4 and TLE Data

For this method, the point on the periodic orbit that corresponds to the epoch time of SGP4 and TLE data should be calculated in terms of Q_1 and Q_2. From the perspective of estimation theory, a reference trajectory should be corrected to yield an estimate of the actual trajectory. For this effort, the low eccentricity KAM torus predictions are considered as the reference trajectory, and the SGP4 and TLE predictions are considered as the observational data. Wiesel and Frey showed that the KAM torus basis frequencies can be obtained from SGP4 and TLE data. The desired periodic orbit is the one with zero y_2 and y_4 model variables. The least squares routine for this effort fits the low KAM torus to the SGP4 and TLE data by updating the global variables, Q_1 and Q_2, the frequencies, ω_1 and ω_2, and B^*. The convergence criterion is met when the estimate correction vectors of modal variables,
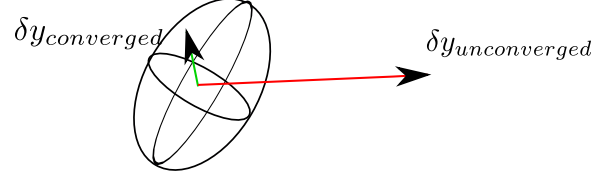
Figure 21. The Converged and Unconverged State Correction Vectors

δy_i, are smaller than 1% of the sigma values, σ_i. Convergence for least squares method depends on the correction vectors and the error ellipsoid. If the correction vectors lie well within the 1σ error ellipsoid [67]. Figure 21 represents the converged and unconverged state correction vectors.

This effort uses nonlinear least squares. This method combines the SGP4 and TLE data, which has been propagated for an orbit over two months, and the low eccentricity KAM torus to form an estimate. For each observation, t_i, a series of calculations are made for nonlinear least squares method. First, the state transition matrix is obtained , $\Phi(t_i, t_o)$, by propagating the state vector to the observation time, t_i. Second, the residual vector, $r_i = z_i - G(x)$, is calculated. The SGP4 and TLE data are represented as z_i, and the low KAM torus data are represented as $G(x)$. Third, the observation matrix, $T_i = H_i\Phi$, the covariance matrix, $P_{\delta x}$, and the state correction vector at epoch are calculated as [67]:

$$T_i = H_i\Phi$$
$$P_{\delta x} = (\sum_i T_i^T Q_i^{-1} T_i)^{-1} \tag{150}$$
$$\delta x(t_o) = P\delta x \sum_i T_i^T Q_i^{-1} r_i$$

where Q_i is a matrix that has sigma errors associated with the measurements, H_i is observation function linearization matrix. Then, the reference trajectory is corrected as:

$$x_{ref+1}(t_o) = x_{ref}(t_o) + \delta x(t_o) \tag{151}$$

80

Table 10. Three Shortcomings of the Least Squares Method [11]

1	Although every observation has different accuracy for the observations, each observation is weighted equally, which is a problem when there is observation with poor accuracy because the least squares method will be biased towards them.
2	The errors can be correlated, not independent as least squares method considers them to be.
3	The method soesn't consider that the errors are samples from a random process, and it doesn't utilize any statistical information
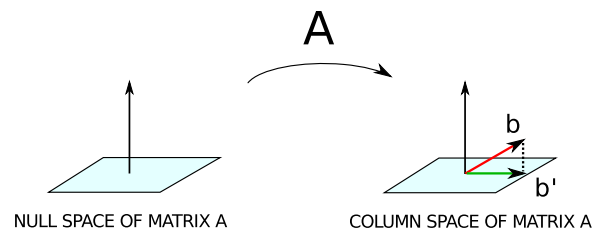
Figure 22. The Visual Depiction of the Least Squares Method

Finally, the process ends when a desired limit for the convergence is met. However, there are short comings of the least squares solution, which are listed in Table 10. In addition, Figure 22 shows the visual depiction of least squares method. The least squares method yields the the projection of the solution in the column space, where the solution is supposed to exist. Therefore, in a sense, the least square method minimizes $(A\vec{x} - \vec{b})^2$, and yields the closest approximate of the solution.

3.8 Summary

The geometry of the core of torus in the full geopotential appears to be a multiply-periodic two dimensional ribbon structure as a function of the argument of latitude angle, Q_1, and the nodal angle, Q_2, whereas it is a periodic orbit in the zonal potential. The orbital eccentricity is a mode of oscillation, which has been expanded to the second order. For the low eccentricity KAM torus theory, each satellite has a set of data files for the periodic

orbit, the modal E matrix, and perturbation series in the form of Fourier series. The periodic orbit has two large angles, Q_1 and Q_2, and four small parameters, y_2, y_4, y_5, and y_6. The change in the two angles is quite large, but the small parameters are expected to be small all the time. The theory includes two parts. The first part is a data package of Fourier series, which need occasional update. The second part is a set of seven parameters, Q_1, Q_2, y_2, y_4, y_5, y_6, and B^*, at epoch t_o which require more frequent update. Multiply-structured Fourier series define the trajectory under modeled perturbations, and it is specialized to a particular satellite because it is a numerical method. However, it takes less than a minute on a modern personal home computer [69]. After the theory files are built and the SGP4 and TLE propagation is obtained, the low KAM torus is fitted to the SGP4 and TLE data because the point on the torus that matches the epoch time of SGP4 and TLE data must be found. Moreover, the fitting process corrects the frequencies of the torus, ω_1 and ω_2, and it figures out the B^* value for the propagation period. It should be noted that the actual accuracy that can be achieved by this theory is supposed to be far better with the raw observational data than SGP4 and TLE data due to the inaccuracies in the SGP4 and TLE. The whole process from the SGP4 and TLE propagation to the least squares fitting needs no human intervention because all scripts are linked by bash files. The author modified every script to be both compatible for Windows$^{\text{TM}}$, and GNU/Linux platforms. The computational part of this effort has been conducted on a 64-bit GNU/Linux machine.

IV. Results and Analysis

In this chapter, the results will be presented and discussed. 1500 TLEs were obtained from `www.space-track.com` servers, and each were propagated for an orbit for 2 months. Then, the low KAM torus theory files were created, which are associated with the periodic orbit, sectoral and tesseral, eccentricity, and air drag perturbations. Finally, the low eccentricity KAM torus was fitted to the SGP4 and TLE propagation data, and the residuals were calculated. Therefore, the least squares fitting routine not only locates the epoch point on the KAM torus and corrects the frequencies, but also yields residuals. The first section presents the success rate for convergence between the low eccentricity KAM torus and the SGP4 and TLE data, and provides details related to the root causes of failures. Each failure was analyzed individually. The second section presents the relationship between orbital characteristics and residuals for all 1500 test cases. Again, some plots for failed cases are provided to figure out the root causes of the failures. The third section discusses and analyzes position and velocity residual plots for LEO and GEO objects in the RAN reference frame, see Section 2.4. The fourth section describes the optimal mean orbital limitations that never fail the convergence of the low eccentricity KAM torus. The fifth section compares the low eccentricity KAM torus and the SGP4 predictions for the best fit and a mean test case. The last section summarizes the chapter.

4.1 Overview of Results

All publicly available TLEs which have eccentricity on the order of 10^{-3} and smaller were retrieved from the `www.spacetrack.com` servers. 1500 TLEs were pseudo-randomly selected to fit the conditions mentioned in Section 3.1. First, each TLE was propagated for an orbit for 2 months period of time. Next, the periodic orbit, and its linearization, which is Floquet solution, for each test case was calculated, and perturbations were added to the

83

Table 11. Rms Values for Least Squares Fitting of 1500 Test Cases

Rms range (Km)	Percentage
$0 - 0.5$	0.6%
$0.5 - 1$	8.53333%
$1 - 3$	8.13333%
$3 - 5$	3.73333%
$5 - 10$	5.53333%
$10 - 20$	8.93333%
$20 - 40$	8.06667%
$40 - 100$	4.86667%
$100 - 200$	4.2%
> 200	4.26667%

solution. Then, the SGP4 and TLE data were fit using least squares, and the residuals for each test case were calculated. The success rate for convergence is 56.8667%. Table 11 represents the percentage of different range of rms values for all 1500 test cases. It should be noted that these percentages will increase if the propagation time period is smaller, because air drag is stochastic, and 2 months is long enough to terminate the torus. Therefore, another analysis was conducted. One hundred failed test cases were pseudo-randomly selected and propagated for 20 days instead of 2 months. The success rate of least squares fitting over 20 days is 66%. Table 12 shows the rms values for the 100 previously failed test cases. It is clear that the air drag is the root cause of the failure for 66 test cases. The other 34 test cases will be analyzed individually in order to find the root causes of the failure. Table 13 represents the 34 failed test cases for the second time.

Iridium 68, NORAD id 25291, is an operational satellite. Therefore, maneuvers for orbit maintenance, or attitude control maneuvers might cause the failure. Another reason for the failure might be its relatively low height of semi-major axis and high B^* values, which are $7.1558000e + 03$ km and $2.0938000e - 04$, respectively. Iridium 68 was propagated from 02-01-2013 to 02-09-2013 in order to check whether the air drag effect is the reason for the failure. However, the fitting process yields residuals on the order of 10^7 for

Table 12. Rms Values for Least Squares Fitting of the 100 Previously Failed Test Cases

Rms range (Km)	Percentage
$0 - 0.5$	0%
$0.5 - 1$	3%
$1 - 3$	15%
$3 - 5$	5%
$5 - 10$	9%
$10 - 20$	3%
$20 - 40$	5%
$40 - 100$	4%
$100 - 200$	8%
> 200	14%

the second time, which is a typical error characteristic for polar inclination. Therefore, it is concluded that its inclination of $8.6397400e + 01°$ causes the failure. In addition, all the Iridium satellites are in a Walker constellation, and they have nearly the same inclinations. However, the author tested all other Iridium debris and satellites to confirm whether the high inclination is the reason for the failure.

Iridium 33, NORAD id 35078, is a debris. Its inclination, semi-major axis, and B^* values are very close to what Iridium 68, NORAD id 25291, has. Iridium 33, NORAD id 35078, was propagated from 03-01-2013 to 03-08-2013 in order to check whether the air drag effect is the reason for the failure. However, the residuals are identical to the residuals that Iridium 68 yielded during the fitting process. Therefore, it has been concluded that its inclination of $8.6399100e + 01°$ causes the failure. Moreover, there are 4 other Iridium 33 debris which have approximately the same inclinations. Thus, all Iridium 33 debris in Table 13 fail due to their high inclinations.

Meteor 1-21, NORAD id 7714, is an operational weather satellite. Its period is $6.1373891e + 03$ seconds, which is in the close vicinity of the 14:1 resonance. It was propagated from 09-02-2013 to 09-08-2013. It yielded residuals on the order of hundreds of meters during the fitting process although the convergence was accomplished. Because the fit was converged,

Table 13. 34 Test Cases Failed for the Second Time

NORAD id	Satellite Name	Type	Launch Date
25291	IRIDIUM 68	PAYLOAD	1998-04-07
35078	IRIDIUM 33	DEBRIS	1997-09-14
7714	METEOR 1-21	PAYLOAD	1975-04-01
29349	KOREASAT 5	PAYLOAD	2006-08-22
25531	IRIDIUM 83	PAYLOAD	1998-11-06
26599	BEIDOU 1	PAYLOAD	2000-10-30
34356	IRIDIUM 33	DEBRIS	1997-09-14
16495	COSMOS 1726	PAYLOAD	1986-01-17
33697	FENGYUN 1C	DEBRIS	1999-05-10
9701	DELTA 1	DEBRIS	1973-11-06
21153	SL-8 R/B	ROCKET BODY	1991-03-12
24115	PEGASUS	DEBRIS	1994-05-19
23092	COSMOS 2279	PAYLOAD	1994-04-26
31039	FENGYUN 1C	DEBRIS	1999-05-10
15308	GALAXY 3	PAYLOAD	1984-09-21
28923	FREGAT R/B	ROCKET BODY	1991-03-12
31988	FENGYUN 1C	DEBRIS	1999-05-10
34928	IRIDIUM 33	DEBRIS	1997-09-14
30760	FENGYUN 1C	DEBRIS	1999-05-10
31561	FENGYUN 1C	DEBRIS	1999-05-10
29830	FENGYUN 1C	DEBRIS	1999-05-10
31339	FENGYUN 1C	DEBRIS	1999-05-10
33605	FENGYUN 1C	DEBRIS	1999-05-10
29921	FENGYUN 1C	DEBRIS	1999-05-10
20061	NAVSTAR 14	PAYLOAD	1989-06-10
7560	SL-8 DEB	DEBRIS	1972-08-16
36482	IRIDIUM 33	DEBRIS	1997-09-14
13073	COSMOS 1275	DEBRIS	1981-06-04
24435	EXPRESS 2	PAYLOAD	1996-09-26
21782	COSMOS 2168	PAYLOAD	1991-11-12
14966	SL-8 R/B	ROCKET BODY	1984-05-11
35981	COSMOS 2251	DEBRIS	1993-06-16
34488	IRIDIUM 33	DEBRIS	1997-09-14
23404	COSMOS 2297	PAYLOAD	1994-11-24

it was propagated for some random dates over 5 days in order to observe an improvement in the residuals. However, the residuals appeared to be poor for all attempts. Its semi-major axis and B^* values can't cause such poor fits. Therefore, it is concluded that the resonance is the reason for the poor residuals. The KAM torus might deform rapidly near the resonant orbits if not fail completely.

Koreasat 5, NORAD id 29349, is an operational satellite. It was propagated from 05-01-2013 to 05-10-2013 and from 07-01-2013 to 07-08-2013 in order to check whether the third body mass perturbations lead to the failure. Both propagations yielded the same big residuals during the fitting process. Its period is $8.6165984e + 04$ seconds, and it is in the close vicinity of the 1:1 resonance. Therefore, it is concluded that the resonance is the reason for the failure.

Iridium 83, NORAD id 25531, is an operational satellite. It was propagated from 02-01-2013 to 02-08-2013. The fitting process yielded characteristic polar inclination residuals, which were on the order of 10^7 km. Therefore, it is concluded that high inclination, which is $8.6396500e + 01°$, is the reason for the failure.

Beidou 1, NORAD id 26599, is an operational satellite. It was propagated from 01-01-2013 to 01-10-2013 and from 09-01-2013 to 09-10-2013. Both least squares fits yielded big residuals, and the convergence failed for both attempts. The resonance might be the reason for the failure because its period is $8.7352213e + 04$ seconds.

Cosmos 1726, NORAD id 16495, is an operational satellite. It was propagated from 01-01-2014 to 01-14-2014. It has an altitude of 527 km, and a B^* value of $3.4805000e - 04$. The orbit was successfully fitted to SGP4 and TLE with an rms value of 7.54832 km over 13 days. The poor fit shows that the atmospheric model used in the program, which is based on the U.S. Standard Atmosphere, should be improved to predict satellites with low altitudes with better accuracy. Figure 23 represents the plots for position and velocity residuals. In the plot, along-track residuals are relatively bigger than the other components,
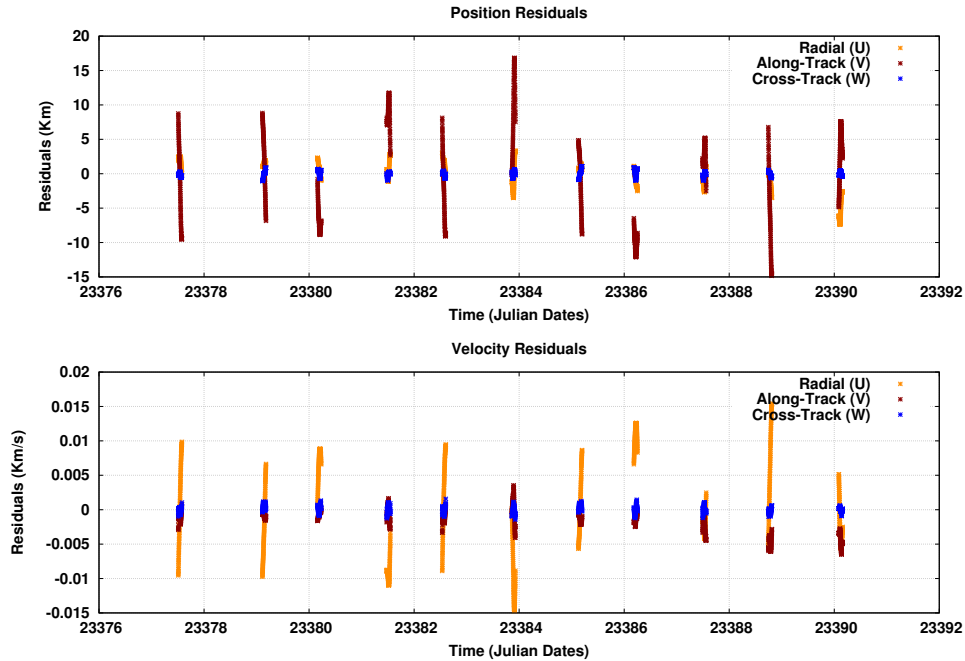
Figure 23. The Residuals for Cosmos 1726 over 13 days

which proves that the air drag effect is the reason for the failure of the first attempt.

Fengyun 1C debris, NORAD id 33697, 31988, 30760, 31561, 31339, 33605, and 29921, are in the close vicinity of the 14:1 resonance. Each debris was propagated for a short period of time in order to figure out whether the air drag effect is the reason for the failure. None of the fits converged. Therefore, the reason for the failure is the 14:1 resonance. Moreover, Fengyun 1C debris, NORAD id 31039, and 29830, prove this statement because although two of them have lower height and higher B^* value, both fits converged, and the residuals weren't bad for their low altitude. Fengyun 1C debris, NORAD id 29830, yields an rms value of 9.47329 km, and NORAD id 31039 yields an rms value of 22.8057 km. Figure 24 represents the plot for position and velocity residuals of Fengyun 1C debris, NORAD id 29830, and Figure 25 shows the plot for position and velocity residuals of Fengyun 1C debris, NORAD id 31039. In the plots, the quadratic characteristic of air drag effect can be easily seen.

Delta 1 debris, NORAD id 9701, has relatively high B^* value, which is $1.2101000e-$
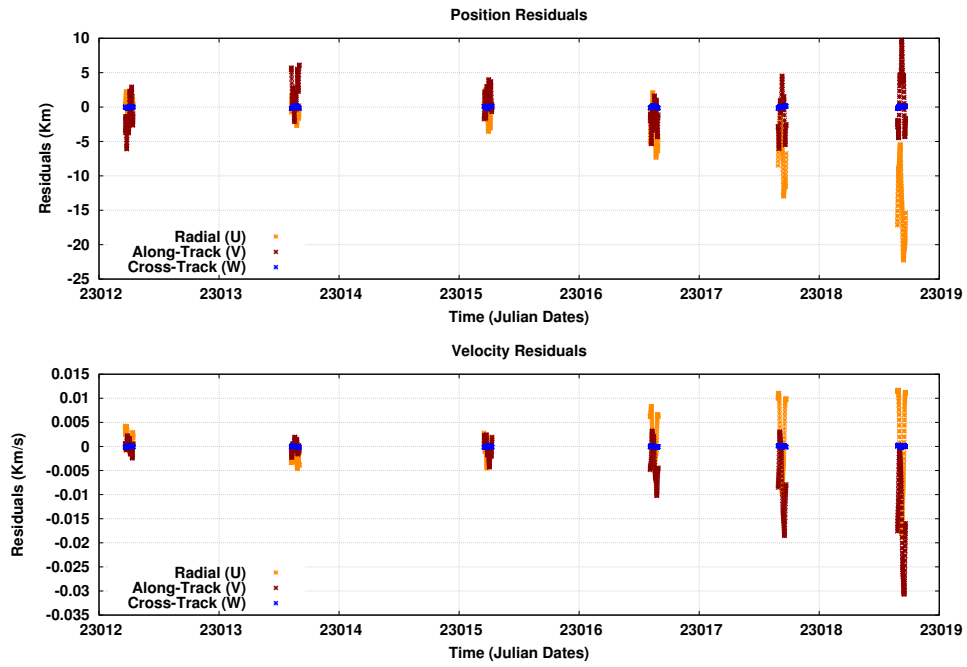
Figure 24. The Residuals for Fengyun 1C, NORAD id 29830, over 6 Days
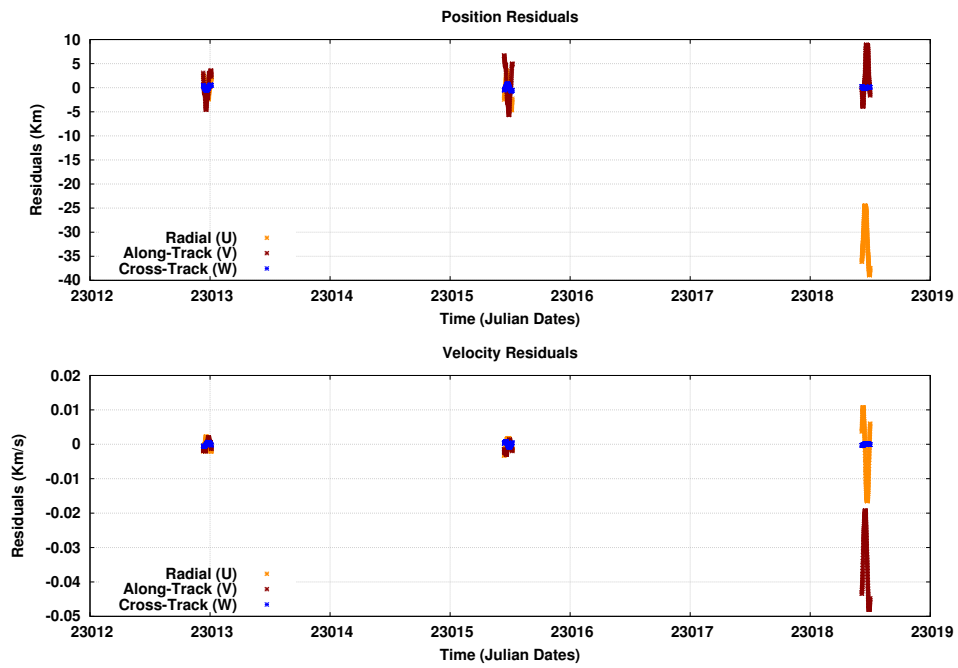
Figure 25. The Residuals for Fengyun 1C, NORAD id 31039, over 6 Days

89

02, and it is also in the close vicinity of the 13:1 resonance. It was propagated from 01-01-2014 to 01-09-2014. The least squares fit converged with an rms value of 94 km over 8 days.Therefore, the air drag effect is believed to be the prime reason for the failure.

SL-8 R/B, NORAD id 21153, is a rocket body. It has an inclination of $8.2926500e+01°$, a semi-major axis of $7.3573300e+03$ km, a B^* value of $1.3800000e-04$, and a period of $6.2804555e+03$ seconds. It was propagated from 01-02-2014 to 01-08-2014. The least squares fitting process converged with an rms value of 47.0068 km. Thus, the air drag is the reason for the failure. Figure 26 represents the plot for position and velocity residuals.
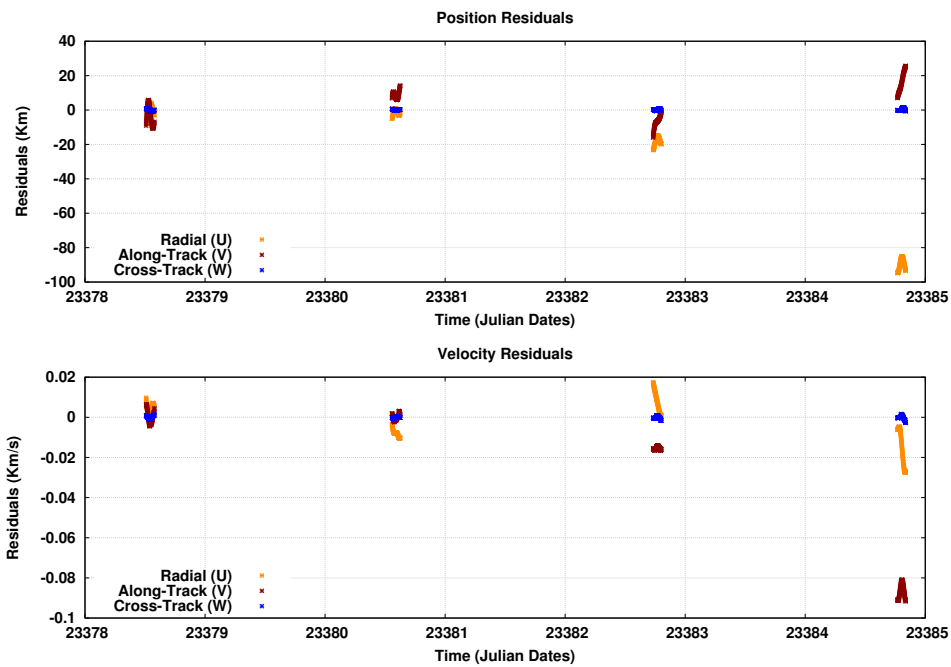
Figure 26. The Residuals for SL-8 R/B, NORAD id 21153, over 10 Days

Pegasus, NORAD id 24115, is a debris. Its relatively low altitude, which is 512.275 km, and relatively high B^* value, which is $6.3281000e-04$, are responsible for the failure because the least squares fit converged when it was propagated from 01-02-2014 to 01-09-2014 over 8 days. Figure 27 represents the plot for position and velocity residuals.

Cosmos 2279, NORAD id 23092, is an operational satellite. It was propagated from

90
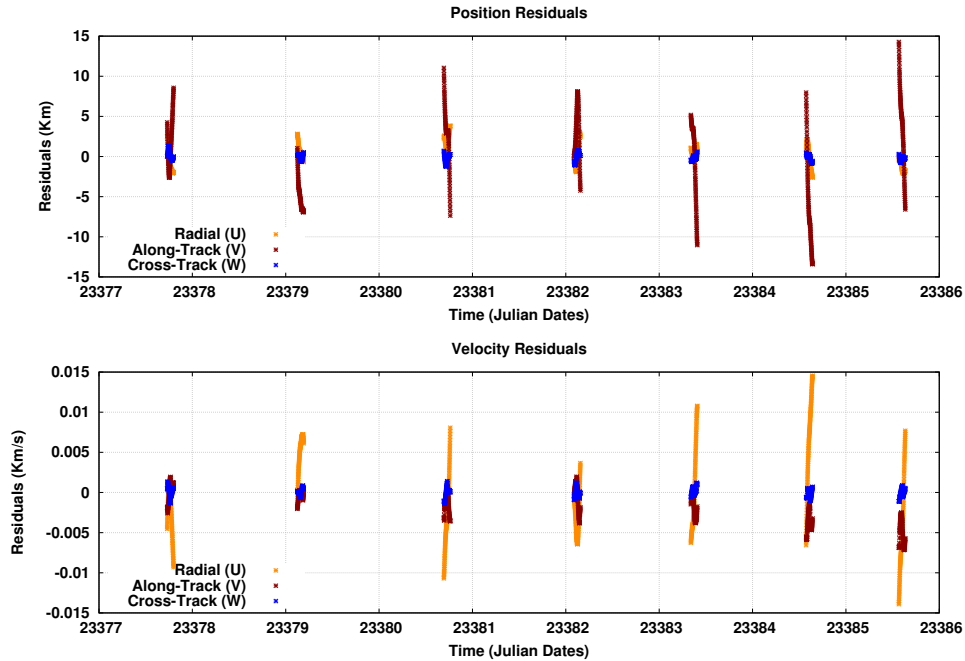
Figure 27. The Residuals for Pegasus, NORAD id 24115, over 9 Days

01-01-2014 to 01-19-2014. The least squares fit converged with an rms value of 13.8748 km over 18 days. Therefore, it is clear that the least squares fit has failed to converge due to the air drag effect. Figure 28 represents the plot for position and velocity residuals.

Galaxy 3, NORAD id 15308, is an operational satellite with a period of 24.03. The propagation from 01-01-2014 to 01-10-2014 yielded an rms value of 1.94622 km. Therefore, the inaccuracies in the TLEs caused the failure.

Fregat R/B, NORAD id 28923, is a rocket body. It has an inclination of $5.6419100e+01°$, a semi-major axis of $2.9813700e+04$ km, and a period of $5.1231209e+04$ seconds. It was propagated for different time periods, and all attempts yielded characteristic rms values for resonant orbits, which were approximately on the order of 10^6, and the residuals were random-like. Therefore, it is concluded that the resonance is the reason for the failure.

Navstar 14, NORAD id 20061, is an operational satellite. It has an inclination of $5.5107800e+01°$, a semi-major axis of $2.7647000e+04$ km, and a period of $4.5749126e+04$ seconds. It was propagated from 01-01-2014 to 01-10-2014. The least squares fitting
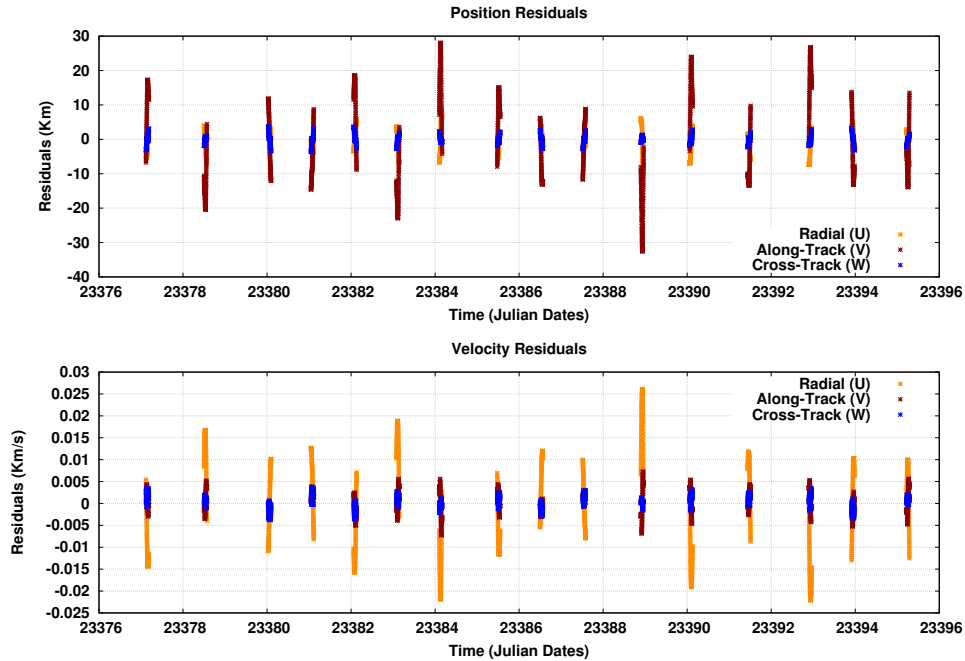
Figure 28. The Residuals for Cosmos 2279, NORAD id 23092, over 18 Days

process yielded random big rms values for iterations, which were on the order of 10^{-6}. Therefore, it is concluded that the resonance is the reason for the failure.

SL-8 debris, NORAD id 7560, has a period of $6.1487649e+03$ seconds. Thus, it is in the close vicinity of the 14:1 resonance. It was propagated from 01-01-2014 to 01-10-2014. The least squares fit failed to converge, and yielded random big rms values for iterations, which is typical residuals for orbits in the close vicinity of the resonance.

Cosmos 1275, NORAD id 13073, is a debris. It was propagated from 01-02-2014 to 01-09-2014. The convergence was accomplished with an rms value of 3.39862 km. Therefore, the reason for the failure is the air drag effect. Figure 29 represents the plots for position and velocity residuals over 7 days.

Express 2, NORAD id 24435, is an operational satellite. It has an inclination of $1.2856800e+01°$, a semi-major axis of $4.2182300e+04$ km, and a period of $8.6219633e+04$ seconds. It is in the close vicinity of the 1:1 resonance. Express 2 was propagated from 01-03-2014 to 01-08-2014 over 5 days. It yielded random big rms values during the least
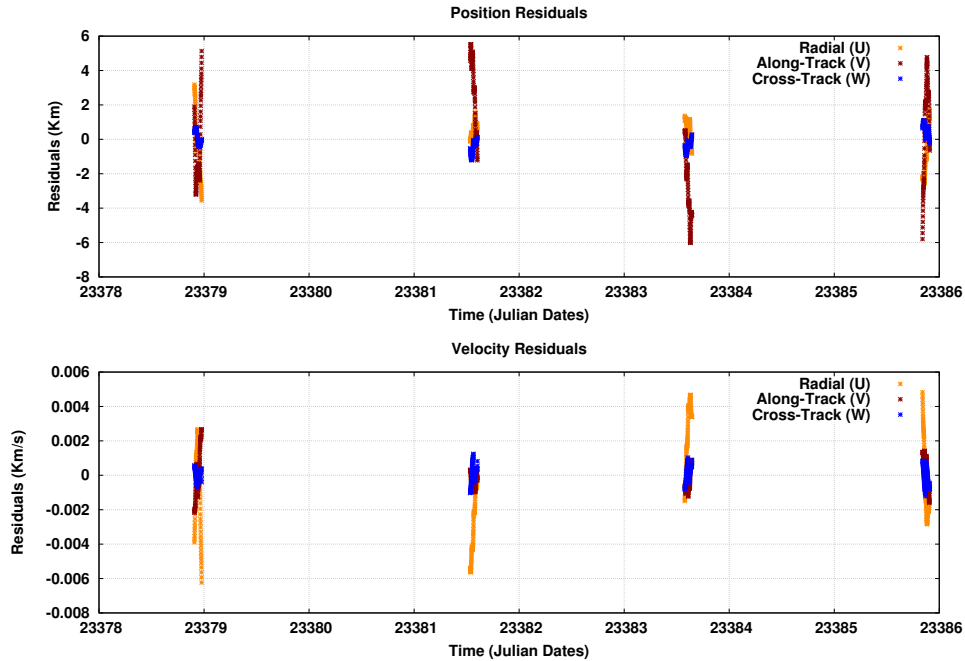
Figure 29. The Residuals for Cosmos 1275, NORAD id 13073, over 7 Days

squares fitting process, and it failed to converge. Therefore, the resonance is the reason for the failure not the third body mass perturbations.

Cosmos 2168, NORAD id 21782, is an operational satellite. It has an inclination of $8.2598100e+01°$, a semi-major axis of $7.7788100e+03$ km, a B^* value of $2.4820000e-04$, and a period of $6.8277959e+03$ seconds. It was propagated from 01-02-2014 to 01-09-2014 over 7 days. The least squares fit converged with an rms value of 2.11935 km. Therefore, it is concluded that the reason for the failure is the air drag effect. Figure 30 represents the plots for position and velocity residuals over 7 days.

SL-8 R/B, NORAD id 14966, has an inclination of $8.2972500e+01°$, a semi-major axis of $7.3620200e+03$ km, a B^* value of $1.9141000e-04$, and a period of $6.2864617e+03$ seconds. It was propagated from 01-01-2014 to 01-09-2014 over 9 days. The least squares fit converged with an rms value of 13.9352 km. Therefore, the air drag effect is the reason for the failure.

Cosmos 2251, NORAD id 35981, has an inclination of $7.4059500e+01°$, a semi-major
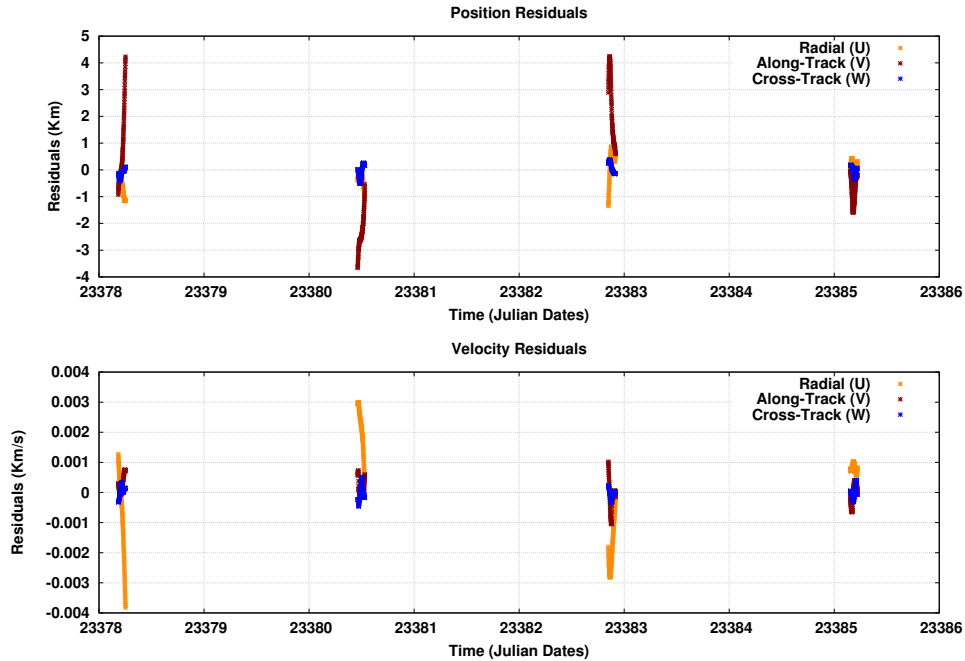
Figure 30. The Residuals for Cosmos 2168, NORAD id 21782, over 9 Days

axis of $6.9195900e+03$ km, a B^* value of $2.9060000e-03$, and a period of $5.7283735e+$ 03 seconds. It was propagated from 01-01-2013 to 01-14-2013 over 13 days. The least squares fit converged with an rms value of 86.645 km, which isn't surprising because of its low altitude and high B^* value. Therefore, the air drag effect is the reason for the failure. Figure 31 represents the plots for position and velocity residuals over 15 days.

Cosmos 2297, NORAD id 23404, is in the close vicinity of the 14:1 resonance. It has an inclination of $7.1013200e+01°$, a semi-major axis of $7.2261100e+03$ km, a B^* value of $2.4820000e-04$, and a period of $6.1131864e+03$ seconds. It was propagated from 01-01-2014 to 01-15-2014, 01-09-2014, and 01-07-2014 for three different time periods. All attempts failed because of the resonance.

In conclusion, 1500 test cases, which fit the conditions mentioned in Section 3.1, were propagated using the low eccentricity KAM torus method. Then, each KAM torus propagation data was fitted to SGP4 and TLE prediction data associated with each test case over 2 months. Initial success rate for convergence is 56.8667%. Then, 100 new test cases were
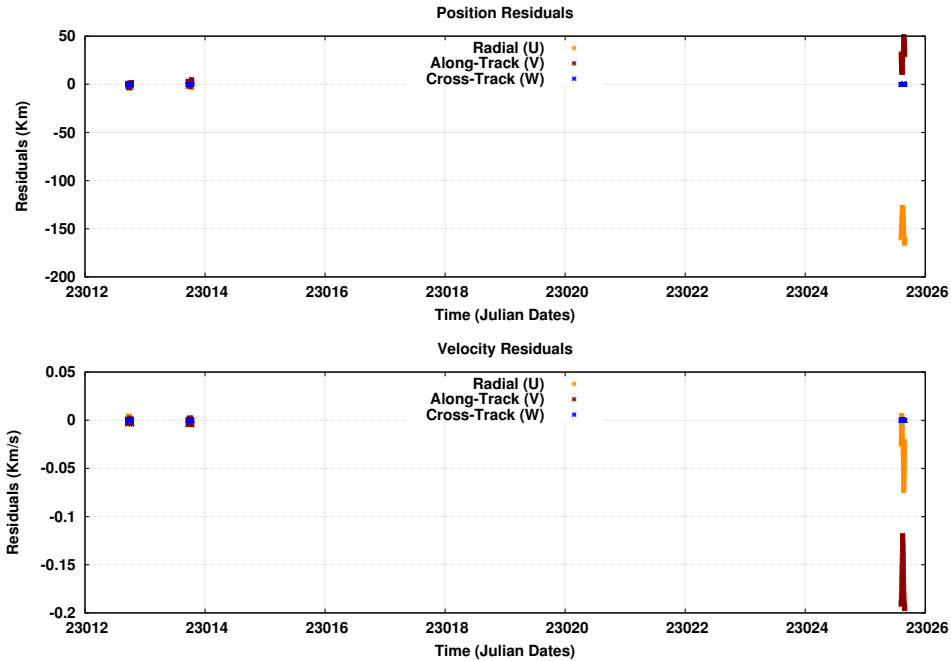
Figure 31. The Residuals for Cosmos 2251, NORAD id 35981, over 15 Days

selected from the failed test cases, and the same process was applied to 100 new test cases. The success rate of least squares fitting over 20 days instead of 2 months for the new test cases is 66%. Next, 34 failed test cases, which failed to converge for the second time, were individually analyzed. Seven test cases failed for the third time because their inclinations are in the close vicinity of polar inclination. An inclination of $86°$ caused the construction of the KAM torus to fail. The unstable forms of the Legendre polynomial recursions for the calculation of geopotential caused the high eccentricity problem. The solution is left for future studies. One test case failed to converge to the SGP4 and TLE data because of the inaccuracies in the TLEs. Ten test cases failed due to the air drag effect. Test cases with relatively high B^* value and low altitude can only be propagated for short period of time because of effective air drag. Sixteen test cases failed to converge due to the resonance. There is no KAM torus near the resonance. Therefore, a clever approach should be taken to deal with the resonance, which is important for the generalization of the theory to all orbits. In addition, critical and polar inclination problems should also be addressed for the

95

generalization of the theory.

4.2　Orbital Characteristics and Residuals

The relationship between some orbital characteristics, such as semi-major axis, eccentricity, inclination, B^* value, and period, and rms values yield valuable information about the theory. Because many factors degrade the accuracy and the dimensions that can be used to present the data are restricted to 3, straightforward presentation of data isn't useful. Therefore, success ratio, which is successful attempts over the sum of the successful and failed attempts, for fixed time intervals versus orbital characteristics are used for the plots. The time intervals vary based on the orbital characteristics. However, there are 30 time intervals for all orbital characteristics. Each success ratio is an average value for a time interval, which is attributed to the starting point of the interval. This is important information for evaluating the plots including resonance data because the effects of the resonance don't seem to be aligned. Therefore, additional explanations are provided for the plots. The data obtained from 1500 test cases were used for all plots in Section 4.1.

The success ratio versus semi-major axis was plotted for LEO and GEO satellites because there were few test cases at the MEO altitudes. For LEO satellites, the prime perturbation that degrades the accuracy for the theory is the air drag. The other parameter that degrades the accuracy for LEO satellites is the resonance. For GEO satellites, the prime perturbation is the third body mass. The other parameter that degrades the accuracy for GEO satellites is the 1:1 resonance.

Figure 32 represents the success ratio versus semi-major axis for the test cases which have semi-major axes of 8000 km and smaller. The resonance points from left to right are the 29:2, 14:1, 27:2, 13:1, 37:3, and 12:1 resonances. Although 29:2 and 37:3 resonances do seem to be aligned with the decrease in the success ratio, the success ratio is an average over a time interval attributed to the starting point of the interval. For the 29:2 resonance

96

case, the success ratio average is from 7050 km to 7100 km, and the altitude, which is calculated from the center of Earth, for the 29:2 resonance is 7090.846 km for orbits with zero eccentricities. For the 37:3 resonance case, the success ratio average is from 7850 km to 7900 km, and the altitude, which is calculated from the center of Earth, for the 37:3 resonance is 7898.714 km for orbits with zero eccentricities. In addition, the 13:1 resonance doesn't degrade the accuracy to zero for the interval between 7600 km and 7700 km. There are missing data for the interval between 7600 km and 7650 km. However, the resonance certainly degrades the accuracy. The success ratio increases with increasing altitude, which isn't surprising, because air drag perturbation is more effective at low altitudes.
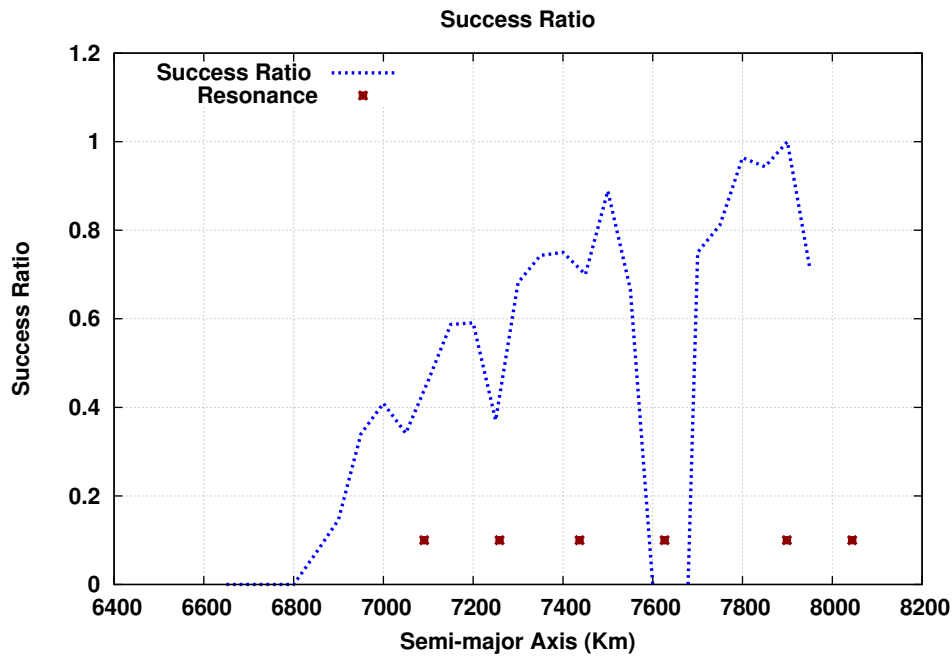
Figure 32. The Success Ratio versus Semi-Major Axis for LEO Objects over 2 Months

The plot for the success ratio of GEO objects is surprising at the first glimpse because there are unexpected failures. Further examination yielded that three test cases created these failures. The author propagated these three test cases, which are Ius R/B, NORAD id 22316, Tvsat 2, NORAD id 20168, and familiar Galaxy 3, NORAD id 15308, from 01-01-2014 to 03-01-2014. They converged with rms values of 13.3379 km, 10.1593 km,

97

and 14.4785 km, respectively, which proves that many failures can be related to the inaccuracies in TLEs, but this effort ignores this fact. Figure 33 represents the success ratio for test cases which have a semi-major axis between 42100 km and 42500 km before and after corrections are applied. The accuracy decreases rapidly after 42316 km. The convergence totally vanishes, or the accuracy becomes extremely low if the convergence is accomplished for 42416 km and bigger semi-major axis values due to the third body mass perturbations. The 1:1 resonance certainly degrades the accuracy. In addition, active payloads in geosynchronous orbit are maneuvered frequently to suppress the action of the resonance.
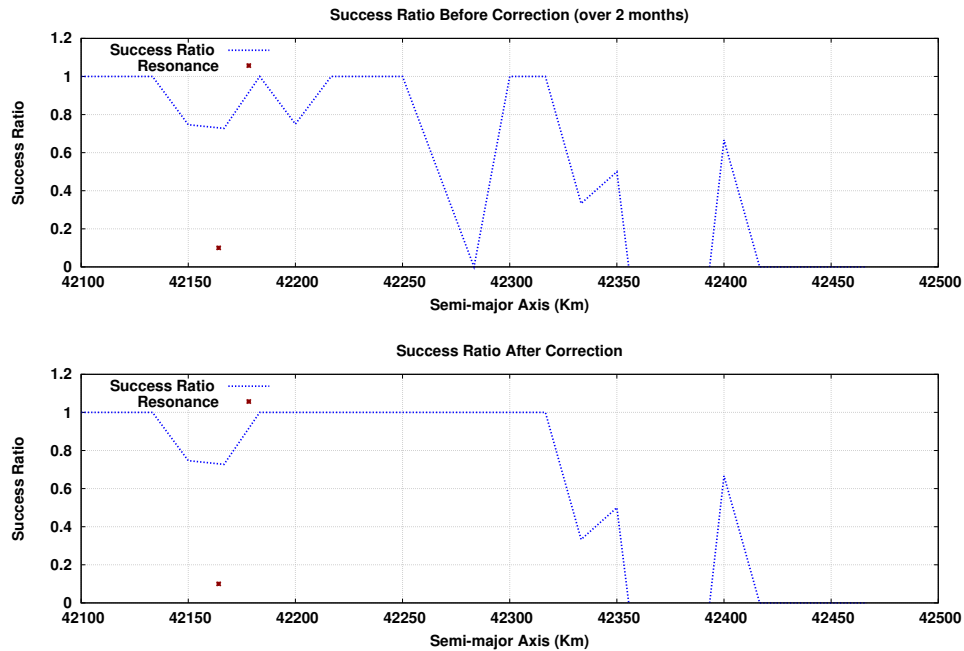
Figure 33. The Success Ratio versus Semi-Major Axis for GEO Objects

Figure 34 represents the success ratio versus eccentricity for the test cases which have eccentricities between 0 and 0.01. In the plot, from 0 to 0.004 the accuracy is pretty leveled, except some ups and downs due to other orbital characteristics. However, after the threshold of 0.004 eccentricity is passed the success ratio decreases to approximately 30%. This proves how eccentricity is an important factor in terms of accuracy for the theory. Moreover, another analysis in Section 4.4 will examine the upper limit for the eccentricity

that can be modeled by the theory.
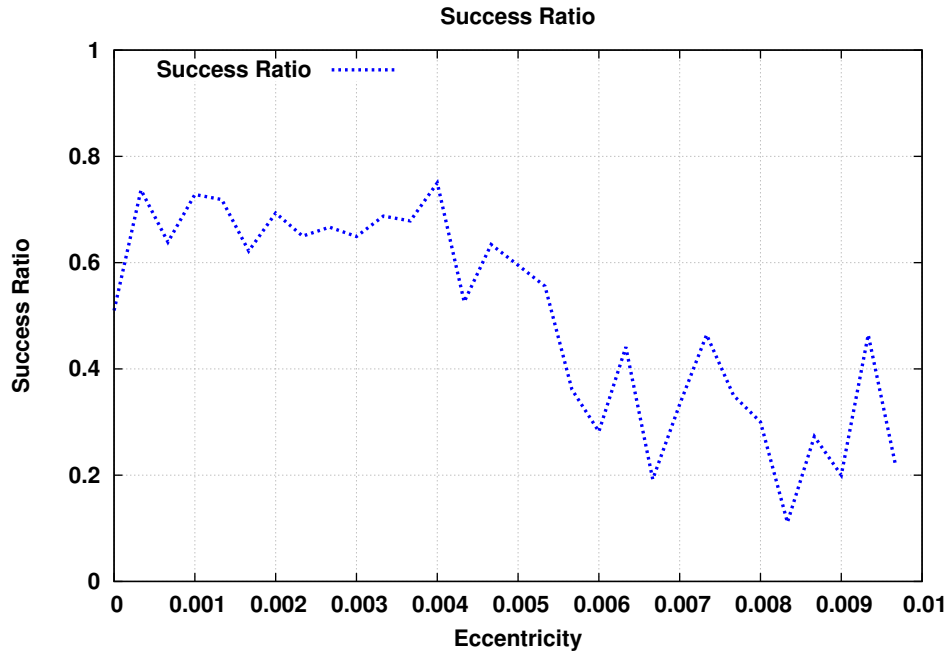
Figure 34. The Success Ratio versus Eccentricity over 2 Months

Figure 35 represents the success ratio versus B^* for the test cases which have B^* values between 0 and 0.01. In the plot, when the B^* value of 0.003 is passed the success ratio for convergence decreases to approximately zero. The sharp decrease with increasing B^* value shows the importance of the value for the theory. As mentioned previously, the B^* value defines the susceptibility of near-Earth objects to air drag. The more effective the air drag is on a near-Earth object, the less accurate low eccentricity KAM torus theory becomes. The drastic effect of the B^* value on the theory necessitates either an improved atmospheric model or the shorter propagation time interval. However, the first option may not introduce enough improvement in the accuracy due to the stochastic nature of air drag. One thousand five hundred test cases were pseudo-randomly selected under the conditions mentioned in details in Section 3.1, which include the close vicinity of polar and critical inclination, and eccentricity on the order of 10^{-3} and smaller. Figure 36 represents the success ratio versus inclination in order to check whether there are other inclination values
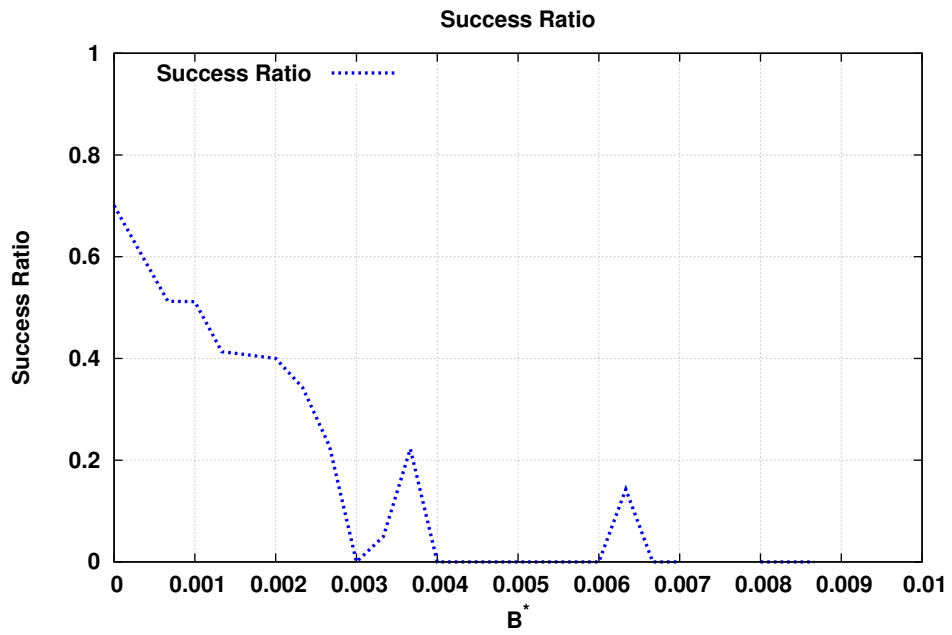
**Figure 35. The Success Ratio versus Bstar over 2 Months**
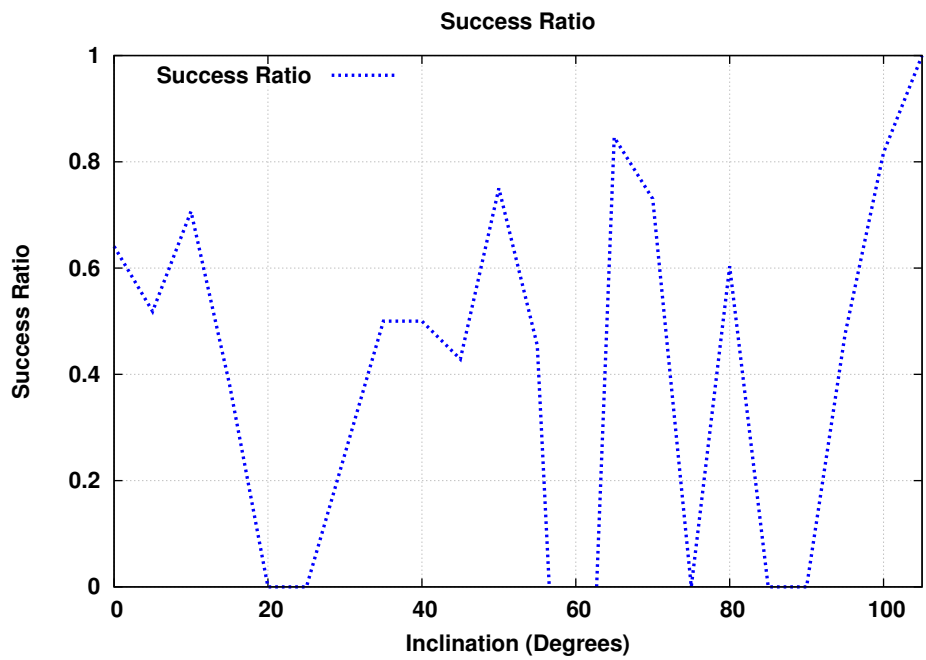
Figure 36. The Success Ratio versus Inclination over 2 Months

100

that lead to the resonance. In the plot, the inclinations of $20°$ and $80°$ seem to decrease the accuracy drastically, but this is an unexpected situation. Further examination yielded that three test cases for inclinations between $20°$ and $25°$, two test cases for inclinations between $25°$ and $30°$, and three test cases for inclinations between $75°$ and $80°$ have created these failures. For inclinations $20°$-$25°$, Delta 2 rocket body, NORAD id 21931, Pegasus rocket body, NORAD id 22491, and Scd 2, NORAD id 25504, have caused the failures. They all have low altitudes. Delta 2 R/B was propagated from 01-01-2013 to 01-10-2013, and the other two were propagated from 01-01-2014 to 01-10-2014. They converged to the SGP4 and TLE data with rms values of 15.2938 km, 0.3447 km, and 0.2793 km, respectively. For inclinations $25°$-$30°$, Tansei 1, NORAD id 4952, Delta 1 debris, NORAD id 10309, and Galex, NORAD id 27783, caused the failures. Delta 1 and Galex have low altitudes. Two of them were propagated from 01-01-2014 to 01-10-2014 with rms values of 269.943 km, 0.2481 km, respectively. Although Delta 1 successfully converged, its semi-major axis, which is 6849.32, caused a big residual. Tansei 1 was also propagated from from 01-01-2014 to 01-10-2014 in order to check whether attitude control, or station keeping maneuvers caused the failure. It was converged with an rms value of 0.5388 km. For inclinations $75°$-$80°$, Scout X-4, NORAD id 871, and SL-21 rocket body, NORAD id 29159, caused the failures. Two of them were propagated from 01-01-2014 to 01-10-2014 with rms values of 0.9033 km, and 24.7307 km, respectively. Therefore, the polar and the critical inclinations are the only ones that fail the converge and degrade accuracy. The success ratio is quite leveled if the corrections are applied. Thus, there is no linear relation between the success ratio and the inclination. Moreover, another analysis in Section 4.4 will examine the limits for the polar and critical inclinations that can be modeled by the theory.

Figure 37 represents the success ratio versus the period for the test cases which have periods between 6000 seconds and 7160 seconds. The resonance points from left to right

are the 14:1, 13:1, and 12:1. The other order resonances, such as 27:2 and 37:3, can't be detected in the plot. The two drastic decreases between 6400 seconds and 6600 seconds are due to the small number of test cases which all except one have high B^* values. One of them failed to converge due to the inaccurate TLEs. For periods between 6440 seconds and 6480 seconds, Delta 1 rocket body, NORAD id 21602, and Nimbus 2 debris, NORAD id 31579, reduced the accuracy. For periods between 6520 seconds and 6560 seconds, Cosmos 770, NORAD id 8325, which has a B^* value of 2.845×10^{-3}, Meteor 3-2, NORAD is 19336, which has a B^* value of 1.1514×10^{-3}, Cosmos 1275 debris, NORAD id 14440, which has a B^* value of 1.4665×10^{-2}, and SL-8 rocket body, NORAD id 11170, which failed due to the inaccurate TLEs because propagation from 01-01-2002 to 03-01-2002 yielded 16.7697 km residual. Because there are few test cases between 6400 seconds and 6600 seconds, the resonance effect can't be detected during this time period. Therefore, if the propagation time is decreased, the success ratio between 6400 seconds and 6600 seconds has a very similar trend as the success ratio between 6200 seconds and 6400 seconds, that is a linear increase with smaller variations.

In conclusion, the resonance has emerged as a problem again in the broader picture. This section presents the analysis for 1500 test cases. For LEO objects, air drag degrades the success ratio of the least squares fit over 2 months to zero for altitudes below 422 km. The accuracy also increases with increasing altitude. For GEO satellites, third body mass perturbation degrades the success ratio of the fit to zero for altitudes above 36038 km. The only resonance that effects the accuracy is the 1:1 resonance for altitudes between 35622 km and 36122 km. The eccentricity has appeared as an important parameter that degrades the accuracy. A sharp decrease in the accuracy occurs for eccentricities bigger than 0.004. The B^* value has drastically decreased the accuracy of the theory. Moreover, all 16 test cases between the interval 0.0030 and 0.0033 have failed to converge. Therefore, the upper limit for B^* for the theory can be defined as 0.003. However, the success rate for
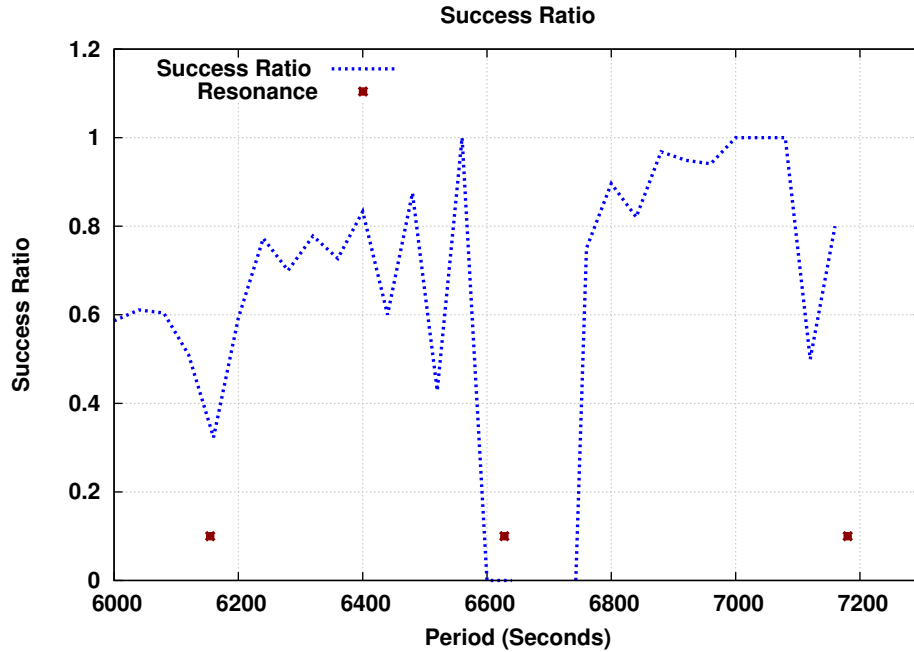
Figure 37. The Success Ratio versus Period over 2 Months

B^* values between 0 and 0.001 can be easily enhanced by an improved atmospheric model. For the current theory, 217 out of 725 test cases have failed for the B^* values between 0 and 0.00033. The polar inclination and the critical inclination were proved to be the only problem that terminates the convergence of the least squares fit. Thus, there are no other inclination values that lead to failure of the convergence of the least squares fit. Moreover, there is no linear relation between the success ratio and the inclination. The success ratio based on the period is unsurprisingly very similar to the success ratio based on the altitude. There is a linear relation between the period and the success ratio of the convergence of the least squares fit.

4.3   Some Samples from the Results

The general performance of the theory has been presented so far. This section introduces some characteristic examples of the least squares fits for the LEO and GEO objects. Every test case has a plot that represents the accuracy of the low eccentricity KAM torus

theory assuming that SGP4 and TLE data are raw observational data. The reference frame for the plots is RAN frame of reference, see Section 2.4. However, this isn't a fair evaluation of the accuracy of the theory because the basis frequencies and B^* are continuously updated using SGP4 and TLE data. Section 4.5 introduces a fair comparison between SGP4 and the low eccentricity KAM torus method in terms of accuracy. Therefore, the plots introduced in this section present whether the numerically built torus can be fitted to observational data. If the torus is fitted to the observational data with high accuracy, the result is a compact numerical set of algorithms that are as accurate as numerical methods and as fast as general perturbation techniques, in terms of computational time.
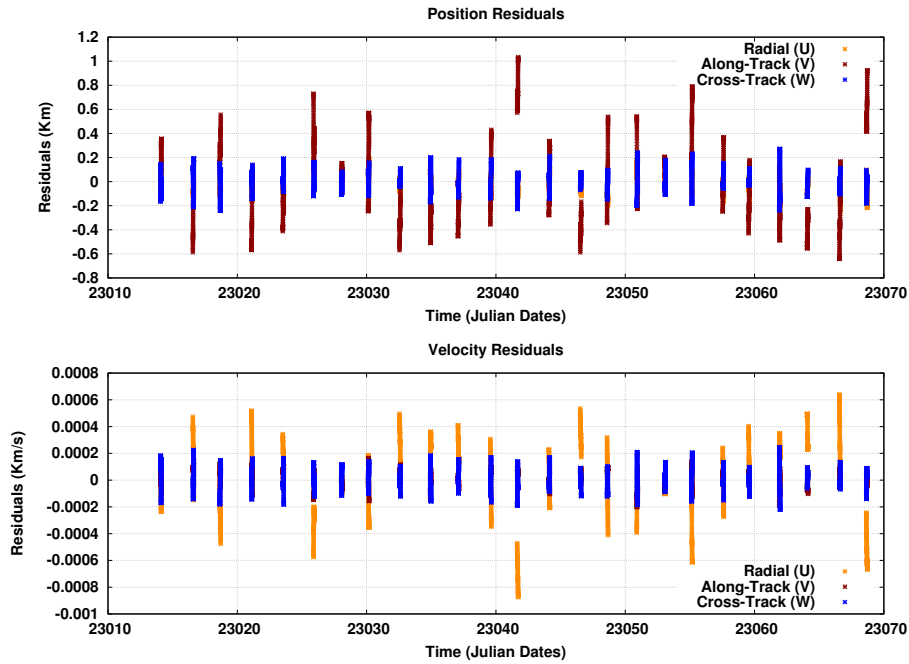
Figure 38. The Residuals for Thorad Delta 1 Debris, NORAD id 8168, over 2 Months

Figure 38 and Figure 39 represent the best 2 least squares fits for LEO objects. They are Thorad Delta 1 debris, NORAD is 8168, and Thorad Delta 1 debris, NORAD is 8140. The least squares fitting process yielded $3.6864262e - 01$ km and $4.2330236e - 01$ km, respectively. Although both of them have similar orbital characteristics, the difference in the accuracy is due to the B^* values, which are $8.2174000e - 05$ and $9.3318000e -$
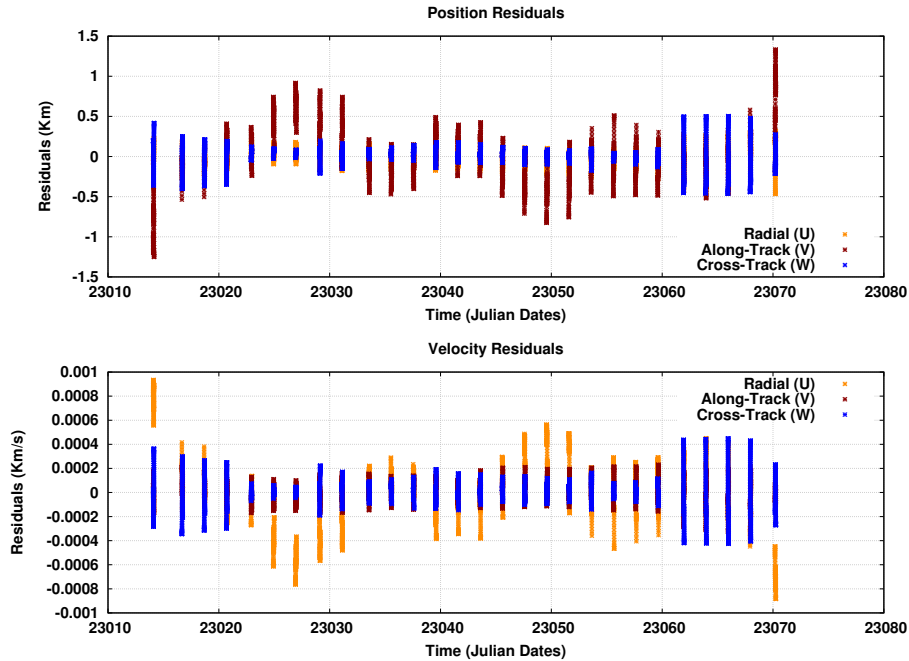
Figure 39. The Residuals for Thorad Delta 1 Debris, NORAD id 8140, over 2 Months

05, respectively. It should be also noted that Thorad Delta 1 debris, NORAD is 8140, is approximately at an altitude 25 km higher than Thorad Delta 1 debris, NORAD is 8168. Both plots present the bounded oscillatory behavior of the residuals over 2 months. They both have an altitude slightly above 1450 km. Thus, air drag isn't that effective, and the quadratic structure of air drag usually appeared on along-track and radial components can't be detected in the plots.

Ops 6630 debris, NORAD id 9323, Cosmos 2251 debris, NORAD id 35469, and Thorad Agena D debris, NORAD id 4214, have least squares fits with residuals on the order of kilometers due to different reasons. Figure 40 represents the position and the velocity residuals of Ops 6630 debris for the least squares fit. Ops 6630 debris, NORAD id 9323, has an inclination of $9.7031200e+01$, a semi-major axis of $7.8056200e+03$, a B^* value of $2.5971000e-04$, and a period of $6.8631247e+03$ seconds. Its relatively high B^* value leads to a residual of 5.02942 km over 2 months. However, the familiar quadratic structure of air drag that appears on the along-track and the radial components can't be detected in
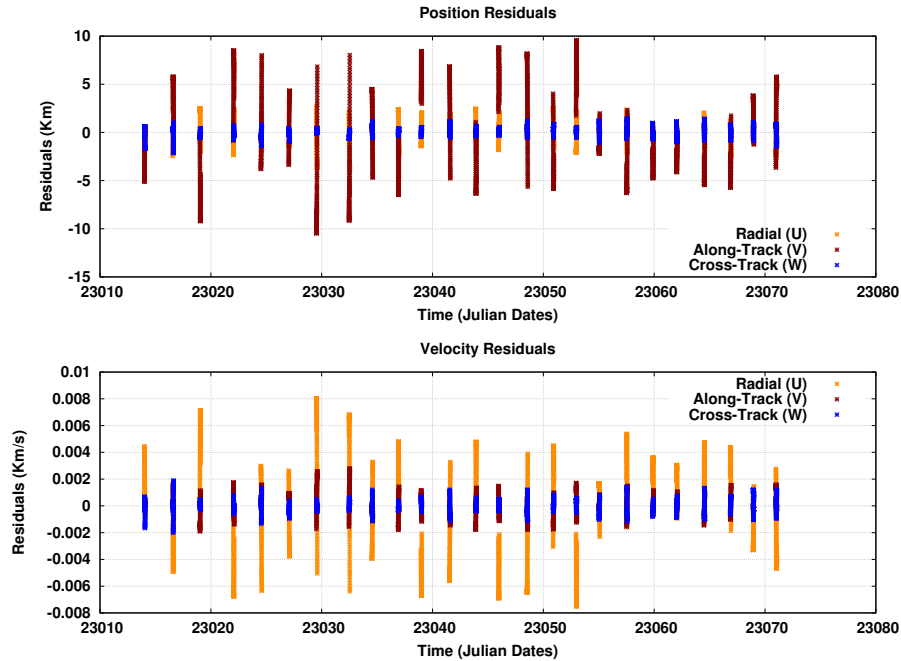
Figure 40. The Residuals for Ops 6630 Debris, NORAD id 9323, over 2 Months

the plot because its B^* value doesn't exceed the limit that can be handled by the theory. However, Figure 41 represents the quadratic air drag effect on the least squares fit of Thorad Agena D debris. The along-track and the radial components seem to diverge from the desired oscillatory behavior of the residuals. Another factor that degrades the accuracy is the inaccuracies in the TLEs. Figure 42 represents the residuals of Cosmos 2251 debris for the least squares fit. In the plot, one of the TLEs is certainly inaccurate.

GEO satellites don't yield neat oscillatory behavior for the residuals because the third body mass perturbations aren't added to the theory yet. However, third body mass perturbations can be calculated like air drag perturbations, see Section 3.5. There will be at least one additional angle in the Fourier series to specify the motion of the Sun or the Moon. Three example test cases were chosen to present the characteristic fits for GEO satellites. Two of them have the best fits for GEO. The other one is one of the poorest fits. The poor fit proves the behavior of the residuals when the altitude of the satellite approaches to the threshold of 36000 km. Figure 43 represents the position and the velocity residuals of Ops

106
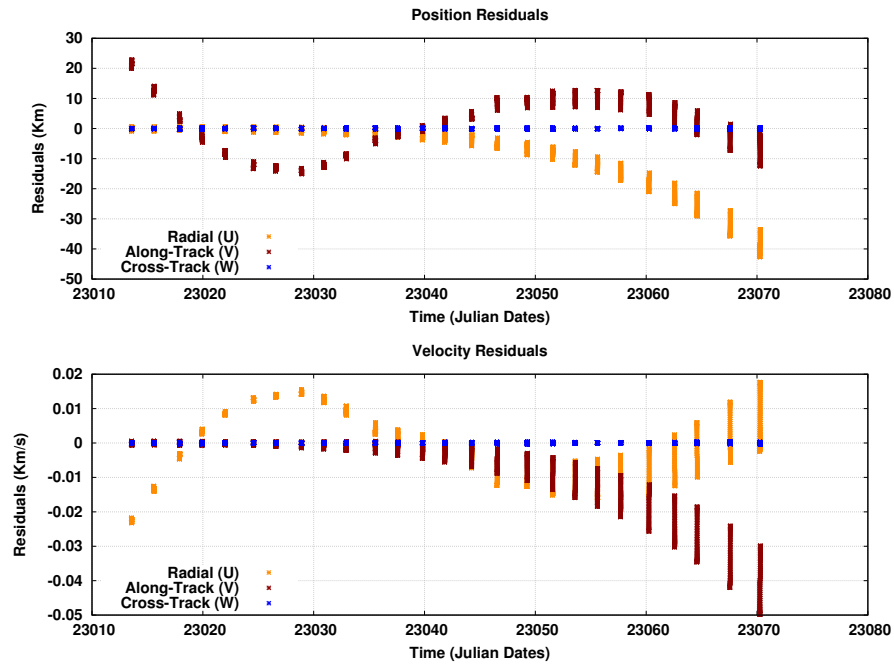
Figure 41. The Residuals for Thorad Agena D Debris, NORAD id 4214, over 2 Months
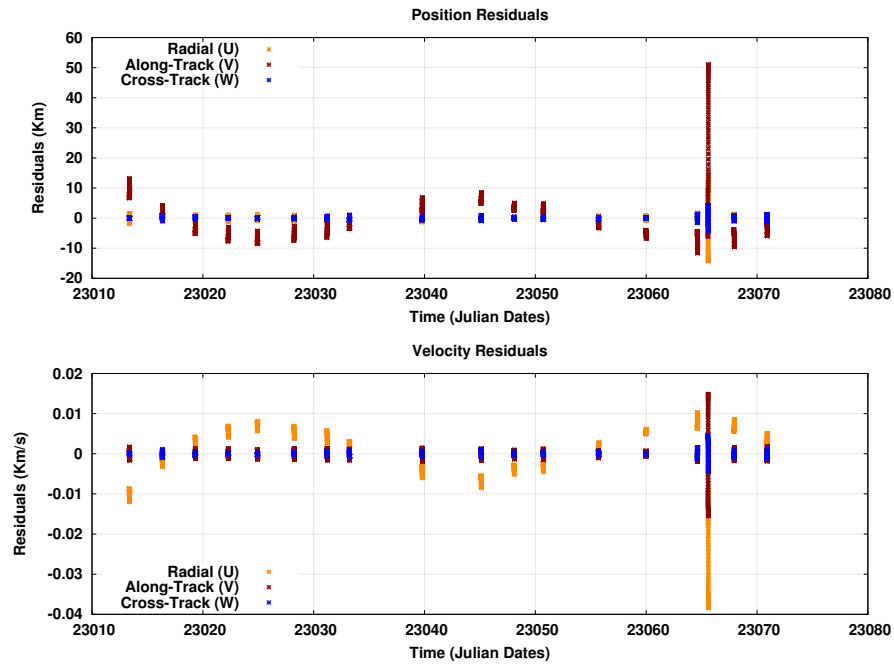

Figure 42. The Residuals for Cosmos 2251 Debris, NORAD id 35469, over 2 Months
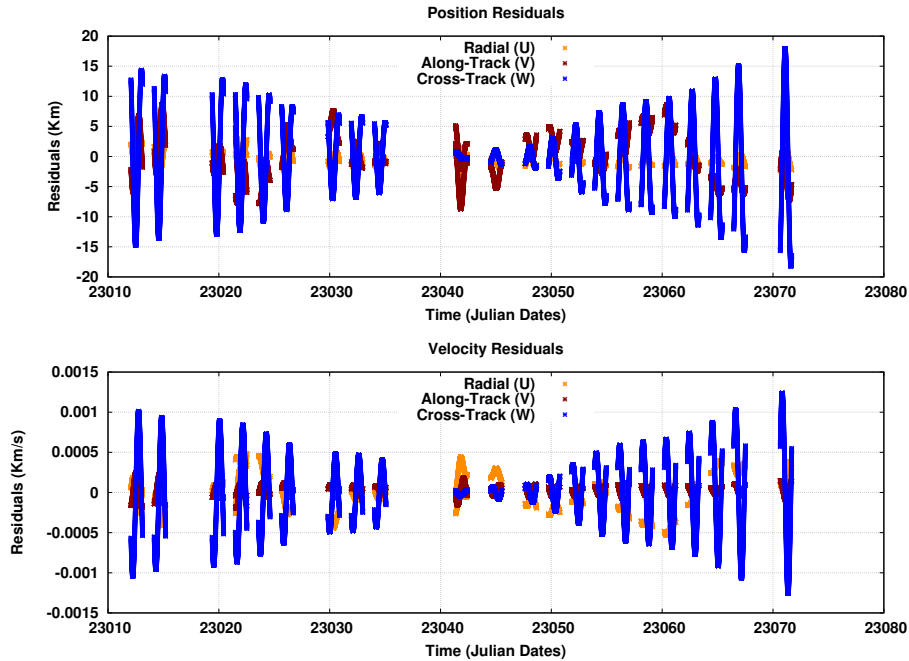
Figure 43. The Residuals for Ops 9443 payload, NORAD id 11621, over 2 Months

9443 payload, NORAD id 11621, for the least squares fit. The least squares fit for Ops 9443 payload was converged with an rms value of 8.4179 km. Although this fit is one of the best fits for GEO satellites, its accuracy is far worse than the best fit for LEO objects because objects at high altitudes change their orbits towards the ecliptic plane of the solar system. Therefore, the third body mass perturbations should be added to the theory for better accuracy for GEO satellites. Figure 44 represents the position and the velocity residuals of Ops 9438 payload, NORAD id 10001, for the least squares fit. There are irregular patterns in the plot. However, third body mass perturbations are not the only source of error. Both station keeping maneuvers and inaccurate TLEs can cause these irregular residuals as well. Intelsat 4-F3 payload, NORAD id 5709, yielded one of the poorest fits. Intelsat 4-F3 payload has a semi-major axis of $4.2349300e + 04$ km and a period of $8.6732156e + 04$ seconds. It isn't in the close vicinity of the 1:1 resonance. Thus, third body mass perturbations is the root cause of the poor fit. Figure 45 represents the position and the velocity residuals of Intelsat 4-F3 payload for the least squares fit. The propagation of Intelsat 4-F3

payload from 01-01-2013 to 03-01-2013 yielded an rms value of 923.06 km.
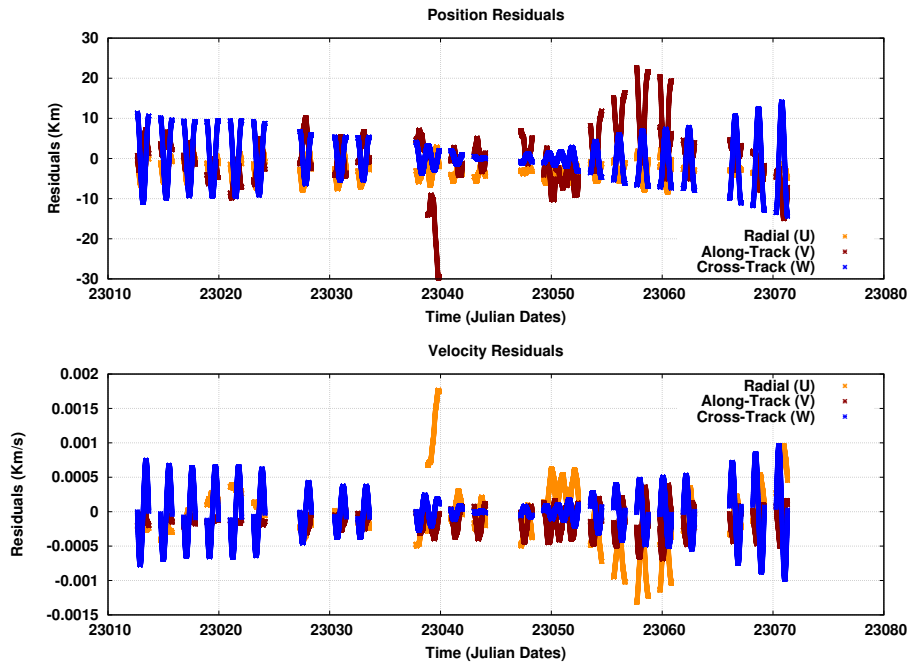
Figure 44. The Residuals for Ops 9438 payload, NORAD id 10001, over 2 Months

4.4   Further Analysis for Orbital Characteristics

The low eccentricity KAM theory is known to fail in the close vicinity of the polar and the critical inclinations and eccentricities above 10^{-3}. However, there is no experimental proof for the limits of the theory in terms of inclination and eccentricity. This section rigorously investigates those limits. For this section, 890 new test cases, which have an eccentricity of 10^{-3} and smaller, for polar inclination, 432 new test cases, which have an eccentricity of 10^{-3} and smaller, for the critical inclination, and 160 new test cases for eccentricity were retrieved from `www.space-track.com` servers, and propagated from 01-01-2014 to 03-01-2014. Another approach has been taken for the pseudo-random selection of the new test cases. For each case, the interval of interest was divided into 4 equal pieces. Equal number of random test cases were selected for each interval.
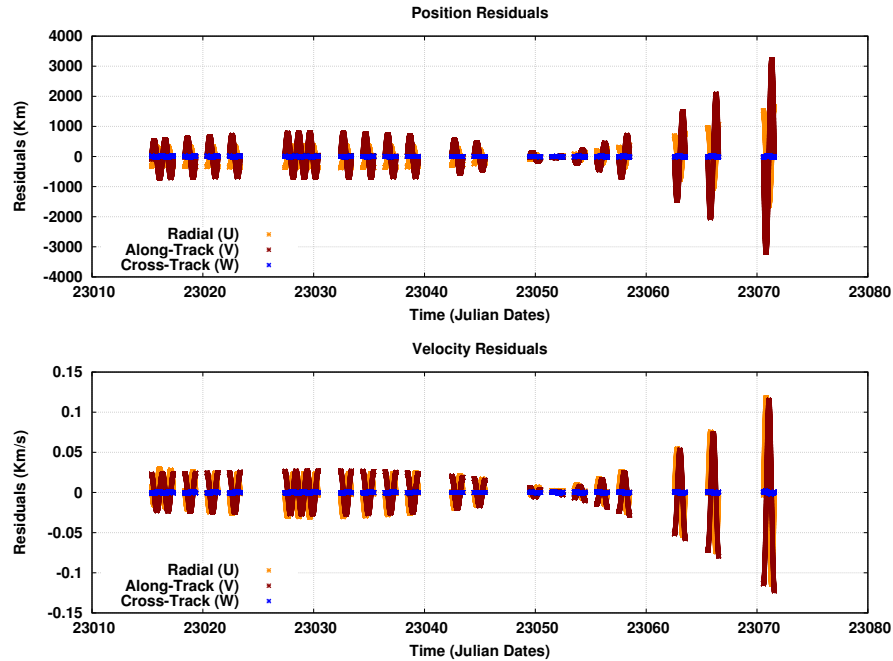
Figure 45. The Residuals for Intelsat 4-F3 payload, NORAD id 5709, over 2 Months

Figure 46 represents the success ratio versus the eccentricity. The range for the eccentricity is between 0.01 and 0.05. This plot shows the upper limit of the eccentricity that can be modeled by the theory. The drastic decrease in the success ratio can be seen in the plot. The least squares fit clearly fails for the eccentricities of 0.0233 and bigger. The decrease in the success ratio for the eccentricity from 0 to 0.01 is 25%, see Section 4.2. However, the decrease in the success ratio for the eccentricity from 0.01 to 0.014 is approximately 45%.

Figure 47 represents the success ratio versus the inclination, which is in the close vicinity of the polar inclination. From $84°$ to $96°$ all 311 test cases have failed to converge. Therefore, the close vicinity of the polar inclination certainly terminates the fitting process completely. The current theory can't model orbits which have inclinations between $84°$ and $96°$. As mentioned previously, the solution to this problem is known, but it is left to future studies. This work is specifically beneficial for collision avoidance calculations and formation flight applications.

110
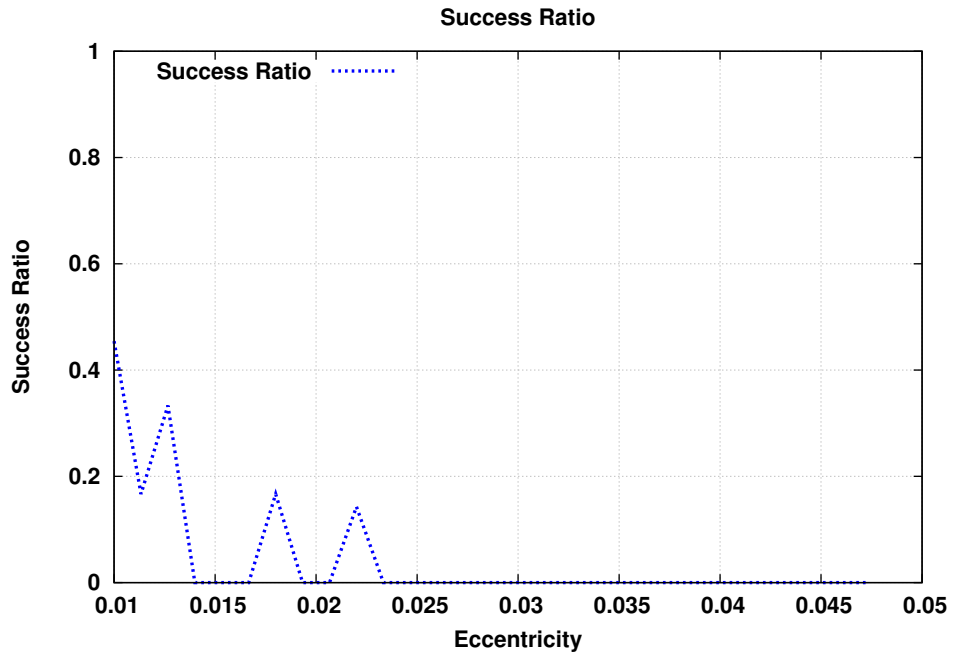
Success Ratio

Figure 46. The Upper Limit of the Eccentricity for the Theory

Success Ratio for Polar Inclination
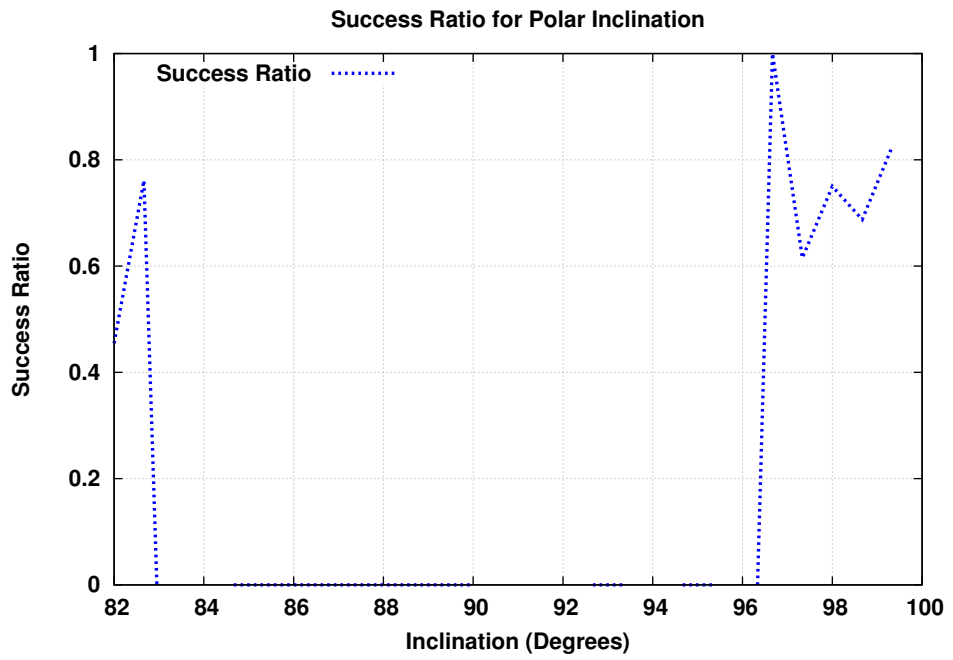
Figure 47. The Optimal Region in the Close Vicinity of Polar Inclination
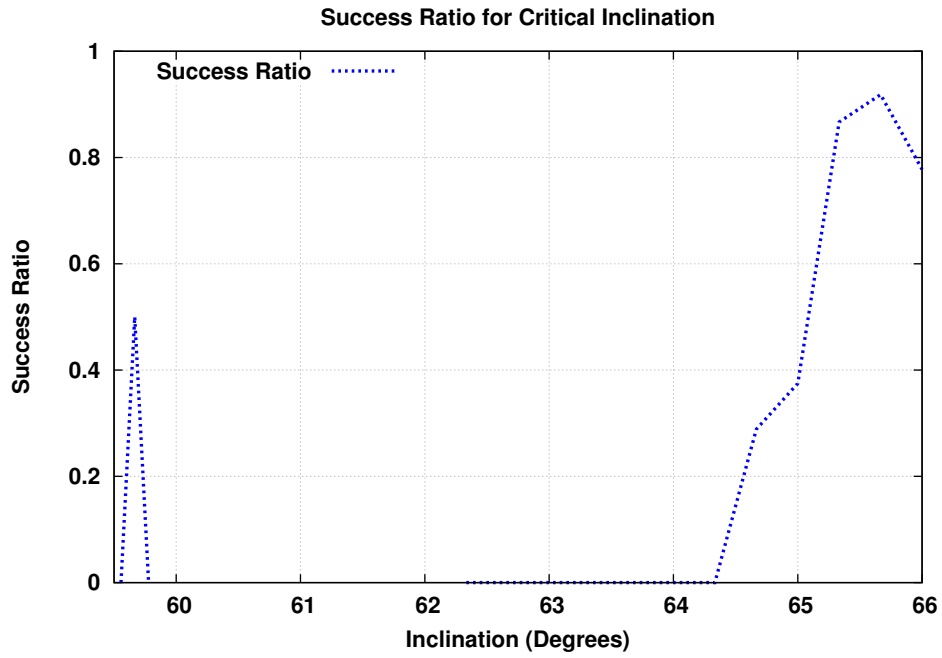
**Figure 48. The Optimal Region in the Close Vicinity of Critical Inclination**
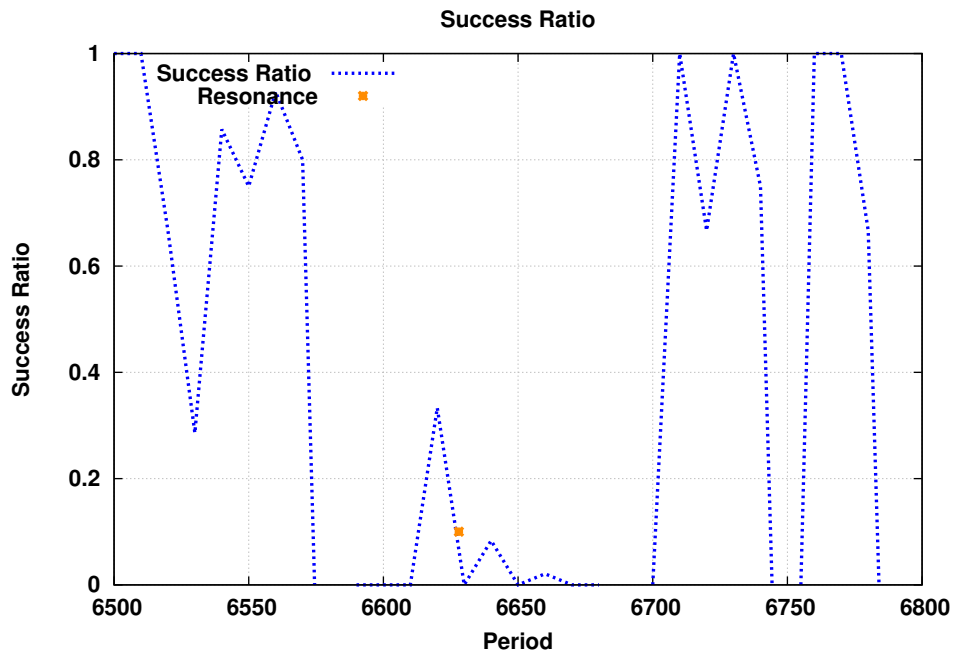
Figure 49. The Success Ratio versus Period (13:1 Resonance)

Figure 48 represents the success ratio versus the inclination, which is in the close vicinity of the critical inclination. The interval between 64.5° and 59.5° is where the success ratio becomes zero. Thus, the optimal region is the interval between 65.5° and 58°. Although it is hard to define the starting point of the optimal region due to the missing points, the upper limit is definitely 64.5°.

The author also analyzed the 13:1 resonance. 156 tests cases failed between 6570 seconds and 6700 seconds. Delta 1 debris, NORAD id 6213, Jason debris, NORAD id 35414, and Cosmos 1691, NORAD id 35414, were the only survivors in the close vicinity of the 13:1 resonance. Figure 49 represents the success ratio versus the period. This analysis provides valuable information for the behavior of the new theory near resonance.

4.5 Comparison between KAM Torus Method and SGP4

The least squares fitting process of the low eccentricity KAM torus to the SGP4 and TLE data requires continuous differential corrections of B^* value, basis frequencies, and the the global variables. The author has written additional scripts to compare the new method to SGP4. First, a low KAM torus is built, and then, least squares is fitted to SGP4 and TLE data over two months. Theory files, which are used to build the torus, and the basis frequencies are stored. Then, TLE of a future date, which is two months later than the starting date of the propagation, is propagated for an orbit by SGP4. This propagation is assumed to be the truth. Next, both the low eccentricity KAM torus and SGP4 are propagated over two months and residuals are calculated. The same process is repeated for the second time for other TLEs.

Figure 50 represents the residuals over one period for the new theory. Figure 51 represents the residuals over one period for SGP4. This comparison is made for the best least squares fitted near-Earth object, which has an rms value of 0.377006 km over two months. This test case is Thorad Delta 1 debris, NORAD id 8168. It has an inclination of
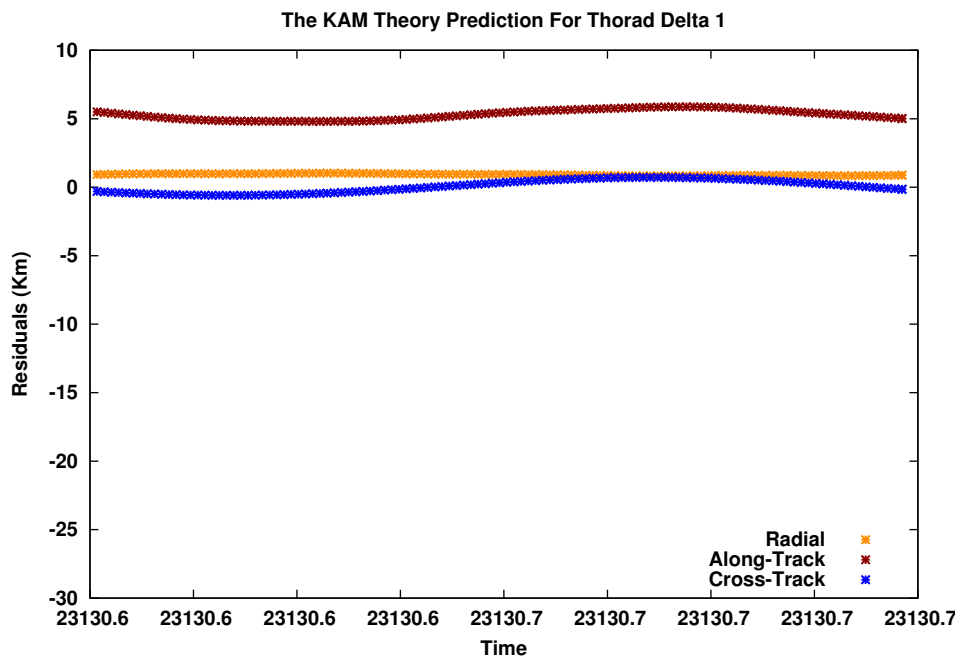
**Figure 50. The Low Eccentricity KAM Torus Prediction over 2 Months for the Best Fit Case**
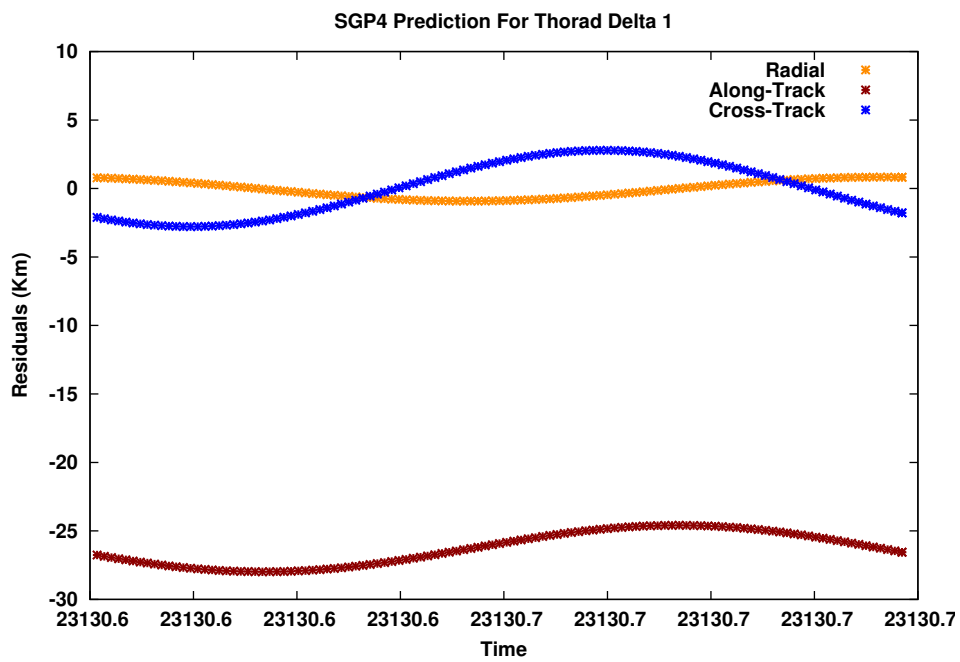
Figure 51. SGP4 prediction over 2 Months for the Best Fit Case

$1.01334e + 02°$, a semi-major axis of $7.83195e + 03$ km, and B^* value of $8.21740e − 05$. The new theory yields approximately five times more accurate predictions than SGP4 does. The theory files for this comparison was created from 01-01-2013 to 03-01-2013. The date for the truth TLE is 05-01-2013.
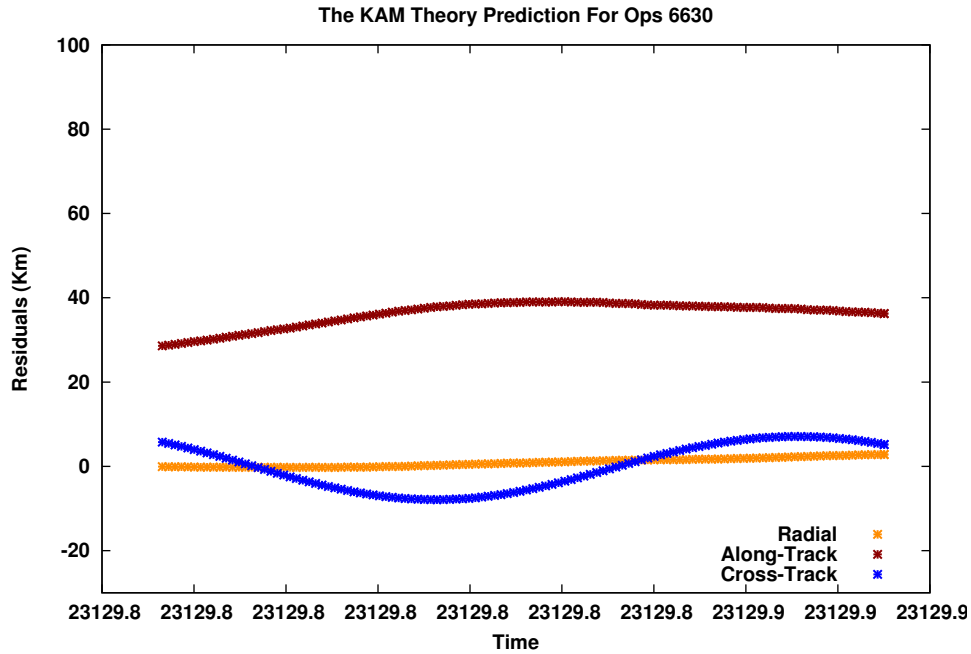

Figure 52. The Low Eccentricity KAM Torus Prediction over 2 Months for a Mean Case

Figure 52 represents the residuals over one period for the new theory. Figure 53 represents the residuals over one period for SGP4. This comparison is made for an average least squares fit, which has an rms value of 5.0332 km over two months. This test case is Ops 6630 debris, NORAD id 9323. It has an inclination of $9.7031200e + 01°$, a semi-major axis of $7.8056200e + 03$ km, and B^* value of $2.5971000e − 04$. The new theory yields approximately three times more accurate predictions than SGP4 does. The theory files for this comparison was created from 01-01-2013 to 03-01-2013. The date for the truth TLE is 05-01-2013.

The author also propagated the best fit case, NORAD id 8168, from 03-01-2013 to 05-01-2013 with approximately two days intervals. The result is very promising because there

115
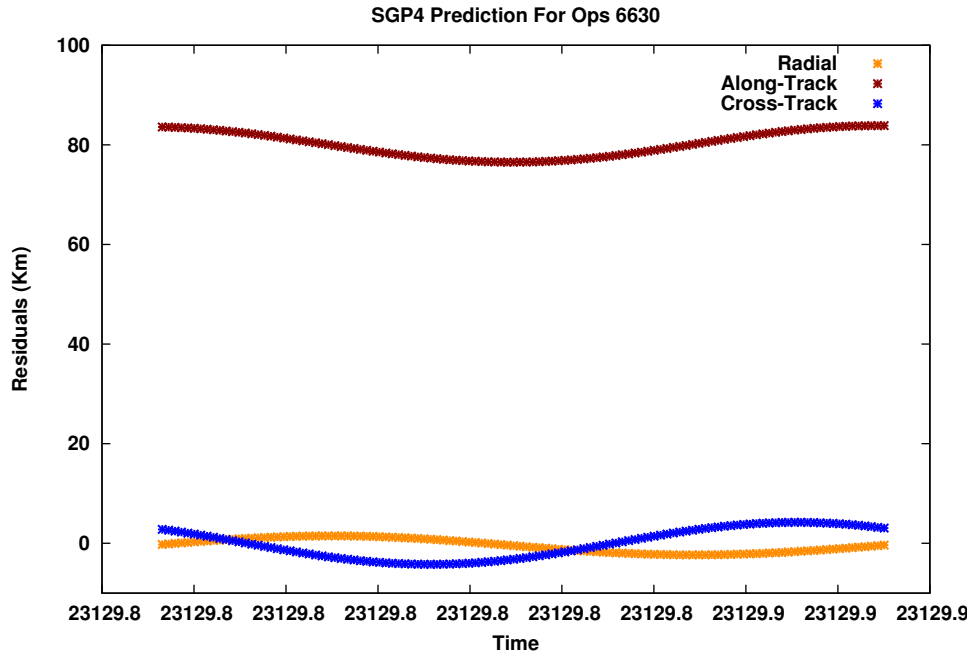
**Figure 53. SGP4 prediction over 2 Months for a Mean Case**
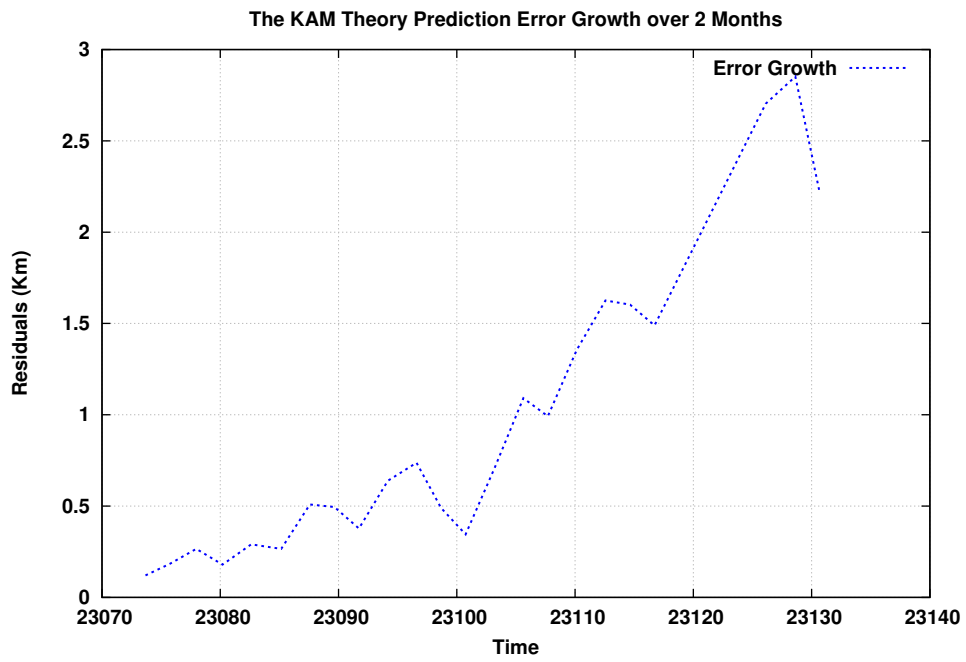
Figure 54. The Error Growth of the New Theory

is a linear error growth for one month with a small slope. Then, the error growth nearly doubles between 30 to 60 days. Figure 54 represents the residual growth versus period. The inaccuracies in SGP4 and TLE is also uncovered by Figure 54.

V. Conclusions and Recommendations

This chapter presents the conclusions and the recommendations for future studies. The first section introduces the conclusions obtained from chapter 4. The limitations and applicability of the new theory is presented. For the second section, recommendations for future studies are given.

5.1   Conclusions

Although the title for this effort is "KAM Torus Orbit Prediction using SGP4 and TLE", it has yielded more than only the possibility of orbit prediction combining the observational data and the theory. The new theory has proven to be a better substitute for SGP4. Its numerical set of algorithms provide higher accuracy and increase computational speed. The theory can be implemented in less than a minute on a home computer. The new theory has binary files associated with parameters, such as the periodic orbit, the geopotential and air drag perturbations, and second-order eccentricity perturbation. The new theory contains two parts. First, a data package which includes Fourier series. Second, a set of seven values, Q_1, Q_2, y_2, y_3, y_4, y_5, y_6, and B^* at an epoch t_o. Therefore, the new theory seems to be an alternate way to compress ephemerides.

The low eccentricity KAM method appears to be promising for collision avoidance calculations because it yields accurate predictions. The linear residual growth of the new theory for short time intervals proves its applicability to collision avoidance calculations. Although it is hard to make a precise accuracy analysis without raw observational data, the error growth plot, see Section 4.5, proves that the low eccentricity KAM torus theory may rival numerical methods in terms of accuracy. In addition, the new theory can yield far better residuals with two simple modifications. First, the relatively inaccurate TLEs can be eliminated from the fitting process, see Figure 54. Second, the linear correction behavior

for the frequencies during the fitting process can be projected forward. Moreover, the new theory can reduce the dependence on NORAD. Because most ground stations depend on NORAD TLE, they must wait NORAD to publish the TLE. However, debris and most satellites can be propagated forward in time using TLE history with high accuracy using KAM torus theory. Formation flight is another possible application for the low eccentricity KAM torus theory. Since the accuracy of the theory increases for short time periods, the new method can be an onboard collision avoidance algorithm given that the satellite can receive position data.

5.2 Future Studies

There are some issues related to the new theory. As presented throughout chapter 4, resonance, high eccentricity, polar inclination, and critical inclination issues should be addressed. This effort provides an extensive analysis of the new theory. The generalization of the theory to all orbits can be possible after these issues are solved. However, this effort can be used as future reference before applying theory on different debris and satellites. The solution to the the polar inclination problem is already known. The problem emerges due to the forms of the Legendre polynomial recursions which becomes numerically unstable. The solution to this problem is provided in Wiesel's text [64]. The atmospheric model should be improved. Russian GOST Atmosphere is a promising candidate because it requires less computation time and it is relatively accurate. It is built by empirical data obtained from Cosmos satellites. It includes solar flux and geomagnetic activity effects [60]. The application of the theory to orbits with high eccentricity and critical inclination is an area of current interest. In addition, the actual accuracy analysis requires raw observational data, because SGP4 and TLE has intrinsic inaccuracies.

Bibliography

1. V. Arnold. *Mathematical Methods of Classical Mechanics*. Springer, 1989.

2. V. I. Arnold. Small denominators and problems of stability of motion in classical and celestial mechanics. In *Collected Works*. Springer Berlin Heidelberg, 2009.

3. J. Binney and S. Kumar. Angle variables for numerically fitted orbital tori. *Monthly Notices of the Royal Astronomical Society*, 261:584–592, Apr. 1993.

4. J. Binney and D. Spergel. Spectral stellar dynamics. *Monthly Notices of the Royal Astronomical Society*, 252:308–321, Jan. 1982.

5. C. L. Bisher. Verification of kam theory on earth orbiting satellites. Master's thesis, Air Force Institute of Technology, March 2010.

6. R. E. Bordner. Orbital tori construction using trajectory following spectral methods. Master's thesis, Air Force Institute of Technology, 2010.

7. B. Bowman. A first order semi-analytic perturbation theory for highly eccentric 12 hour resonating. *NORAD document*, 1971.

8. R. Broucke. Numerical integration of periodic orbits in the main problem of artificial satellite theory. *Celestial Mechanics and Dynamical Astronomy*, 58(2):99–123, 1994.

9. D. Brouwer. Solution of the problem of artificial satellite theory without drag. *The Astronomical Journal*, 64:378–396, 1959.

10. D. Brouwer and G.-I. Hori. Theoretical evaluation of atmospheric drag effects in the motion of an artificial satellite. *Astronomical Journal*, 66:193–225, 1961.

11. G. H. B. Byron Tapley, Bob Schutz. *Statistical Orbit Determination*. Elsevier Academic Press, 2010.

12. A. Celletti and L. Chierchia. On the stability of realistic three-body problems. *Communications in Mathematical Physics*, 186(2):413–449, 1997.

13. A. Celletti and L. Chierchia. Kam stability for a three-body problem of the solar system. *Zeitschrift fr angewandte Mathematik und Physik ZAMP*, 57(1):33–41, 2005.

14. A. Celletti and L. Chierchia. Kam tori for n-body problems: a brief history. In A. Celletti and S. Ferraz-Mello, editors, *Periodic, Quasi-Periodic and Chaotic Motions in Celestial Mechanics: Theory and Applications*, pages 117–139. Springer Netherlands, 2006.

15. V. Chobotov. *Orbital Mehanics*. American Institute of Aeronautics and Astronatics, Inc, 1991.

16. B. S.-B. Claude Gignoux. *Solved Problems in Lagrangian and Hamiltonian Mechanics*. Springer, 2009.

17. S. Coffey, A. Deprit, and B. Miller. The critical inclination in artificial satellite theory. *Celestial mechanics*, 39(4):365–406, 1986.

18. J. B. Colin McGill. Torus construction in general gravitational potentials. *Monthly Notices of the Royal Astronomical Society*, 244:634–645, 1990.

19. A. F. S. Command. Basing of first u.s. space fence facility, 2012 (Accessed 27 Jan 2014).

20. C. T. Craft. Formation flight of earth satellites on kam tori. Master's thesis, Air Force Institute of Technology, September 2009.

21. P. C. David A. Vallado. Sgp4 orbit determination. In *Papers- American Institute of Aeronautics and Astronautics; 3; 1630-1658, AIAA astrodynamics specialist conference*, 2008.

22. R. Derbis. Modeling GPS Satellite Orbits Using KAM Tori. M. S. thesis, Air Force Institute of Technology, Wright-Patterson AFB, March 2008.

23. G. M. C. Dirk Brouwer. *Methods of Celestial Mechanics*. Academic Press, 1961.

24. W. Dong and Z. Chang yin. An accuracy analysis of the sgp4/sdp4 model. *Chinese Astronomy and Astrophysics*, 34(1):69–76, Jan. 2010.

25. P. R. Escobal. *Methods of Orbit Determination*. Krieger Pub. Co., 1976.

26. J. Felix R. Hoots, Paul W. Schumacher and R. A. Glover. A history of analytical orbit modeling in the united states space surveillance system. *Journal of Guidance, Control, and Dynamics*, 27:174–185, 2004.

27. S. M. A. Frank J. Regan. *Dynamics of Atmospheric Re-Entry*. American Institute of Aeronautics and Astronatics, Inc, 1993.

28. G. R. Frey. Kam torus frequency generation from two-line element sets. Master's thesis, Air Force Institute of Technology, 2011.

29. H. Goldstein. *Classical Mechanics*. Addison-Wesley Publishing Company, 1953.

30. L. J. Hagen. Effects of air drag and lunar third-body perturbations on orbital motion near a reference kam torus. Master's thesis, Air Force Institute of Technology, 2011.

31. J. Hilton, C.G. ; Kuhlman. Mathematical models for the space defense center. *Philco-Ford Publication No. U-3871*, pages 17–28, 1966.

32. R. Hujsak. A restricted four body solution for resonating satellites without drag. *NASA STI/Recon Technical Report N*, 80:24340, Nov. 1979.

33. J. K. Jeanine Arsenault, Lois Chaffee. General ephemeris routine formulationdocument. Technical report, 496L System Program Office, Electronic System Division, Hanscom Field. Bedford, Massachusetts, 1964.

34. M. Kaasalainen. Construction of invariant tori in chaotic regions. *pre*, 52:1193–1196, July 1995.

35. M. Kaasalainen and J. Binney. Construction of invariant tori and integrable hamiltonians. *Physical Review Letters*, 73:2377–2381, Oct. 1994.

36. M. Kaasalainen and J. Binney. Torus construction in potentials supporting different orbit families. *Monthly notices of the Royal Astronomical Society*, 268:1033–1040, June 1994.

37. T. Kelso. Orbit determination. *Satellite Times*, July/August, 1995. http://www.celestrak.com/columns/v01n06, 25 December 2013.

38. Y. Kozai. The motion of a close earth satellite. *Astronomical Journal*, 64:367–377, 1959.

39. D. Kunz. *Intermediate Dynamics Course Notes*. Air Force Institute of Technology, 2012.

40. M. Lane. The development of an artificial satellite theory using a power-law atmospheric density representation. *2nd Aerospace Sciences Meeting AIAA paper 65-35*, 1965.

41. M. Lane and F. Hoots. General perturbations theories derived from the 1965 lane drag theory. *Project Space Track Report No. 2*, 1979.

42. H. Lane M, Cranford. An improved analytical drag theory for the artificial satellite problem. In *AIAA paper 69-925, AIAA/AAS Astrodynamics Conference, Princeton, NJ*, 1969.

43. M. Lara. On periodic polar orbits in the artificial satellite problem. *The journal of the astronautical sciences*, 45:321–328, 1997.

44. M. Lara, A. Deprit, and A. Elipe. Numerical continuation of families of frozen orbits in the zonal problem of artificial satellite theory. *Celestial Mechanics and Dynamical Astronomy*, 62(2):167–181, 1995.

45. B. Lee. Norad tle conversion from osculating orbital element. *Journal of Astronomy and Space Sciences*, 19:395–402, Dec. 2002.

46. J.-W. Lee, Byoung-Sun; Park. Estimation of the sgp4 drag term from two osculating orbit states. *Journal of Astronomy and Space Sciences*, 20:11–20, 2003.

47. B. D. Little. Application of kam theorem to earth orbiting satellites. Master's thesis, Air Force Institute of Technology, March 2009.

48. U. Locatelli and A. Giorgilli. Invariant tori in the secular motions of the three-body planetary systems. *Celestial Mechanics and Dynamical Astronomy*, 78(1-4):47–74, 2000.

49. R. H. Lyddane. Small eccentricities or inclinations in the brouwer theory of the artificial satellite. *Astronomical Journal*, 68:555–558, 1963.

50. R. Martin. The kam theorem and the route to hamiltonian chaos. *Course Notes for Nonlinear Science*, pages 136–139, 2013.

51. L. Meirovitch. *Methods of Analytical Dynamics*. Dover Publications, 2003.

52. O. Montenbruck. An epoch state filter for use with analytical orbit models of low earth satellites. *Aerospace Science and Technology*, 4:277–287, 2000.

53. NASA. The threat of orbital debris and protecting nasa space assets from satellite collisions, 2009 (Accessed 24 Jan 2014).

54. National Aeronautics and Space Administration. *Orbital Debris Quaterly News*, 17(3), 2013.

55. U. of Texas at Austin Center for Space Research. Grace gravity model, 2012.

56. E. G. Oliver Montenbruck. *Satellite Orbits*. Springer, 2012.

57. E. Ott. *Chaos in Dynamical Systems*. Cambridge University Press, 2002.

58. I. Stellmacher. Periodic orbits around an oblate spheroid. *Celestial Mechanics*, 23:145–158, 1981.

59. U.S. Strategic Command, 2012. `http://www.stratcom.mil/factsheets/`. Dec 2012.

60. D. Vallado. *Fundementals of Astrodynamics and Applications*. Microcosm Press and Kluwer Academic Publishers, El Segundo, California, 2004.

61. D. Vallado. A Complete Rework of the SGP4 Code Found in Spacetrack Report Number 3, 2006 (Accessed 13 Sep 2013).

62. D. Vallado. *Fundementals of Astrodynamics and Applications*. Microcosm Press and Kluwer Academic Publishers, Hawthorne, California, 2013.

63. K. A. Vogel. The modal solution to the moon's orbit using canonical floquet perturbation theory. Master's thesis, Air Force Institute of Technology, December 1993.

64. W. Wiesel. *Modern Astrodynamics*. Aphelion, Beavercreek, Ohio, 2010.

65. W. E. Wiesel. Earth satellite orbits as kam tori. volume 129, pages 2669–2681. Univelt, Inc , P.O. Box 28130, San Diego, CA, 92198, USA, 2008.

66. W. E. Wiesel. Kam tori construction algorithms. In *Proceedings of the Advanced Maui Optical and Space Surveillance Technologies Conference, held in Wailea, Maui, Hawaii, September 17-19, 2008, Ed.: S. Ryan, The Maui Economic Development Board., p.E46*, 2008.

67. W. E. Wiesel. *Modern Orbit Determination*. Aphelion Press, 2010.

68. W. E. Wiesel. Earth satellite perturbation theories as approximate kam tori. *The Journal of the Astronautical Sciences*, 58(2):153–165, 2011.

69. W. E. Wiesel. A theory of low eccentricity earth satellite motion. *Advances in the Astronautical Sciences*, 143:19, 2012.

70. M. W. Yates. Stochastic orbit prediction using kam theory. Master's thesis, Air Force Institute of Technology, 2011.

Vita

1st Lieutenant Rasit Abay was born on 02 February 1984 in Tire, Turkey. He graduated from Maltepe Military High School in 2003. He graduated from Turkish Air Force Academy with a Bachelor of Science in Computer Engineering in 2007. He attended the Air Force Institute of Technology in 2012. He is a GNU/Linux and open source enthusiast. His area of interests are orbital mechanics, spacecraft attitude determination and control, numerical analysis.

REPORT DOCUMENTATION PAGE

Form Approved
OMB No. 0704–0188

1. REPORT DATE *(DD–MM–YYYY)*	2. REPORT TYPE	3. DATES COVERED *(From — To)*
27—03—2014	Master's Thesis	Oct 2012—Mar 2014

4. TITLE AND SUBTITLE

KAM Torus Orbit Prediction from Two Line Element Sets

5a. CONTRACT NUMBER

5b. GRANT NUMBER

5c. PROGRAM ELEMENT NUMBER

6. AUTHOR(S)

Abay, Rasit, 1st Lieutenant, TURAF

5d. PROJECT NUMBER

5e. TASK NUMBER

5f. WORK UNIT NUMBER

7. PERFORMING ORGANIZATION NAME(S) AND ADDRESS(ES)

Air Force Institute of Technology
Graduate School of Engineering and Management (AFIT/EN)
2950 Hobson Way
WPAFB, OH 45433-7765

8. PERFORMING ORGANIZATION REPORT NUMBER

AFIT-ENY-14-M-01

9. SPONSORING / MONITORING AGENCY NAME(S) AND ADDRESS(ES)

Intentionally Left Blank

10. SPONSOR/MONITOR'S ACRONYM(S)

11. SPONSOR/MONITOR'S REPORT NUMBER(S)

12. DISTRIBUTION / AVAILABILITY STATEMENT

DISTRIBUTION STATEMENT A:
APPROVED FOR PUBLIC RELEASE; DISTRIBUTION UNLIMITED.

13. SUPPLEMENTARY NOTES

This work is declared a work of the U.S. Government and is not subject to copyright protection in the United States.

14. ABSTRACT

A new method for orbit prediction, which is as accurate as numerical methods and as fast as analytical methods, in terms of computational time, is desirable. This paper presents Kolmogorov Arnol'd Moser (KAM) torus orbit prediction using Simplified General Perturbations 4 (SGP4) and Two-Line Element (TLE) data. First, a periodic orbit and its Floquet solution is calculated. After that, perturbations, which are on the order of 10^{-5} and smaller, are added to the periodic orbit plus Floquet solution. Then, the low eccentricity KAM torus is least squares fitted to the SGP4 and TLE data. The performance of the theory is presented in various ways. The new method is approximately five times more accurate for the best fits and three times more accurate for mean fits comparing to SGP4 and TLE. History of TLEs and KAM torus theory can be used to make accurate orbit predictions, which is conceptually similar to extrapolation. In addition, the new method may rival numerical methods and it can be used for collision avoidance calculations, and formation flight applications. However, high eccentricity, polar and critical inclination, air drag, and resonance problems should be addressed.

15. SUBJECT TERMS

KAM Theory, SGP4 and TLE, Periodic Orbit, Floquet Problem, Non-linear Least Squares

16. SECURITY CLASSIFICATION OF:

a. REPORT	b. ABSTRACT	c. THIS PAGE
U	U	U

17. LIMITATION OF ABSTRACT

UU

18. NUMBER OF PAGES

138

19a. NAME OF RESPONSIBLE PERSON
Dr William E. Wiesel Jr. (ENY)

19b. TELEPHONE NUMBER *(include area code)*
(937) 255-3636 x4312 william.wiesel@afit.edu

Standard Form 298 (Rev. 8–98)
Prescribed by ANSI Std. Z39.18